

University of Alberta

Aspects of the Colossal Magnetoresistance Material $\text{La}_{1-x}\text{Ca}_x\text{MnO}_{3-\delta}$ Across
the Metal-Insulator Transition

by

Robert J. Patterson



A thesis submitted to the Faculty of Graduate Studies and Research in partial fulfillment of
the

requirements for the degree of Master of Science

Department of Physics

Edmonton, Alberta

Fall 2005



Library and
Archives Canada

Bibliothèque et
Archives Canada

Published Heritage
Branch

Direction du
Patrimoine de l'édition

395 Wellington Street
Ottawa ON K1A 0N4
Canada

395, rue Wellington
Ottawa ON K1A 0N4
Canada

Your file *Votre référence*

ISBN: 0-494-09259-9

Our file *Notre référence*

ISBN: 0-494-09259-9

NOTICE:

The author has granted a non-exclusive license allowing Library and Archives Canada to reproduce, publish, archive, preserve, conserve, communicate to the public by telecommunication or on the Internet, loan, distribute and sell theses worldwide, for commercial or non-commercial purposes, in microform, paper, electronic and/or any other formats.

The author retains copyright ownership and moral rights in this thesis. Neither the thesis nor substantial extracts from it may be printed or otherwise reproduced without the author's permission.

AVIS:

L'auteur a accordé une licence non exclusive permettant à la Bibliothèque et Archives Canada de reproduire, publier, archiver, sauvegarder, conserver, transmettre au public par télécommunication ou par l'Internet, prêter, distribuer et vendre des thèses partout dans le monde, à des fins commerciales ou autres, sur support microforme, papier, électronique et/ou autres formats.

L'auteur conserve la propriété du droit d'auteur et des droits moraux qui protègent cette thèse. Ni la thèse ni des extraits substantiels de celle-ci ne doivent être imprimés ou autrement reproduits sans son autorisation.

In compliance with the Canadian Privacy Act some supporting forms may have been removed from this thesis.

Conformément à la loi canadienne sur la protection de la vie privée, quelques formulaires secondaires ont été enlevés de cette thèse.

While these forms may be included in the document page count, their removal does not represent any loss of content from the thesis.

Bien que ces formulaires aient inclus dans la pagination, il n'y aura aucun contenu manquant.


Canada

Dedication

To Joo Eun, for being everything to me here.

Abstract

Some properties of thin films of the colossal magnetoresistance material $\text{La}_{0.65}\text{Ca}_{0.35}\text{MnO}_{3-\delta}$ in the c-axis oriented perovskite structure are measured. The resistivity is measured in the transition region and compared against a scattering probability based on Jahn-Teller polarons. The magnetoresistive anisotropy is measured both as a function of temperature and applied magnetic field in the transition and compared against a phase separation model involving double exchange carriers and polarons. Oxygen stoichiometry of the films is investigated by vacuum annealing and is shown to shift the magnetoresistance and the negative anisotropy peak to lower temperatures. An electric field on the order of 1×10^7 V/m has been shown to have no effect on the resistivity of this material at room temperature and in the transition. Some results regarding the deposition of piezoelectric thin films of $\text{PbZr}_{1-x}\text{Ti}_x\text{O}_3$ are presented.

Acknowledgement

I would like to acknowledge the contributions of the Nanofab at the University of Alberta for the use of their facilities and the training they gave me.

Also, I would like to thank Dupont Teijin Films for their kind donation of a supply of the Mylar C polymer dielectric film.

I would like to thank Dr. Arthur Mar for participating on my committee and for the use of the PPMS system, which was run by Shane Crerar.

I would like to thank Dr. Kim Chow for the use of his Lock-In Amplifier, the use of his lab space and for being a member of my committee.

I would like to thank Dr. John Beamish for lending out his capacitance bridge and the use of his pumping station.

I would like to thank Dr. Mark Freeman for lending out his electrometer as well as for providing some background material on the LLG equation and simulation and the offer to use his software.

I would like to thank Dr. Isaac Isaac for his input on the effects of oxygen depletion on the T_c of LCMO films.

I would like to thank Dr. Massimo Boninsegni for participating as a member of my committee.

I would like to thank Dr. Cristian Batista of the Los Alamos National Laboratory for a very pleasant and helpful discussion.

I would like to thank Dr. M. Abdelhadi, D. Mullin, G. Popowich, T. Walford and W. Burris for their help and mentorship.

Finally, I would like to thank my supervisor Dr. J.A. Jung for giving a student like me the chance to pursue graduate studies. He has always been supportive, patient and concerned himself as much with my well-being as with my productivity. For this opportunity, which I have enjoyed these past few years, I owe him a great deal of gratitude.

CONTENTS

List of Figures	v
List of Tables	ix
List of Symbols, Nomenclature and Abbreviations	xi
Overview	1
I The Resistivity, Magnetization, AMR and the Effects of Oxygen Content in $\text{La}_{1-x}\text{Ca}_x\text{MnO}_{3-\delta}$	3
1 Introduction and History	4
1.1 Chemical Structure and Doping	5
1.2 Conduction and Magnetization in CMR Compounds	6
1.3 Anisotropy in the Magnetoresistance	9
1.4 Oxygen Stoichiometry	10
2 Theory and Review	11
2.1 CMR Manganites Crystallography and Electron Structure	11
2.2 Charge Transport in LCMO	15
2.2.1 Double Exchange and Magnetoresistance	15
2.2.2 Jahn-Teller Effects	18
2.3 Magnetization and Mean Field Theory	19
2.4 The Low Temperature Anisotropic Magnetoresistance and Film Oxygen Content	21
3 Experimental Procedure and Technical Details	23
3.1 Film Deposition and Patterning	23

3.2	Resistivity and Anisotropic Magnetoresistance Measurements .	27
3.2.1	General Description of the Apparatus	27
3.2.2	Temperature Instability and the Addition of a Preheater	29
3.2.3	Software Modifications	30
3.2.4	Temperature Dependence of the Resistivity	31
3.2.5	Anisotropy Measurements	31
3.3	Magnetization Measurements	33
3.4	LCMO Film Oxygen Depletion	34
4	The Resistivity in the Transition	35
4.1	Experimental Results	35
4.2	Analysis	36
4.2.1	Polaronic Scattering Probability Derivation	38
4.2.2	Resistivity Curve Fitting	56
4.3	Discussion	60
4.3.1	Low Temperature Fits in the Onset of the MIT	60
4.3.2	The High Temperature Fit to the Resistivity	64
4.3.3	Other Means of Addressing the Resistivity in CMR Compounds	66
5	The Magnetization and AMR in the Transition	68
5.1	Magnetization	68
5.1.1	Experimental Results	69
5.1.2	The Maximum in the Magnetic Anisotropy in the Tran- sition	70
5.1.3	Magnetization Analysis	71
5.1.4	Discussion of Magnetization Results	73
5.2	Anisotropic Magnetoresistance	78
5.2.1	AMR Experimental Results	78
5.2.2	Analysis of the AMR during the Transition	83
5.2.3	Discussion of the Anisotropic Magnetoresistance	95
5.3	Oxygen Depletion	103
5.3.1	Resistivity, MR and AMR Data after Vacuum Annealing	103
5.3.2	Analysis of Oxygen Content Experiments	105
5.3.3	Discussion of Film Oxygen Experiments	105
6	Conclusions	112

II	Electric Field Effect in LCMO and Preliminary Results on Depositions of PZT	116
7	Electric Field Effect	117
7.1	Motivation for Electric Field Effect Investigation	117
7.2	Experimental	118
7.2.1	Inorganic Gate Insulator	118
7.2.2	Organic Gate Insulator	119
7.2.3	Electric Field Measurements and Results	121
7.3	Discussion of Electric Field Effect	121
7.4	Summary of Electric Field Effect	123
8	Preliminary PZT Deposition Results	124
8.1	Usefulness of PZT in a CMR Context	124
8.2	PZT Technical Background	125
8.3	PZT Depositions	127
8.4	Preliminary PZT Deposition Analysis and Results	130
8.4.1	X-Ray Diffraction on PZT Thin Films	130
8.4.2	X-Ray Photoelectron Spectroscopy of PZT Thin Films	133
8.5	Discussion of Preliminary Work on PZT	133
8.6	PZT Summary	136
	Bibliography	137
A	RC Circuit Analysis and Mylar Thickness Evaluation	146
B	Spin-Orbit Coupling and Anisotropic Magnetoresistance	148
C	Further Motivation of the Empirical Partition Function	151
D	AMR and LLG Simulations	155
E	The Loss of the Magnetization at the MIT in LCMO	163
F	Some Properties of Mylar C - Dupont Datasheet	166

LIST OF FIGURES

2.1	A schematic diagram of the perovskite structure of LCMO showing the arrangement of atoms.	12
2.2	The e_g orbitals $3z^2 - r^2$ and $x^2 - y^2$	12
2.3	The t_{2g} orbitals xy , xz and yz	13
2.4	The expected electron configuration of the Mn-ions present in LCMO	15
2.5	The orientation of the Mn e_g orbitals relative to the adjacent oxygen p-orbitals	16
2.6	The two Jahn-Teller phononic modes that conserve probability for the e_g orbitals. When the e_g orbital on the Mn site is occupied, the oxygen ions move in the directions indicated. The oxygen ions relax when the electron moves off the Mn site.	19
3.1	X-Ray spectra of LAO and LCMO on LAO	24
3.2	Schematics of LCMO thin film samples CO3 and CO4	26
3.3	A schematic depicting the apparatus used in the AMR measurements	32
4.1	The standard comparison of the resistivity and magnetization of LCMO	35
4.2	The magnetoresistance of the LCMO thin film CO4	36
4.3	The resistivity of LCMO sample CO4 in the absence of an applied magnetic field	37
4.4	Convergence of the series used to estimate phononic scattering for the sinusoidal perturbation and $\beta = 1$ and $\beta = 0.1$	48
4.5	The scattering probability for the sinusoidal perturbation	49

4.6	The convergence of the gaussian scattering probability for $\alpha = 1 \times 10^{21}$ and $\alpha = 1 \times 10^{22}$	52
4.7	The scattering state energy as a function of T for the gaussian-type perturbation	53
4.8	Initial curve shape of the gaussian scattering probability as a function of temperature	54
4.9	The high temperature dependence of the gaussian scattering probability as a function of temperature	54
4.10	The thermally activated behavior above T_c of the gaussian scattering probability as a function of temperature	55
4.11	Low temperature resistivity in the onset of the transition fit by the sinusoidal scattering probability	57
4.12	Low temperature resistivity in the onset of the MIT is fit using the gaussian scattering probability	58
4.13	High temperature resistivity peak fit using the gaussian scattering probability	59
4.14	Crossover between different polaronic scattering mechanisms that best fit the resistivity as a function of temperature	61
5.1	LCMO thin film magnetization in the $B \perp c$ and the $B \parallel c$ orientations	69
5.2	A possible planar magnetic configuration at maximum magnetic anisotropy	71
5.3	Subtracted magnetization curves for $B \perp c$ and $B \parallel c$	72
5.4	LCMO magnetization $B \perp c$ near T_c with mean-field approximation fit	74
5.5	LCMO magnetization $B \perp c$ near T_c with mean-field approximation fit.	75
5.6	LCMO magnetization for $B \perp c$ at low temperatures compared with a mean field theory prediction	76
5.7	The angular dependence of the magnetoresistance of LCMO	79
5.8	Magneto-resistive anisotropy saturation from 200K to 245K and 245 to 270K	81
5.9	Magneto-resistive anisotropy saturation from 200K to 245K and 245 to 270K	82
5.10	Magneto-resistive Anisotropy peak for weak and strong fields for Sample CO3.	84
5.11	Magneto-resistive Anisotropy peak for weak and strong fields for Sample CO4	84
5.12	Schematic of the electron density for double exchange and polaronic conduction	86

5.13	The product of two Fermi functions expected to be similar to the AMR as a function of temperature	91
5.14	Magnetoresistive anisotropy saturation to high field (~ 0.7 Tesla)	96
5.15	Fits to the AMR saturation for select temperatures from 200 to 230 K	97
5.16	Fits to the AMR saturation for select temperatures from 245 to 270 K	98
5.17	Fit to the AMR for non-saturating applied magnetic field on sample CO4	99
5.18	Fit to the AMR for non-saturating applied magnetic field on sample CO4	100
5.19	Changes in the resistivity and MR as a function of vacuum annealing	104
5.20	The effects of vacuum annealing on the AMR peak in the transition	106
5.21	The peak trend for the MR and the AMR with vacuum annealing	107
5.22	The difference in peak location and the relative difference between the MR and AMR peaks with vacuum annealing	108
7.1	A schematic of the gate apparatus for the E-field effect measurement	120
8.1	XRD of MgO	130
8.2	XRD of the high temperature deposition of PZT	131
8.3	XRD spectrum of the low temperature deposition procedure for PZT	132
C.1	The magnetization computed from the empirical partition function	153
C.2	The CMR-like peak computed from the empirical partition function	153
C.3	The CMR-like effect computed from the empirical partition function	154
D.1	The direction cosines for large static H_z and a small static field anisotropy in the a-b plane	157
D.2	Visualization of a the effects of an static magnetic field in the y-direction on a spin in a large static H_z	158
D.3	The direction cosines for large static H_z and magnetic domains in the x-y plane	159

D.4	Visualization of a the effects of an oscillating magnetic field in the y-direction on a spin in a large static H_z	160
D.5	The direction cosines for large static H_y and magnetic domains in the x-y plane	161
E.1	Possible energy level diagram before and after the metal-insulator transition	164

LIST OF TABLES

2.1	Lattice Parameters of LCMO on LAO by High Resolution X-Ray Diffraction at Ambient Temperature [8]	14
3.1	Off-Axis DC Sputtering Deposition Parameters for LCMO Thin Films CO3 and CO4.	25
3.2	Dimensions of CO3 and CO4 LCMO Thin Films.	25
3.3	Vacuum Annealing History of Sample CO3	34
4.1	Parameters for the Fit from Equation 4.21 for Temperatures between 150 K and 245 K.	57
4.2	Parameters for the Fit from Equation 4.29 for Temperatures between 150 K and 245 K.	60
4.3	Parameters for the Fit from Equation 4.29 for Temperatures between 245 K and 300 K.	61
5.1	Summary of Coefficients from a Comparison of the Magnetization Data against a Mean Field Model for the B c and the B.Lc Orientations	74
8.1	Lattice Parameters of PZT on STO and (111) Pt-buffered Si by X-Ray Diffraction and an X-Ray Standing Wave technique for the tetragonal crystal structure compositions near the morphotropic boundary. [38, 69]	126
8.2	Important Off-Axis RF Sputter Deposition Parameters for PZT from Procedures at Two Different Temperatures [59, 5]	127
8.3	Off-Axis RF Sputter Deposition Parameters for PZT Test Films on (100) Silicon Made to Calibrate Deposition and Etch Rates	129

D.1	The Constants Used in the LLG Simulations	156
F.1	Select properties of Mylar C capacitor grade polymer at a thickness of $1.5\mu\text{m}$	166

List of Symbols, Nomenclature and Abbreviations

- CMR** – Colossal Magnetoresistance, refers to the marked decrease in the resistivity of CMR materials under the influence of an external applied magnetic field at temperatures corresponding to the metal-insulator transition.
- DE** – Double Exchange, the conduction mechanism in the ferromagnetic phase of CMR materials.
- MR** – Magnetoresistance, the quantity obtained by subtracting two resistivity curves, one without an applied magnetic field and one with an applied magnetic field. This quantity shows up as a peak and is normalized to the resistivity curve in zero field. See the Theory section, equation 2.4.
- MA** – Magnetic Anisotropy, such as that seen during the MIT for the comparison of normalized magnetization curves.
- AMR or MRA** – Anisotropic Magnetoresistance or Magneto-Resistive Anisotropy, respectively. The difference in the measured resistance depending on the angle of an applied B-field and with respect to the crystal c-axis. For consistency, AMR will typically be used to refer to this quantity.
- Perovskite** – A ‘near cubic’ atomic arrangement. In the case of the manganites, the orthorhombic lattice can be considered to be centered on the Mn ion. The Mn ion has six bonds in total to oxygen ions in both the positive and negative directions of the three coordinate axes. The

La ion sits at the four corners of the orthorhombic box. (See Fig. 2.1)
The perovskite films investigated here are c-axis (long axis) oriented.

c-axis – The long axis of the perovskite structure. The c-axis direction will be perpendicular to the plane of the film and will be taken as synonymous with the z-direction throughout the entirety of this report ($\hat{c} \equiv \hat{z}$).

a-b plane – This is the plane in which the perovskite structure has relatively similar dimensions. Through the entirety of this report the film plane will correspond to the a-b plane. In addition, the directions x and y will correspond to the directions a and b respectively ($\hat{a} \equiv \hat{x}$ and $\hat{b} \equiv \hat{y}$).

Manganite – A manganese oxide that has a high oxidation state, in this work this term will usually refer to LCMO, which has an oxidation state of +3 or +4.

$e_{g,0}$ – This is a short form for the $3z^2 - r^2$ orbital, since it has the angular momentum quantum number $l = 0$.

$e_{g,2}$ – This is a short form for the $x^2 - y^2$ orbital, since it has angular momentum quantum number $l = 2$

E_a, E_b – In the derivation of the scattering probabilities based on phonons, these energies correspond to the plane wave (double-exchange) and polaron (JT distorted) energies, respectively. Please see section 4.2.1.

LCMO – $\text{La}_{1-x}\text{Ca}_x\text{MnO}_3$ with $x = 0.35$ in all the experimentation done for this report.

LSMO – $\text{La}_{1-x}\text{Sr}_x\text{MnO}_3$, a CMR material related to LCMO, just with a different dopant species, which results in slightly different properties.

LMO – LaMnO_3 , the Mott-insulating parent compound of LCMO.

CMO – CaMnO_3 .

STO – SrTiO_3 a substrate material with good lattice matching to LCMO and a good insulator.

LAO – LaAlO_3 a substrate material with good lattice matching to LCMO and a good insulator.

PZT – $\text{PbZr}_{1-x}\text{Ti}_x\text{O}_3$ a piezoelectric material used in thin film form in the experimentation. The optimal doping level for electromechanical properties is $x = 0.53$.

MIT – Metal-Insulator Transition, for manganites occurring between about 200K and 300 K. In LCMO, this is also accompanied by gain or loss of ferromagnetic order.

Transition Region – The temperature region over which the precipitous rise in the resistivity of CMR materials occurs. For LCMO, this region corresponds to roughly 200 - 270 Kelvin.

FET – Field Effect Transistor

MOSFET – The Metal-Oxide-Semiconductor Field Effect Transistor is currently the device geometry used in a great deal of the contemporary solid state microelectronics. It is a solid state switch having a source a gate and a drain. When the gate voltage is high, current is allowed to flow from source to drain and the transistor is "ON". Without an applied gate voltage, no current flows and the transistor is OFF.

RF – Radio Frequency, 13.6 MHz is the standard frequency assigned for magnetron sputtering.

VB – Visual Basic, for this report the version of the programming language is 6.0 and it was used as a part of the Visual Studio .NET suite.

Electrostriction and Piezoelectricity – Electrostriction refers to the mechanical deformation a material may undergo as a result of an applied electric field. Piezoelectricity is the opposite effect, referring to the electric dipole generated under the influence of a mechanical stress.

ZF – Zero Field, no external applied magnetic field is applied to the LCMO thin film during the measurement.

B – An externally applied magnetic field.

$B \perp c$ – The applied magnetic field is perpendicular to the c-axis of the LCMO film and parallel to the applied current.

$B \parallel c$ – The applied magnetic field is parallel to the c-axis of the film and perpendicular to the applied current.

XPS – X-Ray Photoelectron Spectroscopy refers to the ejection of low lying ‘core’ electrons from the atoms in a solid by means of bombarding X-Rays. These photoelectrons have characteristic energies which can be used to determine, for example, film stoichiometry with relatively good accuracy.

XRD – X-Ray Diffraction from Bragg’s Law is used to probe the crystal structure of a solid.

JT or JTD – Jahn-Teller or Jahn-Teller Distortion. These distortions can be static or dynamical. There are two modes worth considering that conserve probability for the e_g orbitals. These modes are shown schematically in Figure 2.6.

Polaron – A polaron, or dressed electron, is an electron that travels through the lattice accompanied by phonons. The conduction of this electron is intimately tied to the phonons that move with it.

LN₂ – Liquid Nitrogen.

TEM – Transmission Electron Microscopy

MFM – Magnetic Force Microscopy, a variation on Atomic Force Microscopy (AFM).

LLG – Landau Lifshitz Gilbert, with reference to the equation attributed to them with respect to the magnetization direction of a classical dipole or dipoles.

T – In this report, T will always refer to the temperature.

High Temperature – in this report, will always refer to temperatures at or above T_c .

Low Temperature – in this report, will always refer to temperatures at or below T_c .

Overview

This report is broken into two parts. The first part discusses work that is largely complete. The second part presents work that was unsuccessful in producing a measurable effect or that was preliminary in nature. The structure of these two parts is as follows.

The first part contains some completed work relevant to CMR manganites. As much as possible, this part is organized in the format of a traditional laboratory report. An introduction and some background on CMR manganites, emphasizing the material $\text{La}_{1-x}\text{Ca}_x\text{MnO}_{3-\delta}$, is given in the first two chapters. An explanation of the experimental procedure and changes made to the apparatus are specified in the next chapter. A chapter is dedicated to some resistivity measurements made across the metal-insulator transition. Also, data relevant to the magnetic and magnetoresistive anisotropy is presented in a chapter, along with the effects of a reduction in oxygen doping. Measurements of the magnetoresistance and the AMR are made for decreasing film oxygen content. This part is concluded by offering a few possible interpretations of the colossal magnetoresistance effect that arises in the transition, and some potential future work is outlined.

The second part is organized into two largely self contained chapters. The first chapter outlines the effects of an applied electric field to these materials. This experiment had a null result for very large applied electric fields both at room temperature and at temperatures corresponding to the metal-insulator transition. Some preliminary work on depositions of the piezoelectric material PZT by sputtering is also presented.

Part I

The Resistivity, Magnetization, AMR and the Effects of Oxygen Content in $\text{La}_{1-x}\text{Ca}_x\text{MnO}_{3-\delta}$

Introduction and History

Transition metal oxides have been shown to display a wide variety of interesting properties. This has been attributed to a strong correlation between spin, orbit and translational degrees of freedom. As a result these materials have been studied quite intensively in the pursuit of a greater understanding of the physics of correlated electron systems.

One interesting family of the transition metal oxides are the so-called Colossal Magnetoresistance (CMR) materials. CMR materials undergo a transition from a ferromagnetic metal to a paramagnetic insulator as a function of temperature. This Metal-Insulator Transition (MIT) occurs near the critical or Curie Temperature (T_c) of the material. Near this temperature, during the phase transition, the resistance of the material can rise by orders of magnitude. Across the MIT, the resistivity of the material shows an extraordinarily large change under the influence of an applied magnetic field, giving rise to the name Colossal Magnetoresistance. Also the MIT is relatively broad. The CMR phase transition, corresponding to a rise in resistivity and the loss of ferromagnetism spans approximately 70 Kelvin.

Thin films of these materials have also been studied. These systems are

of interest due to their potential applications in microelectronics. The potential applications range from magnetic read-heads to Field Effect Transistors (FETs) [33].

This report presents the results of a study of some of the aspects of CMR materials. In the following sections, some more detailed background on the chemical species, resistivity, magnetization, magnetoresistive anisotropy and oxygen content is given.

1.1 Chemical Structure and Doping

CMR compounds can have some variation with respect to the particular elements present. The general stoichiometry is given by $\text{Re}_{1-x}\text{A}_x\text{MnO}_3$, where Re is a rare earth element such as lanthanum (La) and A is a divalent alkaline earth atom such as calcium (Ca) [35].

A variety of atomic species can be composed in this way to form materials displaying the CMR effect. In the place of La, praseodymium and neodymium can be substituted [35]. For praseodymium some very unusual effects at low temperature can be observed [62]. In the case of neodymium, a significant lowering of the critical temperature, T_c , is observed [48]. As a dopant atom, strontium and barium have also been used [35]. Strontium based compounds display very high critical temperatures at or above room temperature depending on the doping level [40]. Doping by these three elements (Ba, Ca, Sr) results in a hole doped “p-type” transition metal oxide, since these elements have one less valence electron than La. Also, tin (Sn) can be used as a dopant atom. This results in an electron doped n-type transition metal compound, as Sn acts as an electron donor in the lattice [14], though the Mn and O stoichiometry has to change somewhat.

Depending on the dopant and doping level, numerous different structural

and magnetic phases can be found in CMR compounds [35]. At a doping level of $x = 0$, the material is a Mott insulator. A Mott insulator is a material in which the strong Coulomb interaction between electrons causes a splitting in the conduction band, leading to a full band at half filling. The Mott insulating parent compound has antiferromagnetic magnetic ordering. With hole doping, empty sites are introduced into the structure and the material becomes conductive. In this work, the sole material studied is $\text{La}_{1-x}\text{Ca}_x\text{MnO}_3$, with a hole dopant level of $x = 0.35$. This is the optimum doping level giving the highest T_c for this compound, a temperature very near 270 K. That is, the ferromagnetic, highly conductive phase of the material survives to the highest temperature before the transition to paramagnetism and insulative behavior occurs.

1.2 Conduction and Magnetization in CMR Compounds

The conduction of charge in these CMR compounds is attributed to the well-known double exchange mechanism, first proposed by Zener in 1951 [70]. It was proposed based on ideas from the simple system NaCl, and was originally employed to explain some of the observations of Jonker and Van Santen. The theory of Double Exchange (DE) was essentially employed to overcome the obstacle of conduction across an oxygen ion with a full valence shell in something like a tight binding model.

The crystal structure for LCMO is shown schematically in Figure 2.1. It shows that in order to go from one Mn atom to another Mn atom, an oxygen atom must be crossed. Since the Fermi energy lies in the d-orbitals on the Mn sites, this is where the mobile holes introduced into the material by Ca doping are expected to reside. These holes cause the Mn atoms to be in either

an Mn^{+3} or Mn^{+4} state. Now, in order to move charge from one Mn ion to another, the charge must cross the full valence of the intermediate oxygen atom. The DE mechanism allows for an electron to move from an Mn^{+3} ion to an adjacent O^{-2} ion along with the simultaneous transfer of an electron from the O^{-2} ion to the opposite Mn^{+4} ion, hence the term “double-exchange”.

This idea was subsequently expanded upon by Anderson and Hasegawa in 1955 [3] and De Gennes in 1960 [20]. Additional work on the energy level splittings resulting from the numerous perturbations found in transition metal compound lattices was treated in detail by the work of Goodenough in 1967 [22]. Kubo and Ohata in 1972 formulated the first fully quantum mechanical treatment, penning the double exchange Hamiltonian in second quantized notation [55]. The theory was considered rather successful in that it did seem to explain the coupling of the ferromagnetic order to the transport of charge at low temperatures.

With the realization of the immense usefulness of solid state electronics there was a resurgence of interest in CMR materials, since they might have potential applications in microelectronic devices. With this resurgence came the realization that the picture surrounding the CMR manganites was far from complete. For example, the double exchange theory alone did not explain the large increase in the resistivity close to the Curie temperature [44]. Thermal fluctuations causing spin misalignment at high temperatures can account for at most a few percent of change in resistivity, not the orders of magnitude changes observed in CMR materials. Polaronic behavior of conduction electrons trapped by Jahn-Teller modes were suspected to play a role in this immense increase in the resistivity of these materials.

Jahn and Teller showed in 1931 that if a system of atoms, of dimension greater than one, has an arrangement that is highly symmetric and has de-

generate electronic states near the Fermi level, then this system can lower its energy by lowering the symmetry of the atomic arrangement [25]. Van Vleck showed that for manganites there were two appropriate Jahn-Teller modes to consider, shown schematically in Figure 2.6 [65]. Subsequently, Kanamori minimized the energy of these modes, and found that the minimization was not unique but was parameterized by a magnitude and a phase that mixed the JT modes in mixed-valence manganites like LCMO [27]. This parameterization still stands as one means of addressing the energy splitting arising from coupling between JT distortions and conduction electrons [45].

Compelling evidence for this polaronic mechanism has been provided experimentally by neutron diffraction experiments [1], as well as by X-ray Photoelectron Spectroscopy (XPS) [37]. In terms of a theoretical formulation, analytical descriptions of the resistivity expected from the introduction of Jahn-Teller polarons into CMR materials is mostly lacking, though at least one attempt has been made with some success [68]. Another manner in which the resistivity due to polarons is addressed is based on specific heat arguments, and includes a few powers of the temperature [58]. This fit performs well at low temperatures in stoichiometric cases. Since a standardized method for moving between quantum mechanical computations on Hamiltonians and macroscopic transport properties such as resistivities has still not been established [44], it is no surprise that this problem is still without a rigorous solution despite the immense amount of effort that has been focussed in this direction.

While the low temperature transport has a largely satisfactory explanation, and a great deal of work has gone into attempts to obtain a working model of the resistivity in the transition region, the high temperature electrical properties of CMR materials are also still in question. Above the

Curie temperature, the resistivity appears thermally activated, as it does in a semiconducting material. This has led some to investigate the possibility of Fermi level shifts in these materials, suspecting that such a shift may move the Fermi level into the gap that occurs due to the coulomb repulsion in the Mott insulating state [18]. However, it is quite likely, based on a simplified analysis presented in this work, as well as the work of other groups [68], that this semiconductor-like behavior is actually a consequence of the onset of polaronic conduction.

The magnetization of these materials has been well known for a long period of time. Measurements of the magnetization can be fit by the model of Searle and Wang, developed in 1969 [55].

1.3 Anisotropy in the Magnetoresistance

Measurements of the Anisotropic Magnetoresistance (AMR) have been made more recently. Detailed measurements of this phenomenon seem to be in short supply, perhaps due to the seemingly limited applicability of these measurements to technological applications. Also, very little in the way of theoretical explanation for this phenomenon exists, particularly in the transition region. A comparison of the AMR at low temperatures to an anisotropy calculation based on spin-orbit coupling has been done and it achieved a relatively good correspondence [76]. Sinusoidal fits to the AMR peaks as a function of angle have been attempted [2]. In terms of proposing and discussing the mechanism behind the anomalously large AMR during the MIT, there have been a few attempts to qualitatively address the subject [6]. This is currently very much an open problem.

Generally, little attention has been paid to the saturation of the AMR as a function of magnetic field. A mechanism or a suitable theoretical explanation

is absent, leading to little to compare this data against.

1.4 Oxygen Stoichiometry

The effects of oxygen stoichiometry in these materials has also been investigated recently [47, 57]. This has been reflected by the reformulation of the standard CMR stoichiometric formulae to $\text{Re}_{1-x}\text{A}_x\text{MnO}_{3-\delta}$. The effect of oxygen content on the CMR compounds is marked. While the effects of oxygen stoichiometry on the resistivity of thin films of CMR materials on different substrates has recently been investigated [58], the effect of oxygen content on the MR and negative AMR in the transition region has not yet been presented.

Theory and Review

2.1 CMR Manganites Crystallography and Electron Structure

The crystal structure of LCMO is perovskite [42]. It has a slightly orthorhombic unit cell, with either La or Ca ions at the corners of the box, oxygen ions centered on each face and a body-centered Mn ion, as shown in Figure 2.1. The unit cell is parameterized by three vectors \vec{a} , \vec{b} and \vec{c} each having different magnitudes and at angles of 90° to one another, forming a “telephone-booth” type structure. This orthorhombic perovskite structure is actually distorted by lattice strain in LCMO. It is not a perfect orthorhombic structure. This can be seen in neutron diffraction studies [11].

The parameters of LCMO’s perovskite lattice have been measured [8]. These lattice parameters are shown in Table 2.1.

The important orbitals in LCMO are the five d-orbitals. In the material these d-orbitals are split into two groups known as the “ e_g ” and “ t_{2g} ” states. These states correspond to specific 3d hydrogenic wave functions [61]. The formulae for these states are standard, and can be found in Ref. [9]. The angular parts of these states are shown in Figures 2.2 and 2.3.

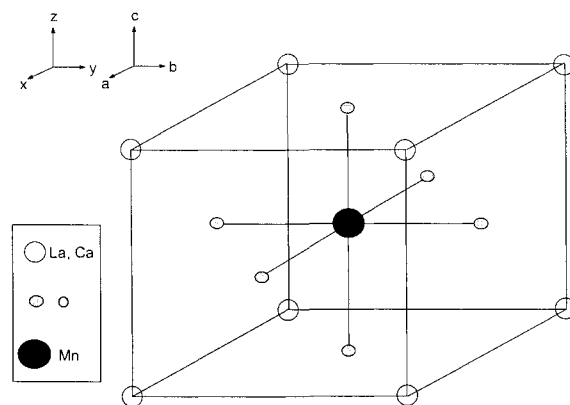


Figure 2.1: A schematic diagram of the perovskite structure of LCMO showing the arrangement of atoms.

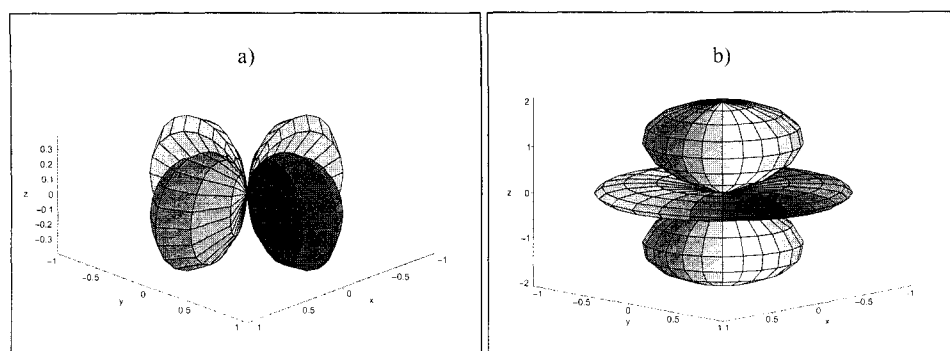


Figure 2.2: The angular components of the e_g orbitals a) $x^2 - y^2$ and b) $3z^2 - r^2$ with radii normalized to 1.

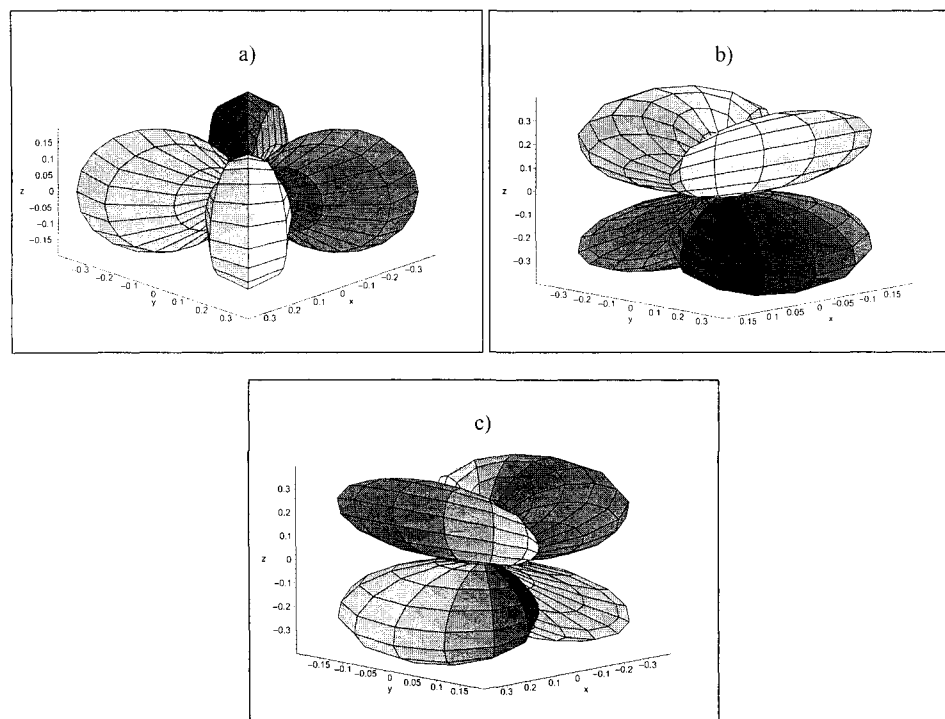


Figure 2.3: The angular components of the t_{2g} orbitals a) xy , b) yz and c) xz with radii normalized to 1.

The band structure of these materials has been analyzed for the pure material LaMnO_3 and CaMnO_3 by density functional methods in a comprehensive way [56]. The calculations use the Local Density Approximation (LDA) of Density Functional Theory. It shows many of the features that are expected in these materials. The Fermi level for LMO is at the top of the e_g band and there is a small gap between the Fermi Level and the next accessible energy states. A prediction of the size of the coulomb repulsion energy U (8-10 eV) and the spin exchange energy J (0.9 eV) are also presented.

There are many degeneracy lifting energy splittings involved in transition metal oxides. The energy splittings arise from numerous interactions. These splittings for the CMR manganites, and generally for transition metal compounds containing Mn, are intra-atomic electron correlation, spin-orbit coupling, crystal field splitting (cubic and non-cubic), the electron exchange energy and the elastic energies of cationic interstices that are displaced from their equilibrium positions in order to lower their energy [22].

Of these splittings, the most important are the intra-atomic electron correlations that lead to Hund's rules, the crystal field effect and elastic lattice effects. These give rise to the splittings and electron configuration shown in Figure 2.4.

Table 2.1: Lattice Parameters of LCMO on LAO by High Resolution X-Ray Diffraction at Ambient Temperature [8]

Lattice Parameter	Length [Å]
a	3.842
b	3.854
c	3.921

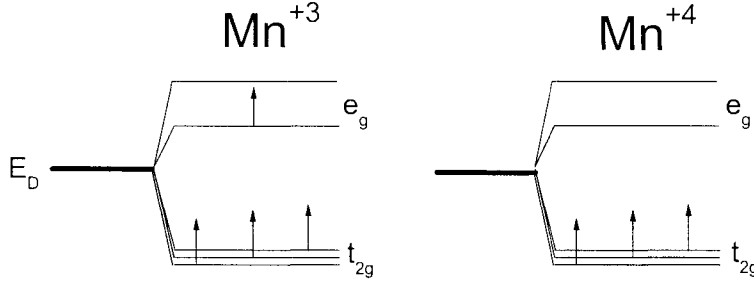


Figure 2.4: The electron configuration and schematic energy level diagram is shown. The Mn^{+3} ions have a singly occupied e_g orbital while the Mn^{+4} ion does not. The e_g and t_{2g} energy levels arise as a result of crystal field splitting. The splitting in the e_g band is expected from Jahn-Teller considerations. The JT splitting in the t_{2g} band is omitted here for simplicity. Single occupancy is favored as a result of the strong coulomb repulsion between electrons, leading to Hund's rules. E_D stands for the energy of the 5-fold degenerate states.

2.2 Charge Transport in LCMO

There are two paradigms in which to understand the transport properties of LCMO. The double-exchange mechanism is best applied at temperatures well below the transition, while Jahn-Teller polaronic transport is expected to be the dominant mechanism during and above the phase transition.

2.2.1 Double Exchange and Magnetoresistance

The double exchange integral is of the form [3]

$$J^* = \int \psi_{d,1} \psi_{p,1} H \psi_{p,2} \psi_{d,2} d^3r \quad (2.1)$$

where $\psi_{d,i}$, $\psi_{p,i}$ are the Mn or O orbital wave functions on the Mn^{+3} side of the oxygen ion or on the Mn^{+4} side of the oxygen, H is the Hamiltonian of the system, containing the typical kinetic energy terms and a function of the averaged potentials and the usual bounds are used to evaluate the integral

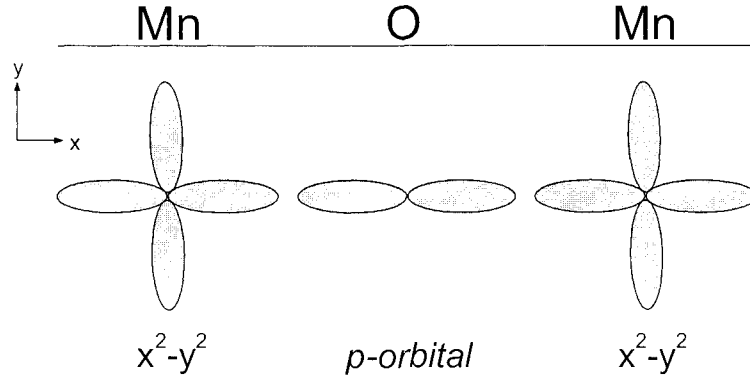


Figure 2.5: The orientation of the Mn e_g orbitals relative to the adjacent oxygen p-orbitals is shown. The e_g orbitals have an appreciable spatial extent along the coordinate axes. The oxygen p-orbitals also extend along the coordinate axes. The x^2-y^2 d-orbital is shown in this example, but this is true for both the e_g orbitals.

over r , ϕ and θ .

This integral is vanishingly small unless the p and d orbitals considered are not orthogonal, showing immediately that the e_g orbital selected for conduction must have an appreciable probability density along one of the coordinate axes, as the p-orbitals do. This is shown schematically in Figure 2.5. That is why only two of the five d-orbitals are suitable for conduction by double-exchange.

This integral in Equation 2.1 should be interpreted as one in which the electron in the Mn^{+3} d-orbital moves to the adjacent oxygen p-orbital *simultaneously* with the movement of an electron from the oxygen p-orbital to the adjacent Mn^{+4} d-orbital. This motion is also implied in the standard double exchange Hamiltonian [55].

$$H = \sum_{\langle i,j \rangle} t_{ij}(c_i^\dagger c_j + h.c.) - J_H \sum_i S_i \cdot \sigma_i^c n_i \quad (2.2)$$

where t_{ij} is the hopping probability of the nearly free electrons, J_H is the Hund's coupling energy which is the energy gained when the e_g electron's spin, S_i^z is aligned to the "core" t_{2g} electron spins, σ_i^c . The typical second-quantized creation and annihilation operators are used, c and c^\dagger , n_i is the number operator, $c^\dagger c$, that counts occupied e_g orbitals, and the indices i, j run over all sites or nearest neighbors, as required.

Typically, this Hamiltonian and any other terms added to it, such as the effects of an applied magnetic field, are considered in the $J_H \rightarrow \infty$ limit. Working in this limit means that the core t_{2g} orbital spins and the conduction e_g electron spins must be aligned. When this is the case, the following well known result is recovered [11].

$$t_{ij} = |t| \cos \phi_{ij} \quad (2.3)$$

where t_{ij} is the hopping energy and ϕ_{ij} is the alignment of spins on adjacent Mn^{+3} and Mn^{+4} ions. This is a key result as it shows that the transport of charge is dependent on the angle between spins on nearest-neighbor Mn ion sites. When spins are not aligned, the hopping parameter is decreased.

Another quantity of interest is the Magnetoresistance (MR) of the CMR thin film. The MR quantifies the difference in the resistivity as a function of applied magnetic field. The definition of the MR is

$$MR = \frac{\rho_B - \rho_0}{\rho_0} \quad (2.4)$$

where $\rho_{B,0}$ refers to the resistivity of the CMR material in the presence of a magnetic field or in zero field respectively.

The Double-Exchange Hamiltonian involves strong Hund's coupling between the spin of the occupied e_g orbital and the t_{2g} orbitals [44]. A strong

coulomb on site repulsion between electrons is also present [56]. These two statements can be seen on some level to be equivalent, each saying that it is energetically preferable to have electrons in different orbitals and ferromagnetically aligned than to have electrons in the same orbital and antiferromagnetically aligned. The double-exchange interaction can then be invoked to show why it is that at low temperatures the material is a ferromagnetic conductor and at high temperatures the resistivity increases. However, this cannot be the end of the story given that the additional scattering at high temperatures does not localize a great deal of charge in the band [42]. Again, polaronic conduction has been credited with the sharp increase of the resistivity near the curie temperature T_c .

There seems to be some ambiguity in terms of defining the critical temperature, T_c , in the literature. For the purposes of this report, when it is not otherwise specified, T_c will be taken as the inflection point in the resistivity curve. That is, if the resistivity curve is differentiated with respect to temperature, the temperature at which the resulting curve ($\frac{d\rho}{dT}$) maximizes is taken to be T_c . This is one acceptable way to define the parameter [50].

2.2.2 Jahn-Teller Effects

There are two Jahn-Teller modes that are important to the conduction orbitals [56]. These modes are shown schematically in Figure 2.6. It can be imagined that the oxygen ions surrounding the Mn ion oscillate on their respective axes in the directions shown in Figure 2.6.

Contemporary attempts to obtain the resistivity of CMR materials usually involve very detailed numerical computations or very sophisticated quantum mechanical formulations [45, 44]. While these are certainly very powerful tools involving a great deal of mathematical rigor, they have left a gap in

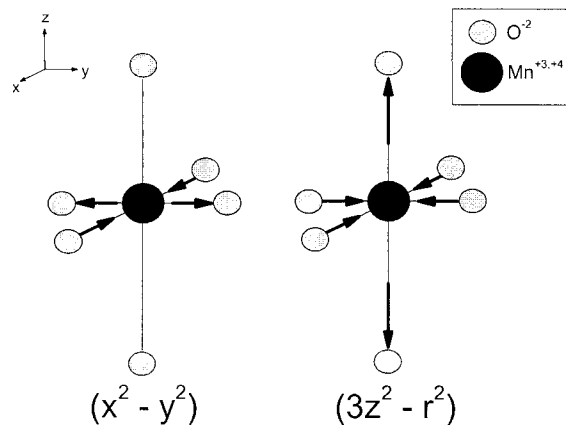


Figure 2.6: The two Jahn-Teller phononic modes that conserve probability for the e_g orbitals. When the e_g orbital on the Mn site is occupied, the oxygen ions move in the directions indicated. The oxygen ions relax when the electron moves off the Mn site.

terms of having a simple model with which to compare experimental data. A model based on some more simplified assumptions will be derived in section 4.2.1. This work is done expressly for the purposes of this report and is not taken from or based on any other work.

2.3 Magnetization and Mean Field Theory

The mean field theory of magnetic phase transitions has existed for a long time [51]. Many attempts to understand the CMR effect in manganites are based on dynamical mean field theories [45]. This motivates the belief that there is some merit in a comparison of the magnetization in the transition to a mean field approach.

The development for the dependence of the magnetization on temperature is given in [51]. In the “zeroth order approximation” to the Ising model, a transcendental equation is arrived at involving the long-range spin order

parameter (\bar{L}_o), the temperature (T) and the exchange integral (J).

$$\bar{L}_0 = \tanh \frac{qJ\bar{L}_0}{kT} \quad (2.5)$$

where q is the number of neighbors contributing to the mean field and the magnetic field in the derivation has been set to zero to investigate spontaneous magnetic order.

This equation has a solution if

$$\frac{qJ}{kT} < 1 \quad \text{OR} \quad T < \frac{qJ}{k} = T_c \quad (2.6)$$

where T_c is the critical or Curie temperature of the transition.

In the limit where $T \rightarrow T_c$, given this solution, the order parameter can be simplified.

$$\bar{L}_0 \cong \left(3 \left[1 - \frac{T}{T_c} \right] \right)^{\frac{1}{2}} \quad (2.7)$$

Here, the exponent $\frac{1}{2}$ is a critical parameter. This is typically the parameter that is compared against experiment to test the validity of a mean-field approximation. Higher approximations of the Ising model predict different critical exponents from that given in Equation 2.7. Typically, these approximations give lower values of the so-called critical exponent. The exponent starts off much less than one and increases with the dimensionality of the system. The addition of more neighboring atoms in higher dimensions brings the environment experienced by any given electron closer to that of a mean-field. Simply, more neighboring atoms increases field averaging [51].

In addition, there is another simplification as $T \rightarrow 0$.

$$\bar{L}_0 \cong 1 - 2e^{-2\frac{T_c}{T}} \quad (2.8)$$

2.4 The Low Temperature Anisotropic Magnetoresistance and Film Oxygen Content

The definition of the AMR, in the absence of access to a more suitable normalization is

$$AMR = \frac{\rho_{\parallel} - \rho_{\perp}}{\rho_0} \quad (2.9)$$

where $\rho_{\parallel, \perp}$ is the resistivity in the presence of a B-field applied parallel or perpendicular to the c-axis respectively and ρ_0 is the resistivity without an applied field.

The low-temperature AMR in CMR manganites has been attributed to spin orbit coupling. Some detailed derivations and relatively successful comparison to experiment has been achieved in this direction [36, 76]. Though this method is derived from mixing ferromagnetic impurities in a metallic matrix, it can be adapted to apply to the CMR manganites.

The original microscopic formulation addressing anisotropic magnetoresistance can be attributed to Smit's work in 1951 [36]. The application of an external magnetic field (B-field) splits the otherwise 10-fold degenerate d-orbitals into two 5-fold degenerate manifolds. When addressing transport properties, now a two-current model seems appropriate, with one current belonging to the spin up manifold and one to the group of spin down states.

The energies of these states are governed by the the spin-orbit coupling Hamiltonian (H_{SO}).

$$H_{SO} = AL \cdot S = AL_z S_z + \frac{1}{2}A(L_+ S_- + L_- S_+) \quad (2.10)$$

where A is the spin-orbit coupling constant, \mathbf{L} , \mathbf{S} are the orbit and spin angular momentum operators and L_+ , L_- , S_+ and S_- are the usual raising

and lowering operators for the orbital and spin degrees of freedom. In the perturbative calculations, it is the raising and lowering operators that mix states.

Scattering arises due to mobile spin up electrons interacting with states of mixed spin arising from spin orbit coupling of the d-orbitals. The resistivity is estimated as the square of a scattering matrix element.

While spin orbit coupling seems to compare well to the low temperature magnetoresistive anisotropy, it fails to account for the large peak in the AMR during the MIT. For a discussion of the spin-orbit coupling effects and their suitable application to the manganites, please see Appendix B. Since no model has as of yet been proposed in the literature, a simple phenomenological model is also presented for this quantity in section 5.2.2.

There has been little detailed work focusing on the anisotropy through the MIT. There has been some work revolving around explaining the residual AMR at low temperature [76]. This work essentially follows the work done on metallic alloys with ferromagnetic impurities, not the CMR compounds with the double exchange conduction mechanism. The work demonstrates that there should be roughly 0.85% AMR at low temperatures, which tends to agree with what is seen experimentally to the correct order of magnitude.

No explanation, qualitative or otherwise, has been offered for the effects of oxygen deficiency in thin films of CMR manganites. An interpretation of this effect has been offered in section 5.3.3.

Experimental Procedure and Technical Details

3.1 Film Deposition and Patterning

The LCMO films were deposited by reactive off-axis DC magnetron sputtering. The deposition parameters for the films are listed in Table 3.1. The sputter target was made in-house by a grinding, pressing and sintering process. The doping level of the LCMO target is $x = 0.35$. Off-axis sputtering was used because it helps to prevent re-sputtering of light elements from the film, such as calcium (Ca), and thus improves the control of film stoichiometry.

The films were patterned by conventional lithography. The strong c -axis orientation of the films was confirmed by X-ray diffraction using a Rigaku RTP 300 RC Diffractometer. The results of these X-ray diffraction investigations can be seen in Figure 3.1. These peaks compare well with what is expected for c -axis oriented LCMO films [8]. The additional peak shown in Figure 3.1 is the $[001]$ (c -axis) diffraction peak. This peak shows a c -axis lattice parameter of 3.92 \AA , which is similar to what is expected for the planar spacing in LCMO films on LaAlO_3 (LAO).

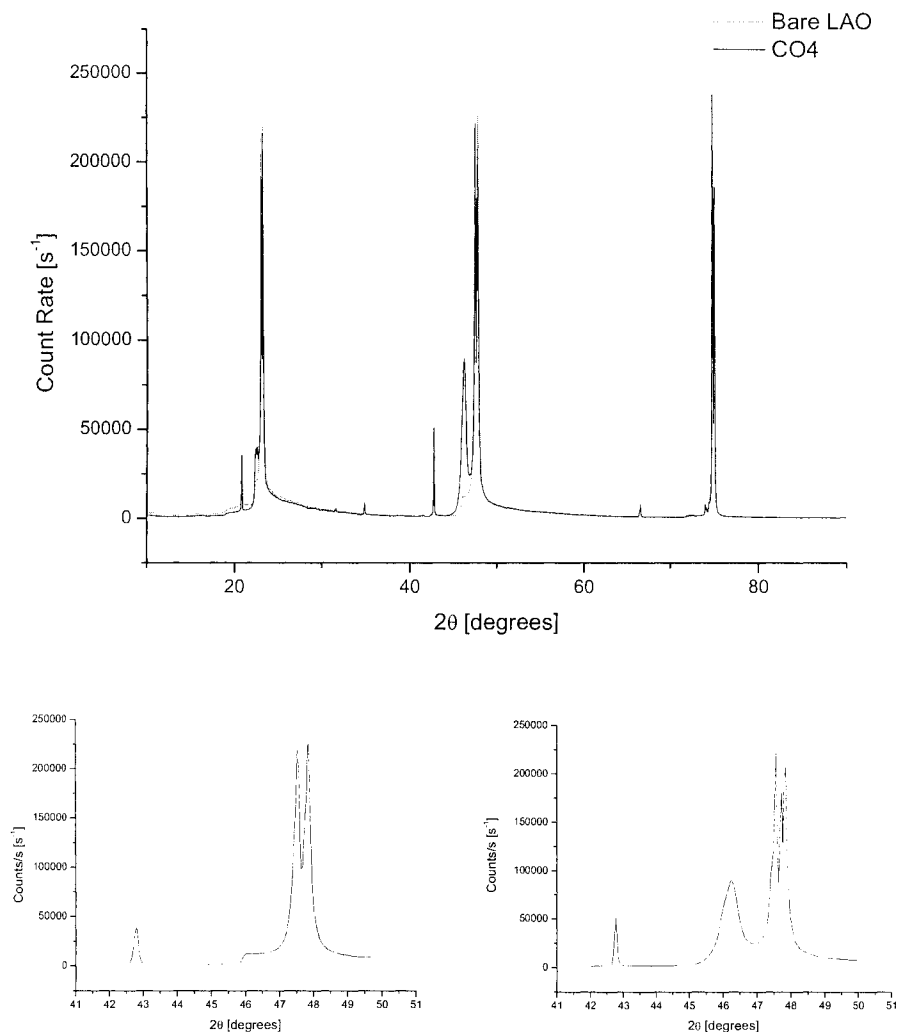


Figure 3.1: X-Ray Spectra of LAO and LCMO on LAO (CO4). The purpose of this plot is to compare the spectra and show the additional strong orientation of the LCMO film. Top: A comparison of the CO4 spectra with that from a bare LAO substrate. Bottom Left: A close up of the LAO spectrum. Bottom Right: A close up of the CO4 spectrum clearly showing the additional peak from the LCMO at 46.24° which corresponds well to the angle expected for good *c*-axis film orientation. The results for CO3 correspond well to what is shown here.

Table 3.1: Off-Axis DC Sputtering Deposition Parameters for LCMO Thin Films CO3 and CO4.

Power:	50 W
Background Pressure:	5×10^{-7} Torr
O ₂ Pressure:	100 mTorr
Ar Pressure:	20 mTorr
Gun Diameter:	1 inch
Substrate Temperature:	750°C
Substrate-Target Distance:	3 cm
Substrate Material:	LaAlO ₃
Anneal Time:	2 hours
Anneal Temp:	650°C
Anneal Environment:	1 atm O ₂

The thickness of the films was measured by contact profilometry using a Tencor Alpha Step 200 profilometer or by optical profilometry using a Zygo Optical profilometer. Two films were made by this process. These films will subsequently be referred to by the names CO3 and CO4. The geometries of these samples are shown in Figure 3.2. Some important parameters of these samples are listed in Table 3.2.

Contact was made to the LCMO thin films through a thin film of sputter-deposited silver (Ag) as a wetting layer and subsequently by pressed Indium

Table 3.2: Dimensions of CO3 and CO4 LCMO Thin Films.

Sample	Parameter	Value
CO3	L ₁	3 [mm]
	L ₂	350 [μ m]
	w	60 [μ m]
	thickness	100 [nm]
CO4	L ₁	6 [mm]
	w	2 [mm]
	thickness	1 [μ m]

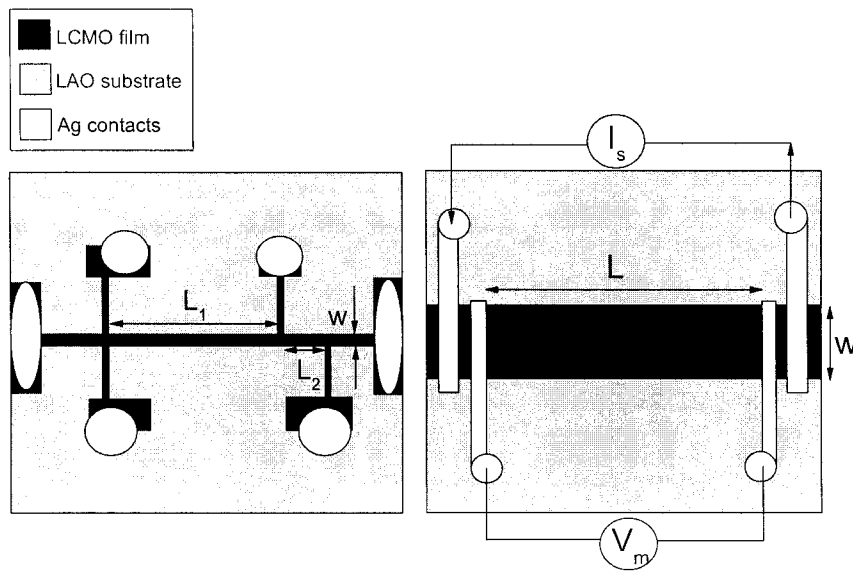


Figure 3.2: LEFT: The geometry of CO3. RIGHT: The geometry of CO4 showing the four-point probe configuration (I_s current source and V_m voltmeter). Some important dimensions are also shown.

(In). It was found that In had better mechanical strength when pressed on Ag than In pressed on aluminium (Al).

3.2 Resistivity and Anisotropic Magnetoresistance Measurements

3.2.1 General Description of the Apparatus

The resistivity versus temperature and the AMR were measured using a four-point probe technique with cryogenic capabilities. Mounted on the cryogenic sample holder is an electrical heater, a sample mount location, a Hall probe and an electrical thermometer.

All instrumentation was controlled and all data was collected by a PC over a GPIB interface using an IEEE card supplied by National Instruments. The data acquisition software was written in Visual Basic (VB) 6.0.

The magnetic field was applied to the sample using a large electromagnet. The magnitude of the magnetic field was measured using a Hall probe mounted on the cryostat near the sample location. Also, the magnitude of the magnetic field was calibrated using a Hall probe at room temperature. This calibration is accurate to a few hundredths of a Tesla. The maximum magnetic field strength safely attainable using the electromagnet is just under 1 Tesla.

A four-point probe measurement technique was used to eliminate contact resistance. This configuration is shown schematically on sample CO4 in Figure 3.2. The current is delivered to the outermost two electrodes and the voltage is measured across the two innermost electrodes. The current to the sample was supplied by a Keithley 236 Source Measure Unit and the voltages were measured using a Keithley 2182 Nanovoltmeter, providing accuracies on the order of nanovolts. The nanovoltmeter is configured so that it uses

the “delta-mode”, meaning that the instrument makes two measurements of opposite polarity in order to cancel thermal Electro-Motive Forces (EMFs) induced in the wires by temperature gradients. The wires measuring the voltage are continuous up to a thermal isolation box, where thermal EMFs across the junction between two metals can be eliminated. Shielded cables are used on critical signals, particularly the voltage and current signals, to minimize induced noise.

The sample can be mechanically rotated in a magnetic field using a stepper motor and the angle measured using an optical encoder. There is a step down gear between the stepper motor and the rotation of the sample that reduces the rotations by a factor of 100. Using this arrangement, the sample can be accurately rotated on the order of hundredths of degrees. The c-axis of the sample was aligned parallel to the magnetic field using a Hall probe. The Hall probe has an angular dependence to its response in an applied magnetic field and it is aligned on the cryostat so that the Hall voltage maximizes when the c-axis of the film is aligned with the field. By rotating the sample in an applied magnetic field and maximizing the voltage from the Hall probe, the c-axis of the thin film can be aligned with the direction of the applied field.

The four-point probe measurement device was mounted onto the end of a standard cryostat dipstick. A large, stainless steel vacuum insulated dewar is used to hold the liquid nitrogen that cools the sample space. This dewar is pumped on by a standard diffusion and roughing pump system. Typically the pressure inside the vacuum insulation is kept to less than 1×10^{-5} Torr.

The temperature was measured using a Silicon-Germanium (SiGe) semiconductor diode. It was calibrated using a standard curve obtained from the manufacturer. This diode thermometer was selected due to its immunity

to the effects of a strong magnetic field. The sample was cooled by Liquid Nitrogen (LN_2) and heated electrically using an inductionless power resistor manufactured by Vishay Inc. The temperature was controlled using a LakeShore DRC-91C PID (Proportional Integral Differential) temperature controller. The range of temperatures safely accessible by the use of this apparatus was between 80 and 320 K.

3.2.2 Temperature Instability and the Addition of a Preheater

At low temperatures, between 80 and 150 K, the initial configuration of the apparatus was sufficient to provide quality data. The apparatus had been optimized for measurements on high T_c superconductors. However, the temperatures of interest for LCMO with a doping level of $x = 0.35$ are between 200 and 300 K. In order to achieve these temperatures with the single resistive heater present in the apparatus, the dewar that cooled the sample could only be partially filled with LN_2 . In this way the appropriate temperatures could be reached but the stability of the temperatures in this region was insufficient to accurately measure the anisotropy. The instability was attributed to two factors: the lack of a large, low temperature thermal reservoir in good thermal contact with the sample and fluctuations due to convection in the sample chamber. In order to improve the temperature stability the dewar would have to be filled completely and more heat would have to be delivered to the LCMO thin film. Simply delivering more power to the existing heater was not an option, as the maximum power that the Vishay resistor could stand, approximately 5 W, was already being delivered at maximum output.

A preheater was incorporated into the apparatus to increase the heating

power and continuous pumping on the sample chamber was introduced to greatly diminish convective temperature fluctuations. The preheater wire was made out of a high resistivity (8.37 Ω/ft) manganin wire that was counter-wound to eliminate induction. That the I-V characteristics of the sample were the same with the preheater on and off demonstrated that any induction from the preheater was negligibly small. In order to function in vacuum the preheater was potted in a thermally conductive paste of ZnO with a thermal conductivity of 0.8 W/m. Without this thermal grounding the heater insulation would burn in vacuum. A copper link between the heater spool, located on the end of the sample canister, and the sample holder. This spool was machined in brass and subsequently silver soldered to the canister. The spool and thermal link were used, instead of a more elegant solution, due to the limited space in the sample holder and on the cryostat.

3.2.3 Software Modifications

In order to quantify the effects of the preheater, the software was modified to take temperature versus time data. A graphical interface was also written to allow for remote control of the preheater. Also, code allowing the transferral of calibration curves between temperature controllers was written. Generally, the user-friendliness of the visual interface was improved. Routines were written to stabilize the temperature. The algorithms used to take AMR data as a function of temperature and AMR were written or updated, as required, to automate the data taking procedure.

3.2.4 Temperature Dependence of the Resistivity

The sample was placed on the end of the cryostat and the four-point probe connections soldered in place using low thermal solder and no flux, as it was found to short the connections. The voltage required to move a constant current through the film over temperatures ranging between 150 and 300 K is measured.

The measurements were made following a step and repeat procedure. The algorithm steps the temperature and waits for it to stabilize. Then a constant current is supplied to the sample, usually 1 or 10 μA , and the voltage is measured in the four-point probe configuration by the nanovoltmeter. All control and data acquisition is done by the visual basic routine on the PC.

These measurements are made in a few different configurations. The first is the Zero Field (ZF) configuration where the orientation of the sample is irrelevant. The second configuration is with the magnetic field applied perpendicular to the film c -axis and parallel to the current ($B \perp c$). The third configuration is with the magnetic field applied parallel to the c -axis and perpendicular to the current ($B \parallel c$). The $B \perp c$ configuration was observed to provide the maximum suppression of the resistivity.

Given the known current and that the dimensions of the film between the contacts, the resistivity of the LCMO film can be easily calculated.

3.2.5 Anisotropy Measurements

Two types of measurements are made. The AMR can be measured as a function of temperature and magnetic field. The arrangement used to measure the resistivity as a function of the angle of an applied magnetic field is shown schematically in Figure 3.3.

To make the measurements, the dependent quantity, either temperature

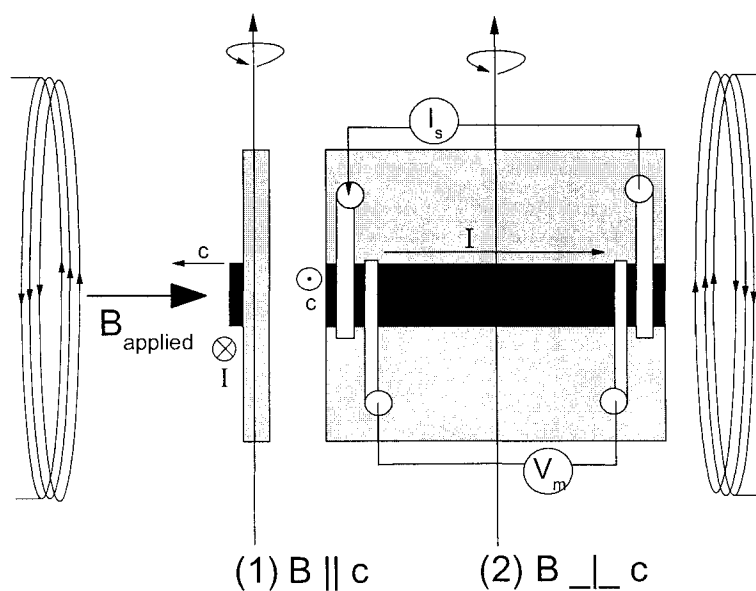


Figure 3.3: A schematic of the arrangement used to measure the AMR is shown. The thin film is rotated mechanically in a magnetic field, typically through 180° . Here (1) shows the $B \parallel c$ orientation, while (2) shows the $B \perp c$ orientation. Both the c - a and c - b planes can be investigated in this way by rotating the sample 90° on the end of the cryostat (take (2) and rotate 90° in the plane of the page).

or B-field, is stepped and stabilized. Then the resistivity is measured as a function of angle. This is done slowly to minimize eddy-current heating. A number of these curves are taken, usually three, and the peak height $\rho_{\parallel} - \rho_{\perp}$ is measured for each curve and then averaged. The data produced from a single scan of the resistivity as a function of field angle is shown in Figure 5.7. This is repeated throughout the range of interest. In terms of temperature, the interesting range for the AMR is between 150 and 270 K. In terms of B-field, measurements are usually made from 0 to 0.86 Tesla. A resistivity curve measured with zero applied field gives ρ_0 . With all this information, the AMR can be calculated according to Equation 2.9.

3.3 Magnetization Measurements

A Quantum Design SQUID magnetometer was used to make the temperature dependent magnetization measurements. The SQUID is cooled by liquid Helium. This instrument measured the magnetization of the thin film CO4. The change in orientation of the film was achieved by manually positioning the film in a different orientation inside a gelatine capsule. While a material like Teflon produces a measurable diamagnetic signal across a wide range of temperatures, gelatine is almost entirely magnetically inert. It has at best a very small diamagnetic contribution to the overall magnetization. This makes it an excellent choice as a sample holder for a magnetometer as sensitive as the SQUID.

This SQUID device is a commercial instrument and so a detailed explanation of its inner workings is omitted here.

Table 3.3: The vacuum annealing history of sample CO3. T_{max} was the maximum temperature seen by the sample, t_{rise} , t_{anneal} and t_{cool} correspond to the rise, anneal and fall times of the temperature and P_b was the approximate background pressure.

T_{max} [°C]	t_{rise} [min]	t_{anneal} [min]	t_{cool} [min]	P_b [mTorr]
320	5	0	18	0.1
345	7	8	18	0.005

3.4 LCMO Film Oxygen Depletion

Film CO3 were annealed in vacuum for a variety of times. The process history of this film is documented in Table 3.3. This annealing was done to remove oxygen from the films.

The MR and AMR were measured between 200K and 270K as before. The locations and magnitudes of the MR and AMR peaks were compared.

The Resistivity in the Transition

4.1 Experimental Results

The standard dependence of the magnetization and the resistivity are obtained for measurements of the thin LCMO films CO3 and CO4. The comparison is shown in Figure 4.1.

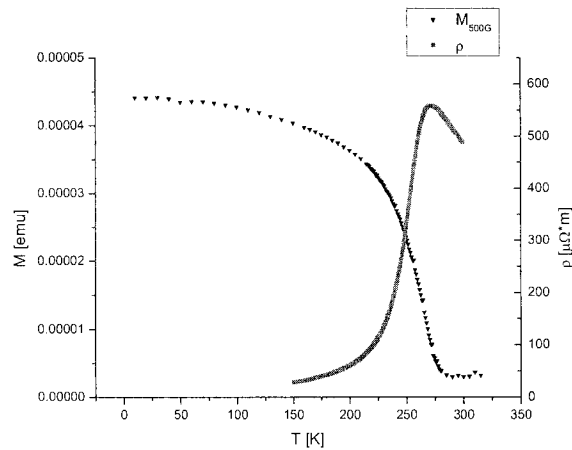


Figure 4.1: A comparison between the resistivity and the magnetization showing the ferromagnetic to paramagnetic transition correlated in temperature with the rise in resistivity. The magnetization was taken in the $B \parallel c$ orientation. The data are from sample CO4.

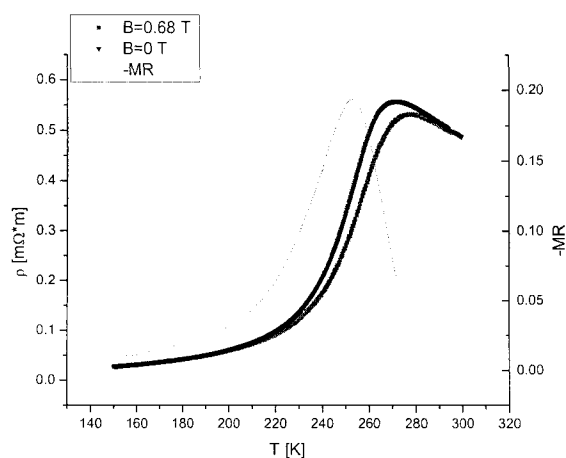


Figure 4.2: The magnetoresistance of the LCMO thin film. A magnetic field of 0.68 T is applied in the $B \perp c$ direction. The maximum negative magnetoresistance ($-MR$) is 19.4%, occurring at 253 K. The data are from sample CO4.

In addition, the magnetoresistance (MR) of the sample, given by Equation 2.4, has the required form, showing a peak near T_c of approximately 20% for an applied field of 0.68 Tesla. The results of this investigation are shown in Figure 4.2.

The resistivity of the thin films of LCMO show the expected dependence, rising by approximately 1.5 orders of magnitude across the MIT. Focus was placed on the transition temperature region, so data was taken between 150 and 300 K. The resistivity data are shown in Figure 4.3.

4.2 Analysis

The purpose of the following derivation is to produce a scattering probability that is a function of temperature. This scattering probability, for large numbers of electrons being scattered, might be comparable to the resistivity of the CMR material. This scattering or trapping probability will be based

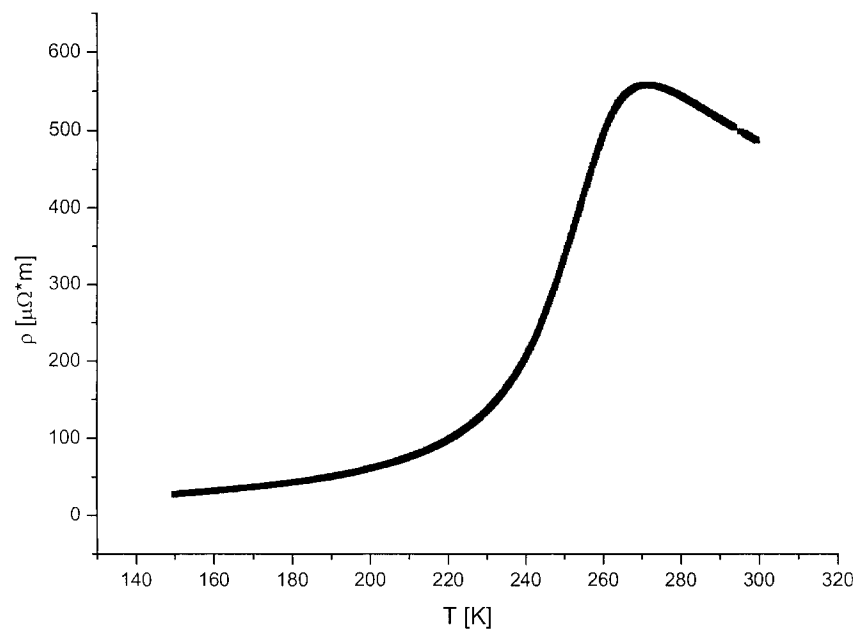


Figure 4.3: The resistivity of thin film LCMO sample CO4 in the absence of an applied magnetic field.

on localizations produced by phonons participating in lattice distortions of a Jahn-Teller type. This work is largely based on material that can be found in some standard textbooks [23, 51].

It has been relatively well established that the double exchange mechanism alone cannot be responsible for the orders of magnitude increase in the resistivity around T_c . Polaronic conduction associated with Jahn-Teller distortions has been widely credited with being responsible for this phenomenon [42, 1, 37]. These phonons are considered to be a diffuse effect, not causing any long range oscillatory order to be present in the lattice. A simplistic analysis of this polaronic effect is presented below, in accordance with the idea of phase separation and in the spirit of the assertion that these materials “should be modelled as a disordered array of phonons” [41].

In what follows, the e_g orbitals are assumed to have energy levels similar to what has been shown in Figure 2.4. The $3z^2 - r^2$ and $x^2 - y^2$ orbitals are usually considered to be non-degenerate. Focus was placed on the $3z^2 - r^2$ orbital in some of the results shown below, but the initial calculations were completed for both orbitals, with similar results.

4.2.1 Polaronic Scattering Probability Derivation

An outline for the basic procedure of this derivation is as follows.

The coordinates in the angular part of the two important e_g orbitals is perturbed by a small time dependence. This time dependent portion is meant to simulate a change in the hybridization or shape of the e_g orbital as a result of neighboring ionic motion. Two types of time dependence are considered, a simple sinusoidal perturbation and a sinusoid localized within a gaussian envelope function. The sinusoid and gaussian combination are meant to simulate a phonon wave packet. Two states are considered in this derivation.

A plane wave state meant to represent a “metallic” double-exchange type electron is analyzed as well as a scattering state composed of a plane and spherical wave. The scattering state is assembled following the standard scattering formulation and represents a scattered, or Jahn-Teller trapped, e_g electron. The scattering amplitude, $f(\theta)$, for the scattering state described above is calculated in the first Born approximation. The matrix elements of the system spanned by the two states above are computed. The off-diagonal matrix elements are time dependent. The dominant terms from these matrix elements are used to compute a transition probability between the plane wave and scattering states in first order time-dependent perturbation theory. This transition probability will be called a “scattering probability.” The scattering probability obtained in this way might apply directly to the resistivity of the material if there was only one mode or frequency of phonon in the lattice. It is well known that the phonon population depends on its density of states and the temperature following Bose-Einstein statistics. An expected scattering probability for incoherent scattering by phonons is then calculated by integrating the scattering probability obtained for a single mode and the density of phononic states, weighted by Bose-Einstein statistics. This produces a scattering probability that is a function of temperature and a few parameters that are taken to be constant. It is these scattering probabilities, given as a function of temperature, that are compared against the resistivity data. Again, for large numbers of electrons being scattered or trapped, these scattering probabilities may compare well to the resistivity in CMR materials.

If the coordinates involved in the angular dependence of one of the e_g orbitals shown in Figure 2.2 are perturbed in time then the following dependence is found.

$$\begin{aligned}
Y_{3z^2-r^2} &= 3 \cos^2(\phi)[1 + u_z(t)] - [1 + u_x(t) \cos^2(\phi) \sin^2(\vartheta) \\
&\quad + u_y(t) \sin^2(\phi) \sin^2(\vartheta) + u_z(t) \cos^2(\phi)] \\
&= 3z^2[1 + u_z(t)] - [1 + u_x(t)x^2 + u_y(t)y^2 + u_z(t)z^2] \quad (4.1)
\end{aligned}$$

$$\begin{aligned}
Y_{x^2-y^2} &= [1 + u_x(t)] \cos^2(\phi) \sin^2(\vartheta) - [1 + u_y(t)] \sin^2(\phi) \sin^2(\vartheta) \\
&= [1 + u_x(t)]x^2 - [1 + u_y(t)]y^2 \quad (4.2)
\end{aligned}$$

where Y_i is the angular portion of the i^{th} orbital and the time dependent function $u_i(t)$ can be considered to be small with the index “ i ” running over the cartesian coordinates.

This representation is meant to simulate on some level the change in the hybridization of the e_g orbitals as a result of ionic motion. The oscillation frequencies can be tuned to simulate the modes given in Figure 2.6 [56]. That requires simply that for the $3z^2-r^2$ case, there is a phase shift of π between the oscillation in the c -axis direction and those in the a - b plane. For the x^2-y^2 orbital, there is a phase difference of π between the oscillations in the a -axis and b -axis directions.

In this investigation, two different types of time dependencies were analyzed. A simple sinusoidal time dependence with an amplitude and a frequency and a sinusoidal time dependence that was localized within a gaussian envelope function were both considered.

$$u_{1,(x,y,z)}(t) = A_1 \cos(\omega_{x,y,z}t + \delta) \quad (4.3)$$

$$u_{2,(x,y,z)}(t) = A_2 \exp(-\alpha t^2) \cos(\omega_{x,y,z}t + \delta) \quad (4.4)$$

where A_i is some small amplitude, ω is the perturbing angular frequency, δ is any phase shift between oscillations in the x, y or z, t is time and alpha is a parameter that scales the width of the gaussian in Equation 4.4. For the remainder of this analysis, Equation 4.3 will be referred to as a “*sinusoidal*” perturbation or scattering mechanism, while Equation 4.4 will be referred to as a “*gaussian*” perturbation or scattering mechanism. Equation 4.3 was analyzed because it is the simplest oscillating perturbation possible, and as such might make a good starting point. The analysis of the gaussian perturbation, Equation 4.4, is probably the closest representation of phonons in the lattice. Phonons propagate through the lattice as local atomic oscillations. At any given Mn atomic site, the disturbance due to a passing phonon will not be permanent, but will grow, last for some length in time and then die away. Equation 4.4 is meant to simulate this. It yields some of the most interesting results present in this analysis.

Using the first Born approximation, a scattering amplitude for conduction electrons scattering off of each time dependent e_g orbital was calculated. Two states were considered. A plane wave state meant to approximate a conduction electron and a scattering state represented by a plane wave and spherical wave combination were used. The scattering state is given from the standard scattering formulation [23]. The plane wave approximation is meant to model a “double-exchange type” electron that moves easily through the lattice. The scattering state is meant to model a scattering or trapping event of a Jahn-Teller type. Transitions between these two states are analyzed in

an attempt to model the scattering or trapping events that occur in these materials due to ionic motion.

$$\phi_1 = A_1 e^{i\vec{k}\cdot\vec{r}} \quad (4.5)$$

$$\phi_2 = A_2 e^{i\vec{k}\cdot\vec{r}} + f(\theta, t) \frac{e^{i\vec{k}\cdot\vec{r}}}{\vec{r}} \quad (4.6)$$

where \vec{k} is the electron wavevector, and $f(\theta, t)$ is the scattering amplitude. The scattering amplitude calculated ended up being only a function of time. The momentum transfer term (\vec{K}) was found to always have an even exponent of order two or greater, making it a scalar quantity.

$$f_{eg0}(\theta, t) = A \left(\frac{(5K^2 - C^2)u_x(t) + 2(K^2 + C^2)u_y(t)}{(K^2 + C^2)^4} - \frac{4(5K^2 - C^2)u_z(t) + 24K^2}{(K^2 + C^2)^4} \right) \quad (4.7)$$

$$f_{eg2}(\theta, t) = B \left(\frac{2(5K^2 - C^2)u_x(t) - 8(2K^2 - C^2)u_y(t)}{(K^2 + C^2)^4} \right) \quad (4.8)$$

$$\begin{aligned} \text{where } A &= \frac{-12m}{\sqrt{6}\hbar\pi^{\frac{3}{2}}} C^4 \\ B &= \frac{-2m}{27\hbar\pi^{\frac{1}{2}}} C^4 \\ \vec{K} &= \vec{k}' - \vec{k} \\ C &= Z/a_0 \end{aligned}$$

where \vec{K} is the momentum transfer, \vec{k} is the original wavevector, \vec{k}' is the final wavevector, Z is the atomic number, a_0 is the Bohr radius, m is the mass of the electron and \hbar is the familiar Planck constant.

Using this time dependent scattering amplitude, and the system spanned by the states of Equation 4.5 and 4.6, the time dependent matrix elements for these states were computed. This was done as a continuation of this analysis presented for the purposes of this report. The eigenvalues of this matrix can also be found, though they are prohibitively long and so are not shown. Here, only the matrix for the $e_{g,0}$ orbital is shown.

$$H'_{eg0}(t) = \begin{pmatrix} \frac{8(6\pi)^{\frac{1}{2}} U_{x,y,z}}{C^{\frac{3}{2}}} & \frac{2(6\pi)^{\frac{1}{2}} (\frac{12}{C} + f(t)) U_{x,y,z}}{3C^{\frac{1}{2}}} \\ \frac{2(6\pi)^{\frac{1}{2}} (\frac{12}{C} + f(t)) U_{x,y,z}}{3C^{\frac{1}{2}}} & \frac{8(6\pi C)^{\frac{1}{2}} (\frac{108}{C^2} + \frac{18f(t)}{C} + f(t)^2) U_{x,y,z}}{81} \end{pmatrix} \quad (4.9)$$

$$\text{with } U_{x,y,z}(t) = (u_x(t) - 4u_z(t) + 5u_y(t))$$

Using the off-diagonal matrix elements, the transition probability from a plane wave state to a scattering state was computed in first order time dependent perturbation theory. This is an appropriate tool for LCMO and CMR materials because it is known that the mean free path of electrons in these materials is very short [55]. Therefore, to use the Drude terminology, the τ_{drift} , the time between scattering events, is very small.

The analysis was done for the case of $K/C \gg 1$ and $K/C \ll 1$, in the limit of large momentum transfer and small momentum transfer respectively. In each case, and for each orbital, some dominant terms can be chosen. Each one of these terms individually, yield a time dependence and a constant that is linear in the time dependent perturbation. In terms of time dependence, the $K/C \gg 1$ and the $K/C \ll 1$ seem to share some symmetry for both the $3z^2 - r^2$ and the $x^2 - y^2$ orbitals. The scattering probabilities for the different K/C limits are shown for the $3z^2 - r^2$ orbital in Equations 4.10 and 4.11.

$$\text{if } \frac{K}{C} \ll 1, \quad P_{trans} \approx \frac{-8\sqrt{6\pi}C^{\frac{13}{2}}(4u_z - 5u_y - u_x)}{(K^2 + C^2)^4} \quad (4.10)$$

$$\text{if } \frac{K}{C} \gg 1, \quad P_{trans} \approx \frac{8\sqrt{6\pi}K^8(4u_z - 5u_y - u_x)}{C^{\frac{3}{2}}(K^2 + C^2)^4} \quad (4.11)$$

Sinusoidal Perturbation

Now first order time dependent perturbation theory can be applied term by term on the dominant terms in the off-diagonal matrix elements. At this point, the specific form of $u(t)$ becomes important. For a $u(t)$ that is a simple sinusoid, such as that given in Equation 4.3, the standard transition probability, $P_{a \rightarrow b}$ is arrived at [23], which will describe the transition probability over short time periods.

$$P_{a \rightarrow b} = \frac{|V_{ab}|^2 \sin^2[(\omega_0 - \omega)\frac{t}{2}]}{\hbar^2 (\omega_0 - \omega)^2} \quad (4.12)$$

where t is the time, ω is the frequency of the perturbation, V_{ab} is the energy expectation value of the time independent portion of the perturbation. The amplitude A_i , shown in Equations 4.3 and 4.4, of the time dependent perturbation have been absorbed here as well. The quantity ω_0 is equal to to [23]

$$\omega_0 = \frac{E_b - E_a}{\hbar} \quad (4.13)$$

where E_a and E_b are the energies of the plane wave and scattering states respectively. Throughout the entirety of the report, E_a will be considered to be positive, while the sign of E_b is defined relative to E_a .

If only one phonon mode existed in the lattice this might be the end of the story. However, it is known that as the temperature rises, phonons begin to populate higher energy states. Since the phononic contribution to the

resistivity is expected to be an incoherent perturbation, an integral of the form of Equation 4.14 can be evaluated in order to find the total scattering probability, in this case, as a function of temperature. A similar procedure has been followed to study the absorption and emission of electromagnetic radiation [23].

Here the upper bound of integration has been set to infinity. No Debye-like cut-off frequency is necessary. Integration is being performed, so the phonons are considered to have a continuous spectrum of energies. Given the relatively high T_c that CMR materials display, the continuum approximation is likely a good one.

$$\langle P \rangle = \frac{|V_{ab}|^2}{\hbar^2 N} \int \frac{\sin^2[(\omega_0 - \omega)\frac{t}{2}]}{(\omega_0 - \omega)^2} g(\omega) n(\omega) d\omega \quad (4.14)$$

where the $g(\omega)$ used is the density of states in three dimensions. This choice is justified by the exponent on the magnetization on Figure 5.4, since the mean-field approximation seems to have some merit in describing the magnetic phase transition and the mean-field model works better for systems of large dimension. The quantity $n(\omega)$ represents the average occupation number given by Bose statistics. While a more detailed density of states would be a definite asset in the following calculation, it seems to be sufficient to use this parabolic approximation.

The density of states for phonons in three dimensions and the standard Bose statistics for phonons are given in Equations 4.15 and 4.16 respectively.

$$g(\omega) = \frac{3\omega^2}{2\pi^2 c^3} \quad (4.15)$$

$$n(\omega) = \frac{1}{e^{\beta\hbar\omega} - 1} \quad (4.16)$$

The integral in Equation 4.14 is most easily evaluated by expanding the integrand as a series. The $n(\omega)$ and the $\sin[(\omega_0 - \omega)t/2]$ must be expanded. If this is done, three integrals are obtained.

These integrals can be evaluated if the index on the Taylor expansion in the $\sin[(\omega_0 - \omega)t/2]$ is equal to the index on the expansion in the geometric series for the partition function (ie: $n = m$). This has the effect of weighting the probability of having a phonon near the frequency required to trap an electron by a JT-type distortion by $\sim (\omega_0 - \omega)^n$. For terms of high order in the expansion, this weighting factor will become small very rapidly. Physically, this can be interpreted as meaning that high energy phononic modes are not allowed to participate in the JT distortion.

If this approximation is made then Equation 4.17 is obtained.

$$\langle P \rangle = \frac{|V_{ab}|^2}{4\hbar^2 N} \sum_n^{\infty} \frac{(\frac{t}{2})^{4n-2} e^{\beta\hbar\omega_0(n+1)}}{[(2n+1)!]^2} \int_{\omega_0}^{\infty} (u^2 + 2\omega_0 u + \omega_0^2) u^{4n-4} e^{-\beta\hbar u(n+1)} du \quad (4.17)$$

where β is the familiar $\frac{1}{kT}$, with k as Boltzmann's constant and T as the temperature, and N is equal to the total number of phonons present, the usual normalization integral in $g(\omega)$ and $n(\omega)$.

$$N = \int g(\omega)n(\omega) d\omega \quad (4.18)$$

If the integral in Equation 4.17 is evaluated many powers of the temperature as well as special functions in temperature are obtained. The special functions are called the Whittaker "M" functions and are the solution to the differential equation given in 4.19. This function has a series expansion given by 4.20.

$$\frac{d^2 y}{dz^2} + \left(-\frac{1}{4} + \frac{\mu}{z} + \frac{\frac{1}{4} - \nu^2}{z^2} \right) = 0 \quad (4.19)$$

$$\begin{aligned} \text{Whittaker } M(\mu, \nu, z) = & z^{\frac{3}{2}} - \frac{1}{3} z^{\frac{5}{2}} + \frac{7}{96} z^{\frac{7}{2}} - \frac{1}{96} z^{\frac{9}{2}} + \frac{11}{9216} z^{\frac{11}{2}} \\ & - \frac{1}{9216} z^{\frac{13}{2}} + \frac{5}{589824} z^{\frac{15}{2}} - \dots \end{aligned} \quad (4.20)$$

with $\mu = \nu = 1$

where μ, ν are just index quantities. In this derivation, β forms a part of the z variable given in Equation 4.20. Given that β is inversely proportional to T , this means that increasing powers of β give increasing powers of $1/T$. As a result, the infinite series expansion of the Whittaker “M” functions will converge as a function of T .

Taking all the functions of temperature obtained by this method, including the special functions, gives a sum. The sum in Equation 4.17 converges quite rapidly for increasing n , as shown in Figure 4.4. For small β , the curve takes longer to converge, as shown in Figure 4.4. So a detailed understanding of the relative size of β is important in interpreting this analysis. Relative to \hbar , β will definitely be large, so it is likely that the rapidly converging dependence portrayed in Figure 4.4 is the correct one for the derivation being offered here.

The first three terms of the sum obtained from Equation 4.17 are used to produce a scattering probability. Terms with temperature dependences ranging from T^{-5} to T^8 are obtained. The leading order terms are shown in equation 4.21. These terms are meant mainly to give an example of the powers of T involved and some of the coefficients. However, the terms in equation 4.21 are given without the corresponding normalization constants.

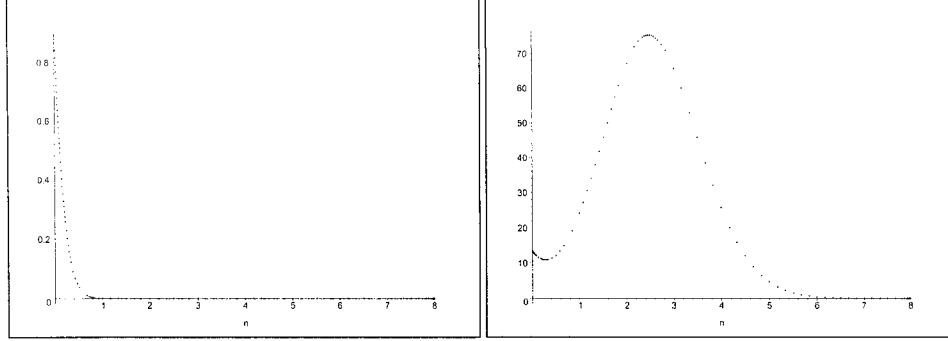


Figure 4.4: Convergence of Series used to estimate phononic scattering for the sinusoidal perturbation with LEFT: $\beta = 1$ and RIGHT: $\beta = 0.1$.

So while at first glance they may seem immensely large, there are small constants not shown here that will bring these terms back to a reasonable magnitude. The most important thing is what has been obtained in terms of the leading powers of T.

$$\begin{aligned} \langle P \rangle \approx & \frac{2.57x10^{-7}t\omega_0^2k^6}{(\hbar)^6}T^6e^{-\frac{3\hbar\omega_0}{kT}} + \frac{1.02x10^{-6}t\omega_0k^7}{(\hbar)^7}T^7e^{-\frac{3\hbar\omega_0}{kT}} \\ & + \frac{1.20x10^{-6}tk^8}{(\hbar)^8}T^8e^{-\frac{3\hbar\omega_0}{kT}} \end{aligned} \quad (4.21)$$

Equation 4.21 gives a scattering probability curve that has a dependence shown in Figure 4.5. The shape of this curve is reminiscent of the rise in the resistivity of LCMO near T_c . The analysis is limited in that the curve diverges with a temperature dependence of $\langle P \rangle \propto T^8$.

To maximize the scattering, the terms making up the curve shown in Figure 4.5 can be differentiated with respect to T. This leaves only two undefined parameters, ω_0 and T. In the roots of this equation, ω_0 can be isolated. If this is done, to first order, the relationship

$$\omega_0 \approx \frac{-0.889kT}{\hbar} \quad (4.22)$$

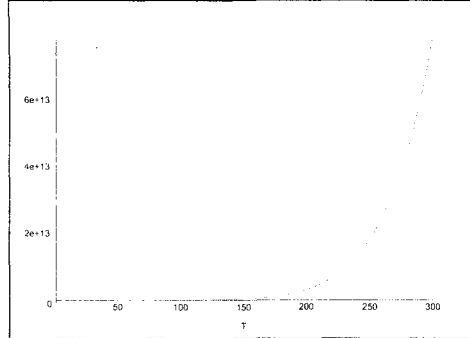


Figure 4.5: The total integrated scattering probability for the sinusoidal perturbation with $\hbar, k, \omega_0, t = 1$.

is obtained.

This means that the energies involved in the scattering process, at least over the temperature regime where the sinusoidal perturbation of Equation 4.3 and the subsequent approximations made up to this point are appropriate, are given by

$$E_b = E_a - 0.889kT \quad (4.23)$$

To second order, the natural frequency ω_0 is

$$\omega_0 \approx \frac{(-1.167 + 0.844i)kT}{\hbar} \quad (4.24)$$

This analysis shows that the energy difference ω_0 is a function of temperature. Interpreting the second root, which has an imaginary component, is a bit troubling. The particle energies are observables, and so they should not have any imaginary components or phase angles associated with them. That this second order root has an imaginary component may just be an artefact of this analysis, showing simply that it is limited to making predictions to first order. However, the important consequence of this work is that it shows

that the energy splitting between the plane wave and the scattering states of electrons in the case of a time dependent e_g orbital is a direct function of temperature. This dependence, to first order in time dependent perturbation theory, is linear in temperature.

Perturbation in a Gaussian Wavepacket

Now the results from the case of the second time dependence given in Equation 4.4, a sinusoidal perturbation localized in time within a gaussian envelop function, can be presented.

The transition probability, calculated from first order time dependent perturbation theory, can be found. Here the limits of integration were expanded to infinity, since the gaussian certainly converges for large times. Perhaps not surprisingly, the frequency dependence of the transition probability is gaussian, given that perturbation theory with these expanded limits amounts to taking the Fourier transform of the scattering probability, and the Fourier Transform of a gaussian is a gaussian.

$$P_{a \rightarrow b} = \frac{\pi V_{ab}^2}{16\alpha\hbar^2} e^{-\frac{(\omega_0^2 + \omega^2)}{2\alpha}} \cosh\left(\frac{\omega_0}{\alpha}\omega\right) \quad (4.25)$$

If $\alpha \ll \omega_0$ then $\cosh\left(\frac{\omega_0}{\alpha}\omega\right) \approx 1 \approx \cos\left(\frac{\omega_0}{\alpha}\omega\right)$. Expanding $\cos(x)$ with Euler's identity now gives a complex quantity in the exponent. That $\alpha \ll \omega_0$ will be shown conclusively in the results section in Table 4.3.

This is the scattering dependence in the frequency domain. Again, it has essentially been Fourier transformed from the time domain by a slight modification to the application of time dependent perturbation theory. Now the dependence must be transformed from the frequency domain to a dependence in temperature, or the quantity β , for the equilibrium distribution of microstates for scattering involving phonons. To this end, $n(\omega)$ can be

modified to transform from coordinates in ω to coordinates in β .

$$n(\omega) = \sum_n^{\infty} e^{i\beta\hbar\omega n} \quad (4.26)$$

where i is the $\sqrt{-1}$, the sum runs over all phonon modes participating in the JT distortion and \hbar has been used to ensure correct units.

This gives an integral for the weighted average of the transition probability of

$$\langle P \rangle = \Omega \int_0^{\infty} e^{-\frac{(\omega_0^2 - \omega^2)}{2\alpha}} \cos\left(\frac{\omega_0}{\alpha}\omega\right) g(\omega) n(\omega) d\omega \quad (4.27)$$

with $\Omega = \frac{3V_{ab}^2}{32N\pi\alpha\hbar^2c^3}$

where the limit has been expanded to ∞ since the gaussian envelope most certainly drops quickly to zero away from ω_0 . This integral can be handled by completing the square in the exponent of the integrand that arises.

$$\langle P \rangle = \frac{\Omega}{2} \sum_n^{\infty} \int_{-\infty}^{\infty} \omega^2 e^{-\frac{\omega_0^2 - \omega^2 + i\frac{\omega_0}{\alpha}\omega - i\frac{\omega_0}{\alpha} - 2i\alpha\beta\hbar\omega(n+1)}{2\alpha}} \quad (4.28)$$

This can be evaluated to a closed form solution.

$$\langle P \rangle = \Lambda \sum_n^{\infty} e^{-\left(\frac{\omega_0^2}{\alpha} + \frac{\alpha(\hbar n)^2}{2(kT)^2}\right)} \left[B_+ e^{\frac{n\hbar\omega_0}{kT}} + B_- e^{-\frac{n\hbar\omega_0}{kT}} \right] \quad (4.29)$$

$$\text{with } \Lambda = \frac{3\sqrt{2}V_{ab}^2}{64\sqrt{\pi}c^3}$$

$$B_{\pm} = \left(\pm \frac{2n\sqrt{\alpha}\omega_0}{\hbar kT} - \frac{\alpha^{\frac{3}{2}}n^2}{(kT)^2} - \frac{\omega_0^2 - \alpha}{\sqrt{\alpha}\hbar^2} \right)$$

This is a series solution with two independent parameters, ω_0 and α , as well as a dependence on the temperature. For large α and given that \hbar is

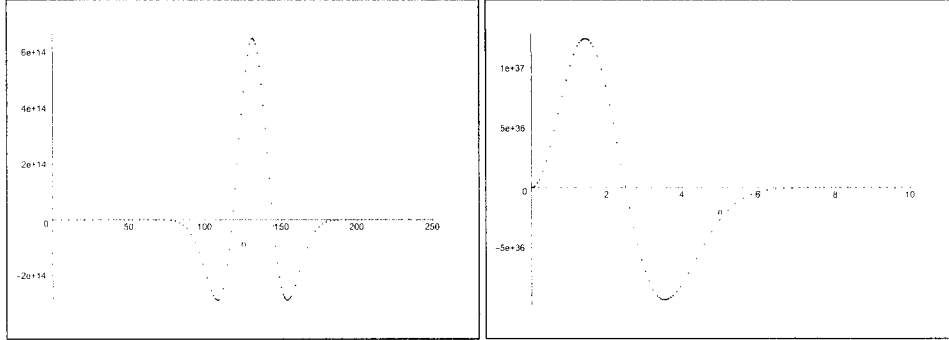


Figure 4.6: The convergence of the Gaussian scattering probability with $V_{ab} = 1 \times 10^{20}$, $c = T = 1$, $\omega_0 = 1 \times 10^{11}$ and LEFT: $\alpha = 1 \times 10^{21}$, RIGHT: $\alpha = 1 \times 10^{22}$.

small, the series converges relatively rapidly in n . An idea of the dependence of the convergence on α can be seen in Figure 4.6. Since this analysis is based on a perturbative approach, it is reasonable to expect that the equations derived, such as Equation 4.29, will be valid over small regions in the temperature.

It is desirable to analyze the dependence of ω_0 in the vicinity of the scattering peak. This region is expected to correspond to the metal-insulator transition. If just the first term of the series expansion given in Equation 4.29 is differentiated with respect to T and solved for ω_0 , the following dependence for ω_0 is obtained.

$$\omega_0 \approx \pm \frac{2\alpha\hbar}{kT} \quad (4.30)$$

This is the temperature dependence of ω_0 for $T \sim T_c$. To look at what is happening below T_c , T can be scaled by T_c . By scaling T so that the limit as $T \rightarrow T_c$ can be investigated, the following dependence is found.

$$\omega_0 \approx \frac{-2\alpha\hbar}{kT(\frac{T_c}{T} - 1)} \quad (4.31)$$

In terms of the energies, Equation 4.31 gives

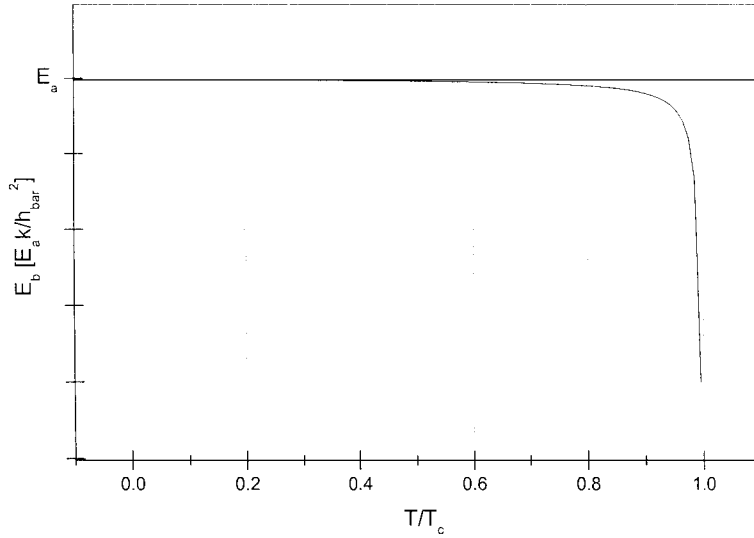


Figure 4.7: The scattering state energy E_b for an e_g orbital subjected to a time disturbance localized within a gaussian envelope function.

$$E_b = E_a - \frac{2\alpha\hbar^2}{kT(\frac{T}{T_c} - 1)} \quad (4.32)$$

This dependence is shown in Figure 4.7. At low temperatures, the energy of the scattering state, E_b is comparable to that of the plane wave state, E_a . However, near T_c there is a divergence in the energies, and the scattering state becomes much lower in energy than the plane wave state. This makes the scattering state the preferred state for the electrons near the transition.

Plots made based on Equation 4.29 are shown in Figures 4.8, 4.9 and 4.10.

There are two important features that Equation 4.29 can be made to reproduce. Using the appropriate ratio of $\frac{\alpha}{\omega_0}$, a plot like Figure 4.8 can be made. It is immediately apparent that this curve is only applicable to the initial stages of the phase transition, as it does not rise very fast and fails to maximize at T_c . However, it can be seen that this initial curve shape is

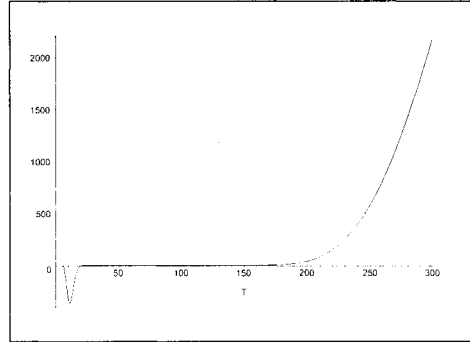


Figure 4.8: The initial curve shape of the gaussian scattering probability is shown for $\omega_0 = 3.9 \times 10^{12}$ and $\alpha = 1.5 \times 10^{25}$. One can see that it does not rise fast enough or maximize, but that it does begin to rise at the right temperature, with the correct curvature for the initial portion of the resistivity curve. Note that it also predicts a large unphysical spike at low temperatures. This is likely due to asymptotic deviations of the terms near $T=0$. For larger numbers of terms, this spike is reduced.

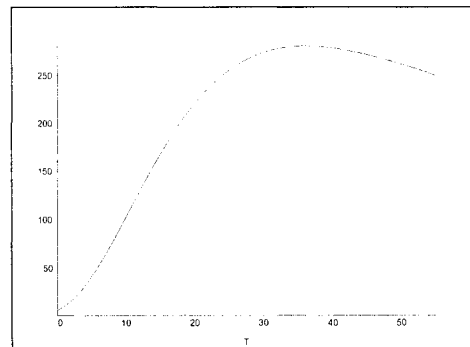


Figure 4.9: The high temperature dependence of the scattering probability for a time dependent disturbance localized within a gaussian envelope function. The curve has been shifted so that the peak is roughly centered at T_c . The parameters used are $\omega_0 = -3.8 \times 10^{11}$ and $\alpha = 1.5 \times 10^{23}$.

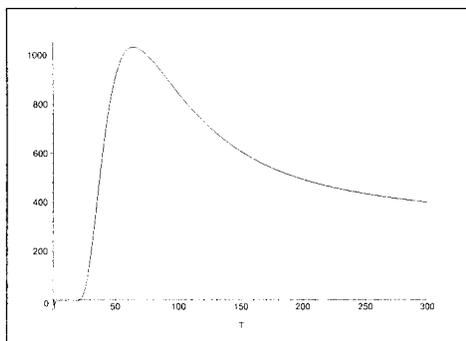


Figure 4.10: The scattering probability appears thermally activated for a time dependent disturbance localized within a gaussian envelope function above the resistivity peak. The parameters used are $\omega_0 = -3.8 \times 10^{11}$ and $\alpha = 1.5 \times 10^{23}$.

somewhat reminiscent of the resistivity increase in the onset of the transition region.

Near T_c , the resistivity maximizes. In this region the dependence should look like that shown in Figure 4.9. This curve is again made by choosing the appropriate ratio of $\frac{\alpha}{\omega_0}$, which in this case is negative.

Also, Equation 4.29 reproduces the “thermally activated” or “semiconductor-like” exponential decay that has been shown experimentally at high temperatures in these materials. However, Equation 4.29 fails to reproduce anything like T_c and the exponential decay expected above T_c simultaneously.

Final Comments on the Derivations

These derivations were done for a few reasons. It was interesting to pursue some ideas surrounding phononic contributions to resistivity, and this analysis does demonstrate that some interesting results can be obtained in this direction. However, beyond any other reason the primary idea shown by this work is that perturbations in time can correspond to energies that are functions of temperature. These perturbations can form a significant portion

of the particle energy at high temperatures. As a result the argument can now be made that these energies should be a part of the numerator of the exponent on any Boltzmann factor, and in any partition function, that might be written about these materials.

$$P_i \propto e^{\frac{f(T)}{kT}} \quad (4.33)$$

This formulation will become central to the arguments made with respect to the AMR in section 5.2.2.

4.2.2 Resistivity Curve Fitting

The leading order terms of the expansion for the straight sinusoidal perturbation given in Equation 4.21 are used to fit the resistivity data between 150 and 245 K. The result is shown in Figure 4.11. The powers of T found in this expansion are interpreted as different polaronic scattering processes [40, 75], and as such are not necessarily going to have the same times associated with them. Given this interpretation, the time parameter was allowed to be different for each of the leading order terms in T. Fits were attempted using the lower powers of T as well. These lower powers of T were found not to contribute in a meaningful way to the resistivity. Also, a residual resistivity term was added to Equation 4.21, but was found to be very small.

The resistivity from 150 to 245 K and 245 to 300 K was fit using the gaussian expansion given in Equation 4.29. The results are shown in Figures 4.12 and 4.13. The first sixteen terms of Equation 4.29 are used. While the data was scaled to assist with the fitting, no other modification to the derived result was performed.

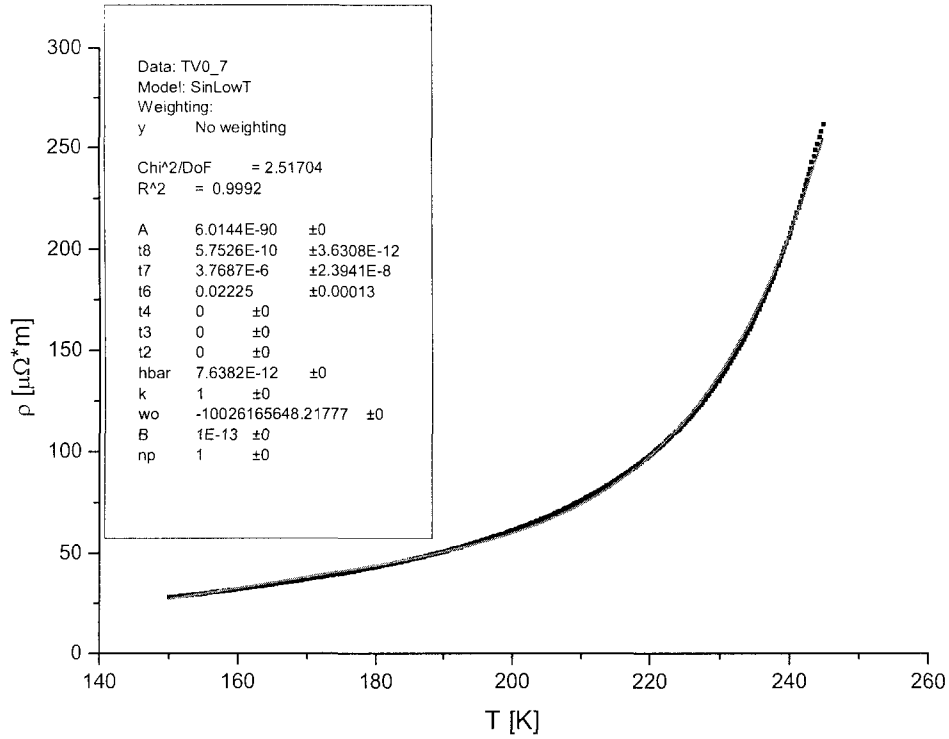


Figure 4.11: The resistivity in the onset of the MIT is fit using the sinusoidal scattering probability. The first three leading order powers of T contribute, T^8 , T^7 , T^6 . It can be seen that even for these high powers of T , close to T_c the fit still suffers from not rising fast enough. Note that ω_0 is an order of magnitude smaller in this case, relative to the resistivity near the peak. The data are from CO4.

Table 4.1: Parameters for the Fit from Equation 4.21 for Temperatures between 150 K and 245 K.

Parameter Name	Value
A	6×10^{-90} (Normalization)
t_8	5.8×10^{-10}
t_7	3.8×10^{-6}
t_6	2.2×10^{-2}
ω_0	$\sim -1 \times 10^{10} \text{ [s}^{-1}\text{]}$
ρ_0	$1 \times 10^{-13} \text{ [\Omega m]}$

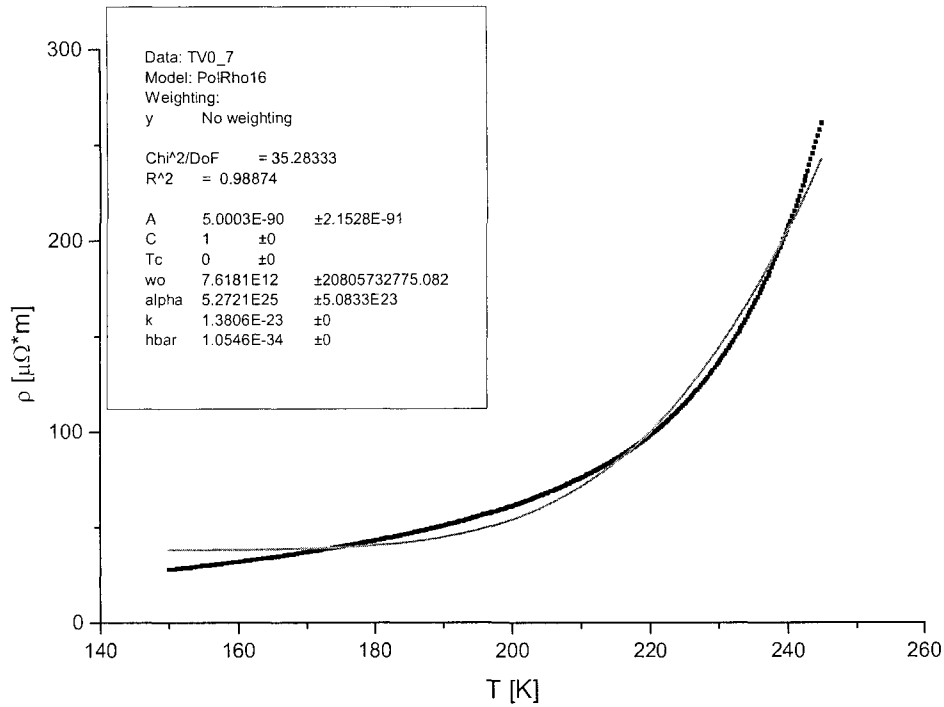


Figure 4.12: The resistivity about T_c is fit using the gaussian scattering probability derived in the Theory section. The first 16 terms in the expansion were used for this fit. Note that it does not fit very well, likely because other scattering mechanisms are omitted. Also note that ω_0 is positive for this fit. The data are from CO4.

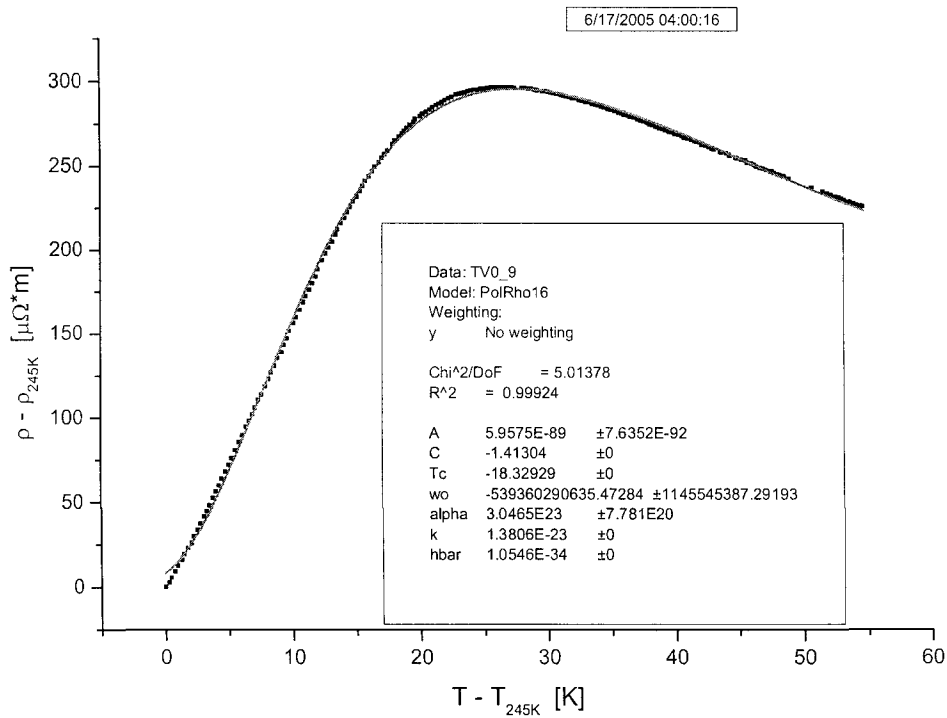


Figure 4.13: The resistivity data is found to be proportional to the gaussian scattering mechanism. Note that the peak area as well as near onset of the change in resistivity are the two places where this curve fails to fit the data very accurately. Also, for this fit ω_0 is now small and negative. Also, the parameter α has grown smaller, meaning that the lifetime of the JT distortions has increased. The data are from CO4.

4.3 Discussion

The advantage of the formulation offered in section 4.2.1 is its simplicity and its analytical nature. It offers a basic and accessible physical picture in which to think about the onset of polaronic charge transport. It also appears to do a reasonable job predicting the resistivity over small regions of temperature in the transition region.

From the resistivity fits shown in Figures 4.11, 4.12 and 4.13, it has been shown that the best agreement at low temperatures corresponding to the onset of the MIT is obtained from the sinusoidal scattering mechanism given roughly by Equation 4.21. At high temperatures, near and above T_c , the resistivity is fit best by the gaussian scattering probability given in Equation 4.29. This is summarized in Figure 4.14.

The sections below are structured in the following way. First, the numerical results from the three fits shown in Figures 4.11, 4.12 and 4.13 are discussed. Then, in section 4.3.3, other work such as numerical modeling and semi-analytical approaches are briefly discussed.

4.3.1 Low Temperature Fits in the Onset of the MIT

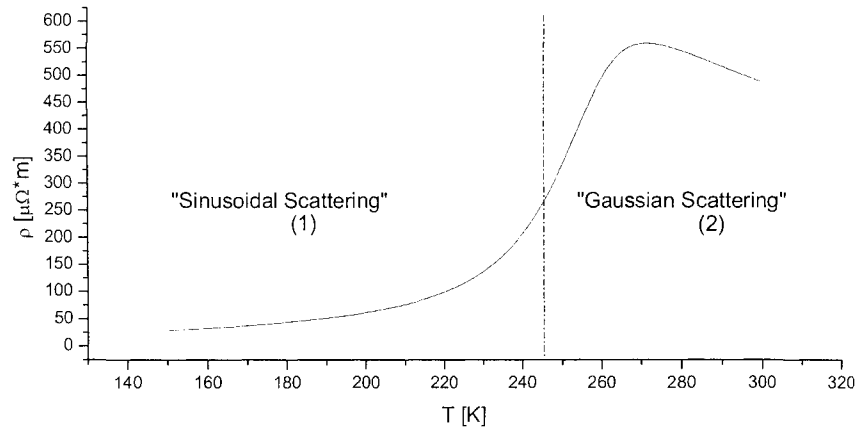
Two fits were performed to the resistivity of LCMO at the onset of the MIT. One was made from Equation 4.21 which is based on a time disturbance given by Equation 4.3, or the “sinusoidal” dependence. The second fit was

Table 4.2: Parameters for the Fit from Equation 4.29 for Temperatures between 150 K and 245 K.

Parameter Name	Value
A	5×10^{-90} (Normalization)
α	5.27×10^{25} [s ⁻²]
ω_0	7.62×10^{12} [s ⁻¹]

Table 4.3: Parameters for the Fit from Equation 4.29 for Temperatures between 245 K and 300 K.

Parameter Name	Value
A	6×10^{-90} (Normalization)
α	3.047×10^{23} [s ⁻²]
ω_0	-5.39×10^{11} [s ⁻¹]

Figure 4.14: The resistivity is best fit at low temperatures by the sinusoidal scattering probability and at high temperatures by the gaussian scattering probability. The crossover occurs at $T \approx T_c$.

made based on Equation 4.29, derived from perturbing an e_g orbital with a time dependence given by Equation 4.4, which has been called the “gaussian” dependence.

The Sinusoidal Scattering Probability

From the fit of the scattering probability computed from the simple sinusoidal perturbation (Equation 4.21) to the resistivity data between 150 and 245 K, shown in Figure 4.11, some times are found. These times, along with all other analytical results, are listed in Table 4.1. For the highest order power of temperature, T^8 , a short time is found relative to the times associated with other lower powers. Given the interpretation that this expansion in T involves electron phonon processes, this power may correspond to some very fast JT trapping process involving the overlap of numerous phonons at the same site in the lattice. The other powers of temperature seem to correspond to processes that are much longer lived.

The value of ω_0 obtained from the fit gives an energy difference between double exchange carriers and JT polarons of $\sim -6.6 \times 10^{-6}$ eV. This is an extremely small energy difference. Also, there is some ambiguity surrounding the obtained value of ω_0 . Given the number of free parameters, any value of ω_0 found can be offset by the times selected in the fit.

The terms given in Equation 4.21 fit the low temperature resistivity quite well between 150 K and 245 K, though it can be seen that there starts to be a discrepancy close to 245 K. However, this analysis would never predict that the resistivity would maximize as a function of temperature, given that the powers of T obtained tend to give a resistivity that diverges as T^8 .

There are numerous powers of T given in the sinusoidal derivation that do not immediately lend themselves to a physical interpretation. The power

T^5 is considered to be an acoustical phonon mode, and it is absent from the expansion. Other integer powers of T derived can not immediately be linked to a specific physical explanation. However during the derivation of Equation 4.17 one of the approximations made was that the indices in the two expansions were the same (“ $m = n$ ”). This had the effect of limiting the contributions from phononic modes of high order (large n) to the final scattering probability. So, from the derivation it has already been considered that these terms are physical in some way, corresponding to some phononic mode or perhaps a multiple phonon process. This assertion is what is used to justify using individual times for each of the terms in the sinusoidal scattering probability expansion. It is reasonable to expect that different phononic processes, perhaps involving different numbers of phonons, should have different characteristic times associated with them. Even without this change to the derivation, the resistivity curve is still in relatively good agreement with the sinusoidal expansion. These curves were not shown, but the results were quite similar to what is discussed here.

The Gaussian Scattering Probability

From the fit of Equation 4.29 to the resistivity between 150 and 245 K, shown in Figure 4.12, two important parameters, α and ω_0 are obtained. These parameters are listed in Table 4.2.

The parameter α can be used to give an approximate lifetime for the JT distortions by computing $\frac{1}{\sqrt{\alpha}}$. The value of α recovered from the fits gives a lifetime for the JT distortions of 0.14 ps, implying that these distortions are in fact not very long lived. This motivates an interpretation that there are so many phonons in the lattice at these temperatures that it is likely that when a phonon mode finishes trapping an electron at one site a new phonon is

ready to take its place. An admissible interpretation is that polarons reduce the energy of the conduction electrons momentarily, but do not trap them so strongly that they do not have any mobility at all in the lattice.

Best fit lines based on this curve admit a large positive value for ω_0 , giving an energy splitting of 5.0×10^{-3} eV. Again, this is a small energy. The fact that ω_0 is positive suggests that the polaronic state is actually higher in energy than the double exchange state, implying that the polaronic state is actually an excitation of the lattice as a function of temperature and JT distorted sites will only have a small population in the ground state.

For the gaussian scattering probability at the onset of the metal-insulator transition, the curve does not perform overly well. This is likely due simply to the fact that other scattering mechanisms giving rise to the metallic-type of resistivity behavior as a function of temperature have been omitted. If a component that is linear in temperature, a metallic resistivity component, is added to this curve it performs better in terms of fitting.

4.3.2 The High Temperature Fit to the Resistivity

Only the gaussian scattering probability predicts the maximization of the resistivity curve and the subsequent thermally activated behavior displayed by the resistivity. Only one fit to the high temperature data was made, based on the dependence given by Equation 4.29. This fit is shown in Figure 4.13. Again, the important parameters obtained are α and ω_0 . These quantities are listed in Table 4.3.

Across the peak of the resistivity, the value of ω_0 obtained is negative, meaning that the E_b energy level is lower than the E_a energy level. If the E_b level is negative, then that would make the scattering state the favorable state in this temperature range. The energy level splitting given by ω_0 is

-3.6×10^{-4} eV. This is again very small, but it is perhaps more obvious now that trapping of charge by JT distortions is occurring.

Again, the approximate lifetime of the JT distortions is given by $\frac{1}{\sqrt{\alpha}}$. The α value predicts a trapping lifetime of 1.8 ps, meaning that the trapping lifetime has increased by about an order of magnitude when compared to the low temperature result.

At very high temperatures, above the resistivity peak temperature, the resistivity appears thermally activated [68]. Something very important that has come out of this analysis is that no additional mechanism need be employed to explain the semiconductor-like behavior of the resistivity at high temperatures. This thermally-activated resistive behavior seems to have fallen out of this simplified approach. No additional mechanism need be employed such as band-squeezing [18], to explain the movement of the Fermi energy into a gap between bands. While a very interesting effect, band-squeezing or other Fermi level shift theories often predict shift values that are quite small, and unlikely to be responsible for this thermally activated behavior of the resistivity above the resistivity peak.

One more important thing to note is that this derivation gets T_c entirely incorrect. It predicts a transition temperature that is at best 50 to 100K. This is not at all near the known T_c for LCMO. More sophisticated calculations also have difficulty predicting T_c , so perhaps it should not be surprising that this simple derivation does not correctly account for this property. One way to improve the fit at high temperatures would be to take more terms in the expansion. The fit does converge at higher numbers of terms as the temperature is increased. However, since this calculation is based on a perturbative approach, it is debatable whether or not taking a large number of terms would really be meaningful.

4.3.3 Other Means of Addressing the Resistivity in CMR Compounds

Numerical simulations that attempt to predict T_c and the resistivity of CMR manganites have been attempted. Most often, tools like Monte Carlo simulations, Fermi Liquid and/or Dynamical Mean-Field theory are employed in this area [45, 46, 12]. These fits are often able to simulate a CMR-like resistivity peak quite well. A reduction in the peak height as a function of applied magnetic field can also be recovered from these numerical simulations. Currently, it still does not seem possible to accurately predict T_c by these methods. In addition, it is somewhat cumbersome to compare these simulations against experimental data.

However, semi-analytical fits to the resistivity have been attempted as well [68, 40, 75].

When fitting the low temperature dependence analytically, typically an empirical model based on specific heat arguments is employed. This fit looks like an assortment of powers of T . The largest exponent in this fit is $T^{9/2}$. This dependence does not match the resistivity data well into the transition, simply because it does not rise fast enough. The low temperature dependence of the resistivity given by the scattering probability derived based on the sinusoidal perturbation (Equation 4.21 and Figure 4.5) shows different powers of T than those typically used to compare against the resistivity from specific heat arguments [40]. These higher powers of temperature admit fits to the resistivity data that are better than those obtained from specific heat arguments.

Some analytical fits to the high temperature resistivity of CMR materials rely on empirical models based on the exponential decay of semiconductors. These fits fail to show the maximum in the resistivity near T_c and increase

exponentially as $T \rightarrow 0$.

Recently, the high temperature resistivity of LCMO with a doping level of $x=0.3$ on LAO substrates has been fit semi-analytically by a function based on polaron conductivity [68]. Despite the fact that the data presented has a T_c that does not appear optimal, the fits perform quite well near the transition and above, showing thermally activated behavior and zero resistivity as $T \rightarrow 0$. The drawback to these fits is that they rely on a Green's function, the form of which is left unspecified. This kind of fit, while perhaps more mathematically rigorous, does not provide a cohesive physical picture of what is happening in CMR materials as a function of temperature.

The Magnetization and AMR in the Transition

Three aspects of LCMO will be addressed in this chapter. Results will be presented for the magnetization of the material, the anisotropic magnetoresistance (AMR) and the effect of film oxygen content. While occasionally other quantities will be shown, what is desired in this chapter is to demonstrate a correlation between the behavior of the magnetic anisotropy (MA) and the AMR in LCMO across the transition region. It is the comparison between the anisotropy in the magnetization and the magnetoresistance that should be emphasized.

5.1 Magnetization

In this section, the experimental data, some curve fitting and a discussion of the magnetization based on a mean field model is presented. The aspects of the mean field model required here are described in section 2.3. A possible cause of the magnetic anisotropy in the transition is presented.

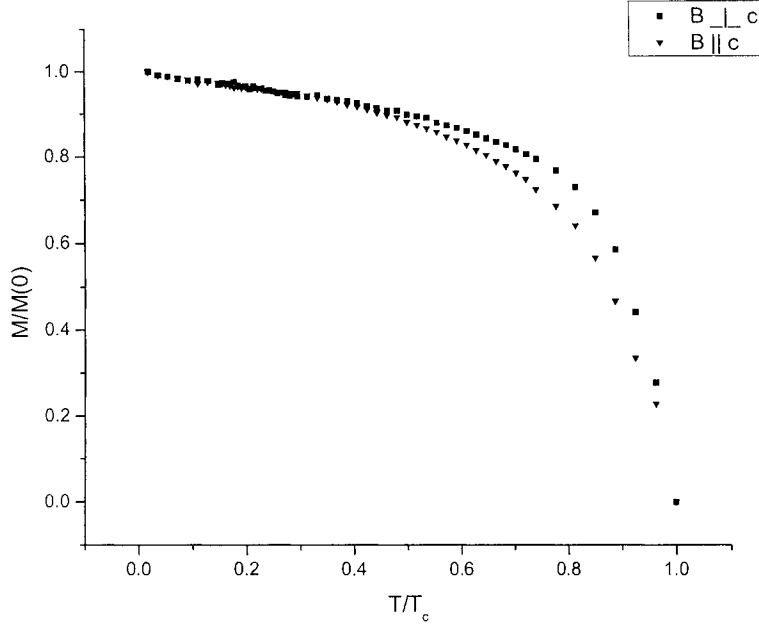


Figure 5.1: LCMO Thin Film Magnetization in the $B \perp c$ and the $B \parallel c$ Orientations. The applied field had a magnitude of 25 Gauss. The data are taken from sample CO4.

5.1.1 Experimental Results

The magnetization (M) of the thin film LCMO samples were measured by SQUID Magnetometry. The curves in Figure 5.1 show the expected dependence on temperature.

It can be seen from Figure 5.1 that there is a split between these two curves in the two orientations $B \perp c$ and $B \parallel c$ over $\frac{T}{T_c}$ fractions corresponding to the transition. At these low fields, it can be seen that in the $B \perp c$ direction, the magnetization retains a higher value through the transition, while in the $B \parallel c$ direction the magnetization has a lower value in the transition.

5.1.2 The Maximum in the Magnetic Anisotropy in the Transition

The MA discussed here is that between the $B\parallel c$ and $B\perp c$ orientations, seen in Figure 5.1.

Due to the presence of JT distorted sites in the lattice during the MIT, there may exist a preference for alignment of spins in the a-b plane on JT distorted Mn^{+3} sites, and preference for alignment along the c-axis on Mn^{+4} sites. This preference would be due to increased coupling in the a-b plane due to the compressive strain on the JT distorted sites decreasing the local in-plane Mn-O bond length. Increased coupling to the c-axis would occur on sites with an unoccupied e_g orbital due to tensile strain from the surrounding JT distorted sites increasing the local Mn-O bond length. This idea is shown schematically in Figure 5.2. That the preferred spin orientation should be in the a-b plane in these materials is given in References [74]. The idea is discussed further in section 5.2.2.

If this is a correct picture then the maximum MA at low applied fields should be a function of the doping level, x , since it carries information about the number of sites with an occupied e_g level. Other relevant parameters to describe this situation, for measurements of the magnetization at low fields, would be the magnetization at a given field and zero temperature, $M_{0,H}$, the saturation magnetization, M_s , and the spin per site, S_i . For a large number of electrons, the maximum MA for this situation would be given approximately by

$$MA_{max} \equiv \left(\frac{M_{\perp}}{M_{0,\perp}} - \frac{M_{\parallel}}{M_{0,\parallel}} \right)_{max} \approx \frac{M_{0,H}}{M_s} \left(\frac{(1-x)S_{Mn^{3+}} - xS_{Mn^{3+}}}{(1-x)S_{Mn^{4+}} + xS_{Mn^{4+}}} \right) \quad (5.1)$$

where $M_{(\perp,\parallel)}$ is the magnetization perpendicular or parallel to the c-axis respectively, $M_{0,(\perp,\parallel)}$ is the magnetic field perpendicular or parallel to the

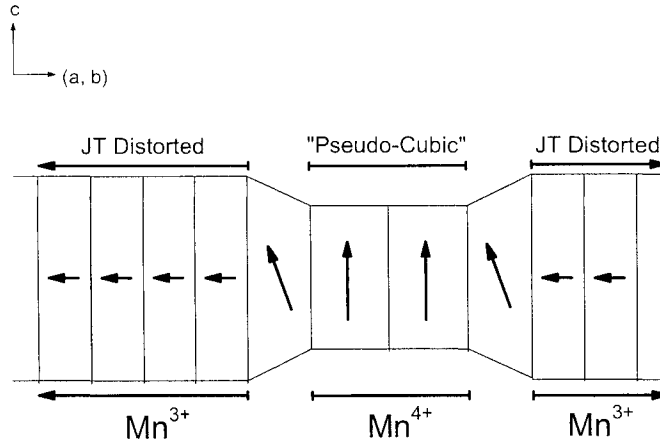


Figure 5.2: A possible configuration for the electron spins at maximum magnetic anisotropy (MA_{max}). Each of the JT distorted sites carries four electron spin moments, one from the e_g orbital and three from the t_{2g} orbitals, while the “pseudo-cubic” sites have only the three t_{2g} spins to contribute.

c-axis at zero temperature, $S_{Mn^{3+}}$ accounts for four electron spins and $S_{Mn^{4+}}$ accounts for three electron spins. The $\frac{M_{0,H}}{M_s}$ term roughly accounts for spins that remain randomized in the small field due to a domain-type structures or thermal excitations.

This picture, shown in Figure 5.2 and Equation 5.1, is likely only applicable at very low fields. At higher fields, this small magnetic anisotropy is overcome by the preference for spin alignment with the field.

5.1.3 Magnetization Analysis

Magnetic Anisotropy in the Transition

If the two curves shown in Figure 5.1 are subtracted from one another, the peak shown in Figure 5.3 is obtained.

It can be seen that the normalized magnetic anisotropy peak (MA_{max}) at $0.91T_c$ (≈ 245 K) shown in Figure 5.3 corresponds to about 0.12 at its

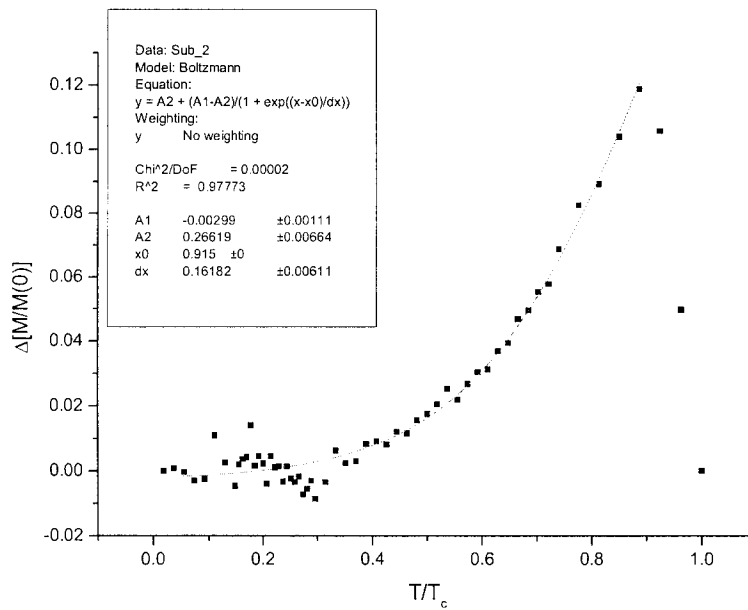


Figure 5.3: Subtracted magnetization curves for the $B_{\perp c}$ and $B_{\parallel c}$ orientations. The peak temperature of this curve compares very well with the temperature of the peak in the AMR data. The peak of this curve is at 245 K and the magnitude of the peak is 0.12. The fit shows that the growth of the magnetic anisotropy can be fit by a Fermi function. The data are from CO4.

maximum. This is well described by Equation 5.1, which predicts a peak height of 0.127. Since for the different spin orientations the $M_{0,H}$ term varies by just under a factor of two, the average of these two values was used. This is likely a correct procedure since normalizing the magnetization at low temperatures for comparison amounts to averaging the low temperature magnetization for both cases.

The Magnetization Compared Against a Mean Field Model

The dependence of the magnetization on temperature near a magnetic phase transition is most easily compared with a mean field model in two regimes, where $\frac{T}{T_c} \sim 1$ and where $\frac{T}{T_c} \ll 1$. Results for temperatures near the transition are presented first.

Near the transition the magnetization drops rapidly to zero, as shown in Figure 2.7. This drop is described by Equation 2.7. The fit to the curve shows a critical exponent of 0.53 ± 0.04 for the B||c orientation. This lies within error of the value predicted by mean-field theory. There was some discrepancy for Figure 5.5, where the exponent is greater than the mean-field result of $\frac{1}{2}$. The critical exponent in this case was 0.62 ± 0.03 .

Also, Figure 5.4 shows a fit to the data was performed for $T \rightarrow 0$. The data is somewhat insensitive to small changes at this low temperature and field, but it is sufficient to see that there is qualitative agreement with Equation 2.8, given by mean field theory.

5.1.4 Discussion of Magnetization Results

Perhaps in contrast to what might have been expected, the low field SQUID magnetometry measurements and the magnetic anisotropy suggest that some degree of magnetic order is established during the magnetic phase transition. This order is not exactly of a ferromagnetic kind, but does in fact have

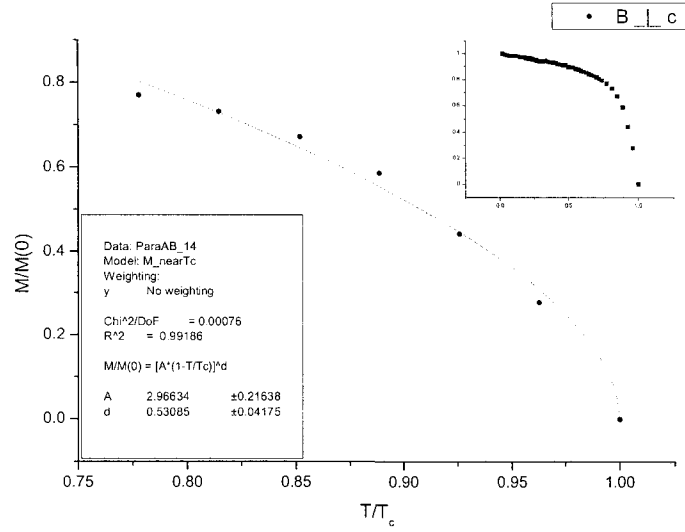


Figure 5.4: LCMO magnetization near T_c with mean-field approximation fit. The insert shows the full curve. The data was acquired using SQUID magnetometry with a field of 25 Gauss applied in the $B_{\perp c}$ direction. The data are from CO4.

Table 5.1: Summary of Coefficients from a Comparison of the Magnetization Data against a Mean Field Model for the $B_{\parallel c}$ and the $B_{\perp c}$ Orientations. The d_i parameters are the critical exponents near the transition, and the B and C parameters are constants for the low-temperature dependence.

Parameter Name	Value
d_{\parallel}	0.53 ± 0.04
d_{\perp}	0.62 ± 0.03
B	0.11 ± 0.01
C	0.22 ± 0.02
MA_{max}	~ 0.12

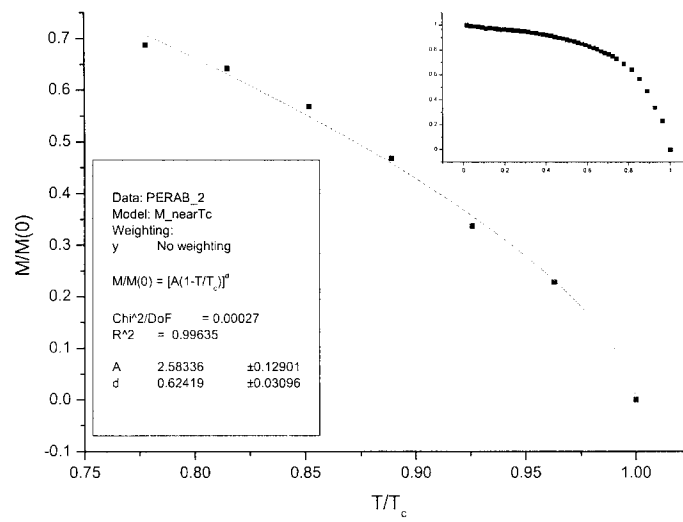


Figure 5.5: LCMO magnetization near T_c with mean-field approximation fit. The insert shows the full curve. Again SQUID magnetometry with a field of 25 Gauss applied in the $B\parallel c$ direction measured the film magnetization. The data are from CO4.

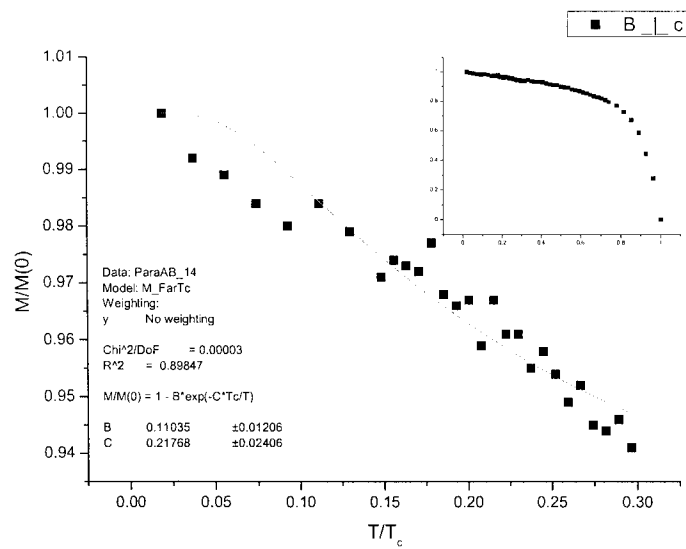


Figure 5.6: LCMO magnetization for B.Lc at low temperatures compared with a mean field theory prediction. The applied field was 25 Gauss. The data are from CO4.

directions of preferred alignment relative to the lattice planes. This preferred arrangement is shown in Figure 5.2 and the explanation of this mechanism can be found in section 5.1.2.

The calculation of the maximum magnetic anisotropy obtained under small fields, 25 Gauss, reveal quite good agreement with the anisotropy expected. However, in Equation 5.1 the $M_{0,H}$ term used was the average of the magnetizations for the two different orientations, B||c and B⊥c, at zero temperature and 25 Gauss. This average is intrinsic to the comparison, as comparing the normalized curves essentially amounts to setting both their magnetizations equal at low temperatures. It makes sense then that their average value would be the relevant factor when referring to the non-normalized magnetization at low temperatures. The value of the MA_{max} obtained from experiment is 0.12 and the value calculated from Equation 5.1 is 0.127. This shows that, under small applied fields, the preferred magnetic orientation in the LCMO thin films is likely that shown in Figure 5.2.

In terms of the magnetization, comparison against a mean-field approach has been applied with some success. The critical exponent for the B||c orientation, 0.53 ± 0.04 is within error of the mean field result of 0.5. The critical exponent in the B⊥c direction however is larger than the expected mean field result, the exponent being 0.62 ± 0.03 , implying that some extra magnetization is coming into play. This preference for magnetization in the a-b plane has already been discussed.

The parameters B and C from the mean field fit near T=0 (Equation 2.8) should both correspond to two in the mean-field model. These parameters are 0.11 ± 0.01 and 0.22 ± 0.02 respectively, certainly not within error of the value two. This discrepancy is true both for the B||c and B⊥c orientations.

The SQUID measurements are, on their own, quite revealing in terms

of the magnetocrystalline anisotropy [7] present in LCMO during the transition. It would seem that they would suggest that there is a maximum anisotropy in the plane close to T_c , after which, there is a sharp drop in the net magnetization of the material. This implies that, when enough polarons are present in the lattice, a more random spin orientation becomes the preferred state. Since paramagnetism is typically attributed to thermal fluctuations randomizing spin orientation, even in a strong magnetic field, it makes sense that at some critical number of phonons, or for a critical population of some spin-randomizing phonon mode, the CMR material should become paramagnetic.

For a somewhat more radical interpretation of what might happen to the charge and spin order at the phase transition, please see Appendix E.

5.2 Anisotropic Magnetoresistance

In this section, the results of measurements of the AMR in the transition are presented. An empirical model for the AMR in the transition is offered. Fits based on the model are performed. A discussion of the AMR results is presented. Again, emphasis is meant to be placed on the correlations between the magnetic and magnetoresistive anisotropies.

5.2.1 AMR Experimental Results

The resistivity as a function of the angle of an applied magnetic field shows a peak. The maximum resistivity is for B applied parallel to the c -axis, while the minimum is found when B is applied in the plane of the film. With this information and using Equation 2.9 the AMR can be calculated. This peak and the associated angles, measured relative to the c -axis, are shown in Figure 5.7.

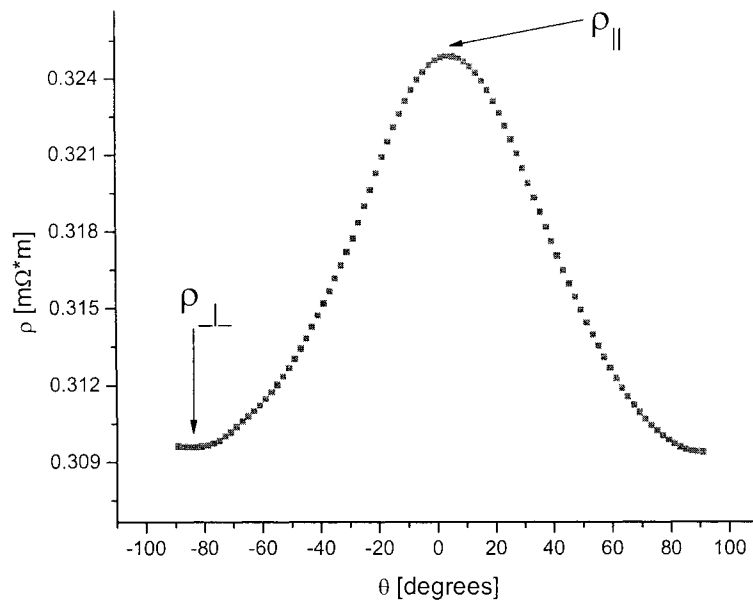


Figure 5.7: The angular dependence of the magnetoresistance of a c-axis oriented LCMO thin film. The angle of the applied magnetic field is measured from the normal to the film, which is the c-axis direction. The maximum resistivity is seen in the $B \parallel c$ orientation, while the minimum corresponds to the $B \perp c$ orientation. The data is from sample CO4.

Two phenomenon are seen in the AMR that are worth noting. They are the saturation of the AMR as a function of magnetic field and the temperature dependence of the AMR.

AMR Saturation

The AMR saturates as a function of a magnetic field as shown in Figures 5.8 and 5.9. There are two unique features to this saturation. The saturation tends to peak and then diminish as a kind of an exponential decay and the saturation point moves.

There are two possible orientations in which to measure the AMR as a function of magnetic field, in the $B\parallel J$ and the $B\perp J$ orientations. If the current is assumed to run in the x-direction, this amounts to measuring the AMR in the z-y and the z-x planes. Measurements in both directions were taken and the curves appear quite similar. The $B\parallel J$ orientation is shown in Figure 5.8 while the $B\perp J$ orientation is shown in Figure 5.9.

Temperature Dependence of the AMR

The AMR through the MIT has a peak as a function of temperature, as shown in Figure 5.10 for film CO3 and Figure 5.11 for sample CO4. This peak occurs at close to 247 K for an applied magnetic field of 0.68 T. This magnitude of applied magnetic field is sufficient to saturate the sample. Right away a correlation between the peak location in the AMR and the peak location of the MA, shown in Figure 5.3, can be seen. The peak in the subtracted magnetization occurs at roughly 245 K.

The AMR as a function of temperature has also been investigated for smaller, non-saturating applied fields. This yields some interesting results, it seems that there might be a slight shift in the peak to higher temperatures, and the AMR drops to zero at lower temperatures than it did for the larger

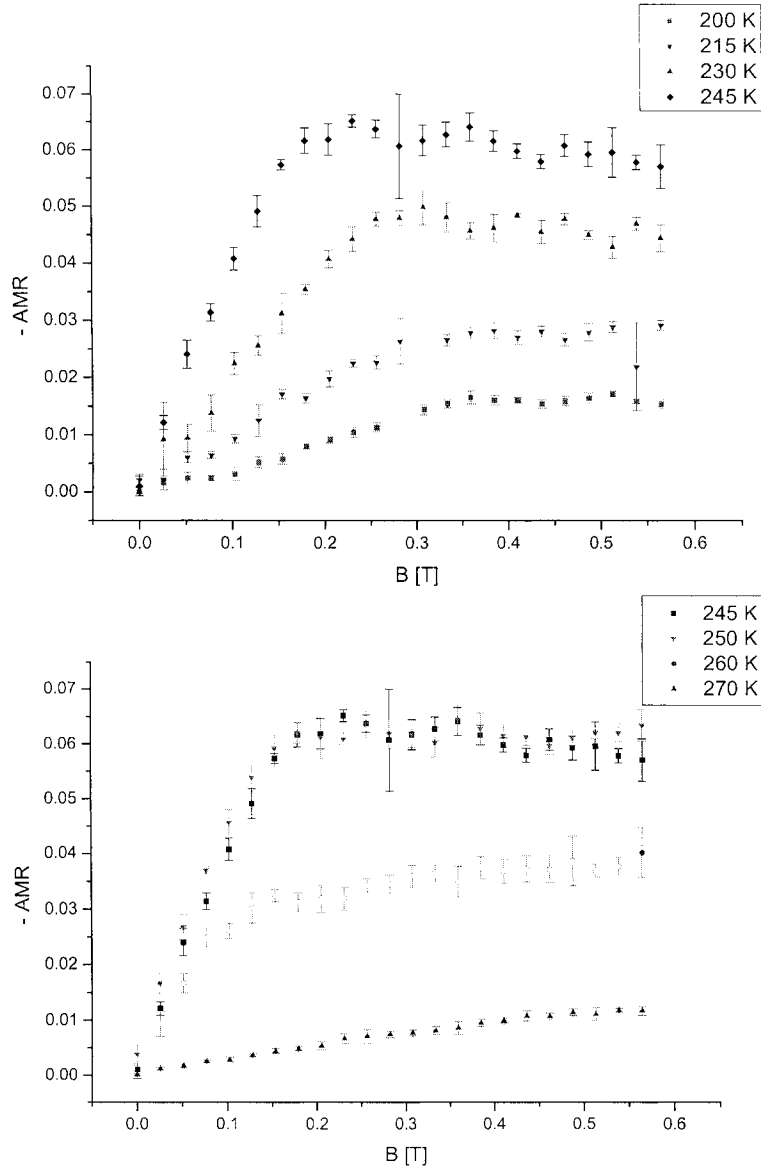


Figure 5.8: Magnetoresistive anisotropy saturation for sample CO4. Below T_c , the saturation has a higher value, but the saturating field decreases as the temperature increases. Also, the slope of the saturated part of the curve is positive for high and low temperatures, but near the anisotropy peak the saturated slope is slightly negative. The data is for the $B||J$ orientation. The instabilities in these curves are due mainly to temperature and magnetic field fluctuations.

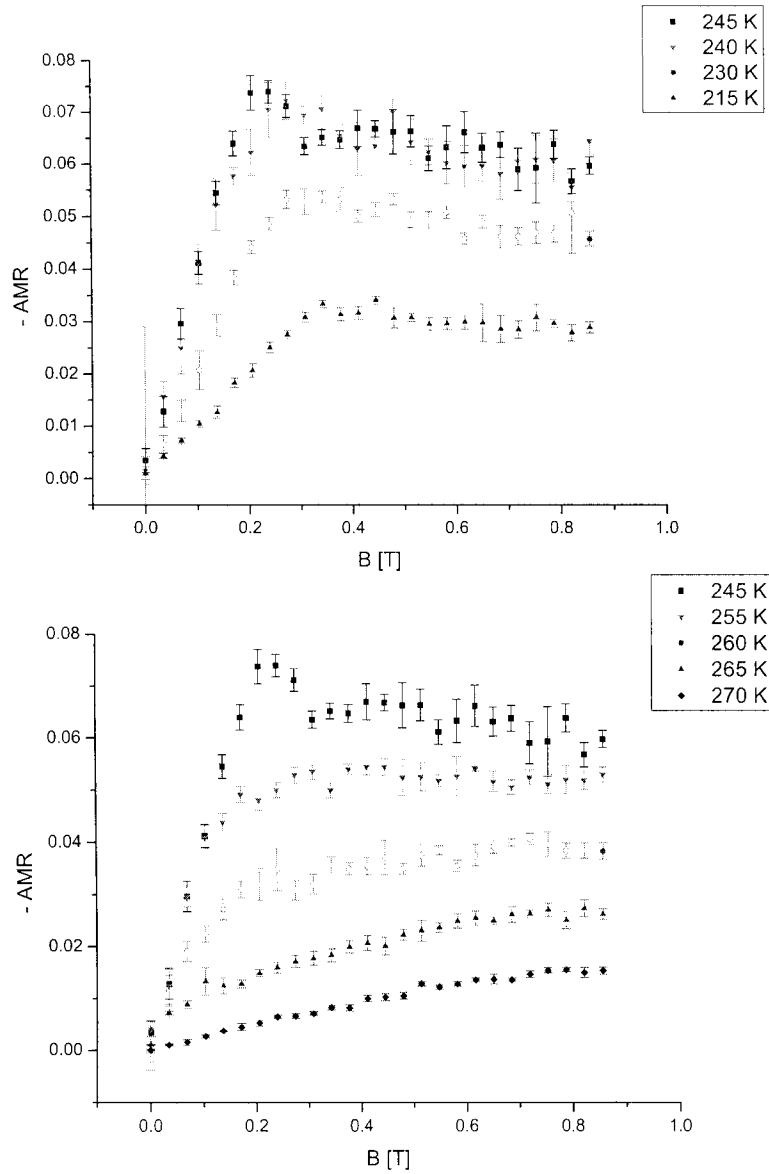


Figure 5.9: Magnetoresistive anisotropy saturation for sample CO4. Below T_c , the saturation has a higher value, but the saturating field decreases as the temperature increases. Also, the slope of the saturated part of the curve is positive for high and low temperatures, but near the anisotropy peak the saturated slope is slightly negative. The data is for the $B \perp J$ orientation. The instabilities in these curves are due mainly to temperature and magnetic field fluctuations.

applied field.

5.2.2 Analysis of the AMR during the Transition

The during the MIT, the AMR shows an anomalously large asymmetrical peak. Since at low temperatures well away from the transition the AMR is well described by spin-orbit coupling, there must be some additional mechanism that is causing this phenomenon. Spin orbit coupling is addressed briefly in section 2.4.

What is developed here is an empirical model for the AMR. This model will attempt to offer an explanation of the anomalously large AMR during the metal-insulator transition.

Phenomenological Model of the AMR

In the following presentation, a phenomenological model containing two important features will be motivated. The first will be a partition function arrived at via the comparison of two competing phases. The second will be that the phononic contribution to the energies of this system will be a function of T . This model may lack somewhat in terms of rigor, as empirical models often do. However, the results are sufficient to give some idea of what is happening in the material with respect to the AMR, and so are worth presenting.

First it should be observed that the AMR has an equivalent formulation in terms of conductivities as opposed to resistivities.

$$AMR = \frac{\rho_{\parallel} - \rho_{\perp}}{\rho_0} = \frac{\sigma_0}{\sigma_{\perp}\sigma_{\parallel}}(\sigma_{\perp} - \sigma_{\parallel}) \quad (5.2)$$

where $\sigma_{\parallel,\perp}$ refer to the conductivity with a field applied either parallel or perpendicular to the c -axis and σ_0 is the conductivity in zero field.

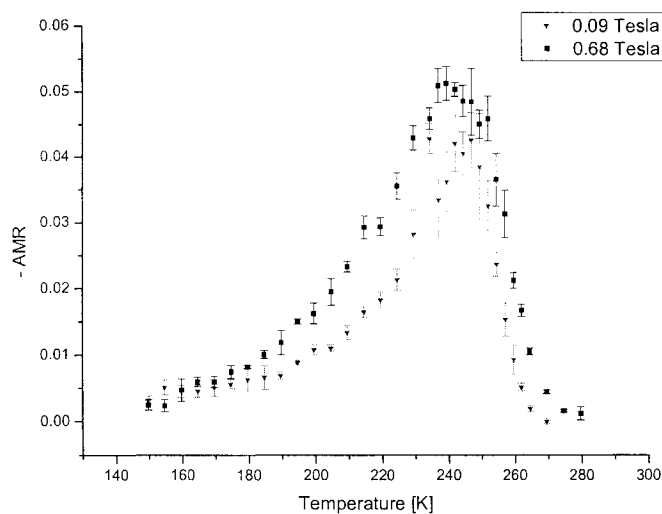


Figure 5.10: Magneto-resistive Anisotropy peak for both weak (unsaturated AMR) and strong (saturated AMR) applied magnetic fields. The instabilities are due mainly to temperature fluctuations of the LCMO thin film. This data was taken from sample CO3.

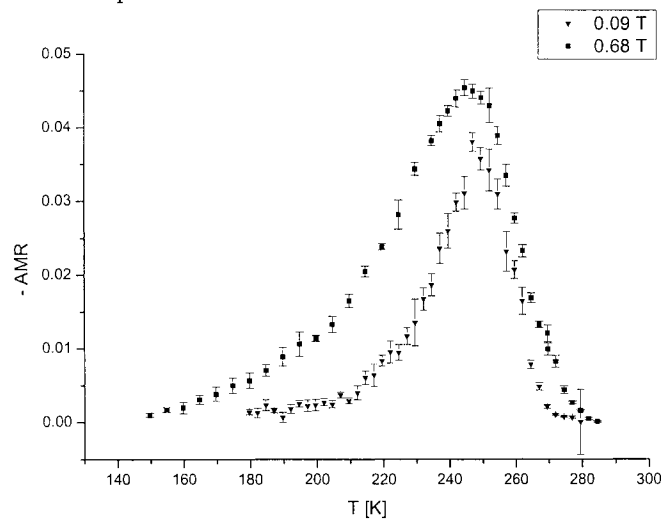


Figure 5.11: Magneto-resistive Anisotropy peak for both weak (unsaturated AMR) and strong (saturated AMR) applied magnetic fields. The instabilities are due mainly to temperature fluctuations of the LCMO thin film. This data was taken from sample CO4.

This small reformulation amounts to a difference in normalization on the difference between the perpendicular and parallel transport quantities as well as a change in the overall sign of the AMR. Since during this project the negative AMR is always plotted, it is essentially the AMR in terms of the conductivities that is being considered.

In the Drude model, the conductivity σ is defined in terms of the charge on the electron q , the mean free path δ , mass of the electron m , the Fermi velocity v_F and the electron density, n .

$$\sigma = \frac{\delta q^2}{mv_F} n \quad (5.3)$$

As a first approximation, consider that there are two interpenetrating phases that exist in these materials over the typical temperature ranges of interest, a ferromagnetic conductive phase and a paramagnetic insulating phase. The conduction mechanisms in these two phases are different. One is predominantly metallic, the double exchange mechanism, and one is more resistive, the polaronic conduction mechanism. Consider that for these two phases the density of conduction electrons propagating in these modes grow and diminish following Fermi statistics [34]. If this is the case, then in the transition, there exist electrons that are conducting by both methods.

$$\begin{aligned} \langle n_i(T, B) \rangle &= \frac{1}{1 + e^{E_i(T, B)}} \\ &= \frac{1}{1 + e^{P_i(B, T, T_c) + \beta[\varepsilon(p, q) + B]}} \end{aligned} \quad (5.4)$$

where $E_i(T, B)$ is the energy of the conduction electron. In this formulation, P_i is a term that accounts for the polaronic contribution to the energies and can be expected to have an explicit temperature dependence. This temperature dependence is accounted for in section 4.2.1 addressing polaronic

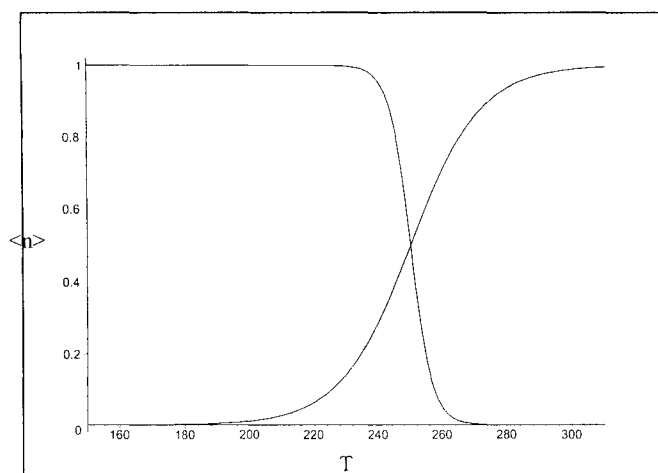


Figure 5.12: A schematic representation of the possible electron densities for double exchange and polaronic conduction showing the overlap of the two conduction mechanisms. The electron densities are given by Fermi functions. At low temperatures, the density of electrons is all of a double exchange type, while at high temperatures the electron density is entirely polaronic. In the transition region the two conduction mechanisms coexist.

conduction. Here ε accounts for other more traditional energies that these interpenetrating phases might have, such as kinetic and potential energy. What is being suggested here is that the only marked difference between the two phases is the parameter P_i , the polaronic activity that exists in each phase.

Polaronic conduction involves a Jahn-Teller type distortion of the kind shown in Figure 2.6. In the first mode, corresponding to the $3z^2 - r^2$ orbital causes an extension in the c-axis, and a contraction in the a and b lattice constants. This means that, in the case of polaronic conduction, the magnetic coupling between the Mn ions in the a-b plane increases, and the c-axis spins become increasingly decoupled. This can be seen intuitively, since the magnetic coupling should fall off as a function of r, or one could consider the

anisotropic Heisenberg ferromagnet.

$$H = -J_{x,y} \sum_{\langle ij \rangle, x,y} S_i \cdot S_j - J_z \sum_{\langle ij \rangle, z} S_i \cdot S_j \quad (5.5)$$

where $J_{x,y,z}$ is the exchange energy in one of the three cartesian directions and the $S_{i,j}$ are the spin vectors.

If the coupling constant $J_{x,y}$ is greater than J_z then it is easy to see that the lowest energy state will be the one where the spins are aligned in the x-y or a-b plane.

Unfortunately this is not the end of the story, there are surely more terms that belong in the Hamiltonian, for instance the double exchange energies and the strong coulomb repulsion term that is present in the Hubbard Hamiltonian. Solving that Hamiltonian is considerably more complicated.

Ferromagnetic Polarons

Recently there has been some presentations of analysis done on the polaronic phase of CMR manganites that make reference to ferromagnetic polarons. These studies indicate a few important things that may prove critical to the understanding of the anomalously large AMR that appears during the transition.

Ferromagnetic polarons are suspected to consist of two or three JT distorted LCMO unit cells. This may appeal to intuition, since the strain field surrounding one JT distorted unit cell surely has some effect on its nearest neighbors. The magnetic coupling within one polaron is expected to be strong while the magnetic coupling between polarons is likely weak. These polarons essentially look like nanoscale magnetic domains and have been shown to be possible experimentally, due to a long range strain field, by Transmission Electron Microscopy (TEM) [10], and theoretically, by simulations on the

1-D and 2-D Kondo lattice by Monte Carlo methods [29, 13] and an analysis using Hartree-Fock approximation at half filling [74]. They have been shown to have a preferred polarization that is in a-b plane. However, since the coupling between polarons is likely weak, nanostructured domains could form, with random magnetizations in the a-b plane. Small scale magnetic domains have been imaged recently by Magnetic Force Microscopy at very low temperatures and at temperatures above T_c in LSMO [32, 66] and by a magneto-optical technique in (110) oriented bulk samples of LCMO, with $x=0.22$, at a few temperatures below 150 K [26].

To a nearly-free electron moving through the material these nanoscale domains might look something like a spin-wave. If the conduction electron was an itinerant or metallic electron near the Fermi level, then this would not matter. However, if the conduction mechanism is the double exchange mechanism then the spin degree of freedom is critically important when it comes to charge transport, as shown roughly by Equation 2.3.

One way to attempt to ascertain the effects of a non-uniform magnetization on a single electron is to use the Landau Lifshitz Gilbert equation to predict the orientation of a classical magnetic dipole. Since this problem is rather complicated, a double-exchange electron with a spin degree of freedom conducting by hopping through what might be a non-uniformly magnetized background with a general preference for spin alignment in the a-b plane, as a first approximation it is perhaps not unreasonable to appeal to this theoretical tool.

The LLG equation was solved numerically for the electron spin initially aligned in the z-direction with a strong magnetic field in the same direction. Two different anisotropy terms were investigated, a constant anisotropy in the x-y plane and an oscillating magnetic field, meant to simulate the ran-

domized local magnetization of the CMR material. In both cases, for a magnetic field that had a magnitude of one percent of the saturation magnetization, the magnetic moment of the dipole would precess out of alignment with the z-axis on the order of nanoseconds.

For the constant field, the spin precessed out of alignment with the z-direction and came to some equilibrium angle. This may not contribute to additional scattering as again the magnetization would be uniform throughout the sample, just not aligned exactly with the z- or c-axis.

For the oscillating anisotropy term, the spin was seen to continually precess about the z-axis, implying that as the electron travels through the material, by double-exchange, its transition probability would be decreased at every lattice site, since the local magnetization at the next site in the lattice would be different than the currently occupied site. The same effect does not occur for spins initially aligned in the x-y plane, which do not precess at all as a function of time. This qualitatively supports the mechanism that is responsible for the AMR. For further the details of the calculations and some representative plots, please see Appendix D.

To summarize this approach as simply as possible, a reduction in charge transport may occur, by double exchange (Equation 2.3), if ferromagnetic polarons contribute to a randomization of the local magnetization. From site to site, the Mn t_{2g} orbitals may have slightly different magnetic moments, despite the influence of a strong applied magnetic field, due to the random or perhaps antiferromagnetic magnetic contributions from nearby ferromagnetic polarons. This effect is large for an applied field aligned parallel to the c-axis. It is greatly reduced for a field aligned in the a-b plane.

Again, though the LLG equation is a classical calculation, it is sufficient to model magnetizations on a small scale, and can be adapted to approxi-

mate discrete magnetic moments on a realistic atomic lattice. This classical approximation is a reasonable one given the temperatures of interest for LCMO, and it is common practice to treat the spins classically, even in the double-exchange Hamiltonian [44].

Consequences of the Coexistence of Phase Separated Ferromagnetic Polarons and Double-Exchange Electrons

If the presence of polarons causes an increase in the c-axis dimension and a resulting magnetic anisotropy that, by double exchange causes an increase in resistivity, then the limiting feature in the conduction should be the product of the two electron densities present in the transition. This product is shown in Figure 5.13.

$$AMR(T)_{T \sim T_c, B} = AMR_{T=0} + C \left(\frac{1}{1 + e^{z_1(T, B)}} \right) \left(1 - \frac{1}{1 + e^{-z_2(T, B)}} \right) \quad (5.6)$$

where the $AMR_{T=0}$ is any remnant AMR usually given by spin-orbit coupling, C represents an unknown amplitude, z_1 is the energy of the double-exchange state and z_2 is the energy of the polaronic state, each as a function of temperature, T , and magnetic field, B .

At low temperatures, below T_c , the anisotropy is limited by the number of polarons present in the lattice. At high temperatures, above T_c , the anisotropy is limited by the number of electrons transported by the double exchange mechanism, since they are the dominant charge carriers and are sensitive to the the magnetic anisotropy.

There is some freedom in choosing the z_1 and z_2 parameters dependence on temperature here. Based on the resistivity analysis performed in section 4.2.1. the $z_{1,2}$ that were selected are

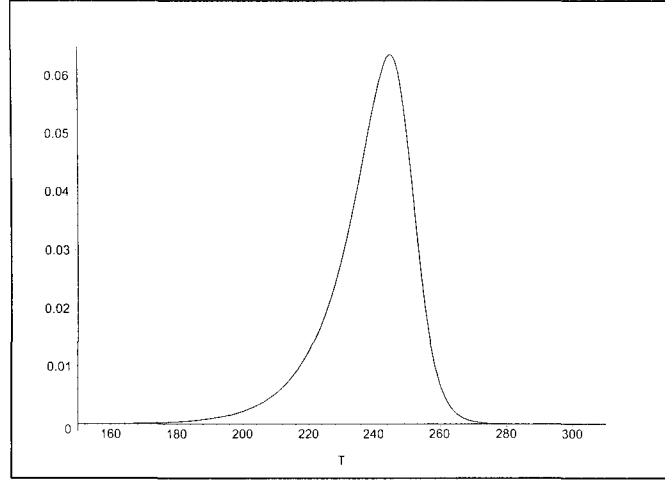


Figure 5.13: The product of the two Fermi functions describing the different conduction mechanisms. This function should compare well with the AMR as a function of T .

$$z_i = c_{i,1}(T - T_c) + \frac{c_{i,2}}{c_{i,3}^2 + (T - T_c)^2} \quad (5.7)$$

where the parameters $c_{i,j}$ are unknown coefficients and $c_{i,3}$ is a damping term introduced on physical grounds on the strong suspicion that the energy given by the increase in splitting is not actually going to become infinite at T_c .

Another option is an asymmetric double sigmoidal curve from the Origin fitting package. With a few small modifications, this exponent looks like

$$z_i = \frac{c_{i,1}(1 - \frac{T}{T_c}) + c_{i,2}\frac{T}{T_c} + H_Z}{\frac{T}{T_c}} \quad (5.8)$$

where the $c_{i,j}$ are constants and the Zeeman energy, H_Z , is equal to

$$H_Z = -\mu_B g \vec{B} \cdot \vec{S}_n \quad (5.9)$$

where μ_B is the Bohr magneton, g is the Landé g factor and S_n is the

spin magnetic moment on site “n”. Fine structure and spin orbit coupling contributions have been neglected.

Both of the z_i suggested in equations 5.7 and 5.8 fit the CMR data with equally well, the only difference is the coefficients. For all subsequent algebraic manipulations of the AMR dependences Equation 5.8 is used. This choice is essentially arbitrary.

At any given point during the transition, the total density of carriers of both types is just the sum of the carrier densities.

$$n_{Total}(B) = \frac{1}{1 + e^{z_1(T,B)}} + \frac{1}{1 + e^{-z_2(T,B)}} \quad (5.10)$$

where n is the carrier density and z_i is the energy of either the double exchange state or the polaronic state. The convention will be that z_1 corresponds to the double exchange state while z_2 refers to the polaron energy.

Since the AMR saturation curves are taken at a constant temperature and since the carrier densities are functions of magnetic field, the AMR saturation curves should be proportional to this total density.

$$AMR(B)_T = d_1 + \frac{d_2}{1 + e^{z_1(T,B)}} + \frac{d_3}{1 + e^{-z_2(T,B)}} \quad (5.11)$$

where the d_i are scaling parameters for the numerical fit.

In both of the above cases, if the two forms for the AMR are analyzed, in both cases the same denominator is obtained. If this denominator is considered to be the partition function then, employing the standard thermodynamic identity surrounding the magnetization at a constant temperature

$$M = - \left(\frac{\partial A}{\partial H} \right)_T \quad (5.12)$$

where H is the applied field and A is the Helmholtz Free Energy

$$A = -NkT \ln(Z) \quad (5.13)$$

with N being the number of particles, k is Boltzmanns constant. T is the temperature and Z is, in this case, the empirical partition function

$$Z = 1 + e^{z_1} + e^{-z_2} + e^{z_1 - z_2} \quad (5.14)$$

one can arrive at the following relationship for the two AMR formulae from Equations 5.6 and 5.11 respectively.

As a function of temperature, the relationships in Equations 5.15 and 5.16 are obtained for the AMR.

$$AMR(T)_{T \sim T_c, B} = AMR_{T \rightarrow 0} - C \left(\Gamma \mu M(T, B) + \frac{e^{z_1(T, B)}}{Z} \right) \quad (5.15)$$

$$= AMR_{T \rightarrow 0} - C \frac{e^{-z_2(T, B)}}{Z} \quad (5.16)$$

$$\text{with } \Gamma = \frac{1}{g\mu_B S_n N k T_c}$$

As a function of magnetic field, the relationship for the AMR given in Equation 5.17 is found.

$$AMR(B)_T = -\frac{T}{T_c} e^{-z_2(T, B)} \left(\Gamma \mu M(T, B) + \frac{2 \sinh(z_2(T, B))}{Z} \right) \quad (5.17)$$

$$\text{with } \Gamma = \frac{1}{g\mu_B S_n N k T_c}$$

where μ is the relative permeability, and M magnetization. Here. Equations 5.15 and 5.16 refer to the dependence of the AMR on temperature, while Equation 5.17 refers to the AMR as a function of magnetic field.

This analysis suggests that the AMR has a dependency on the magnetization of the material, which could be expected for double-exchange ferromagnets. The magnitude of the CMR effect, the “orders of magnitude” resistivity change around T_c , is too large to be a result of the double-exchange mechanism. In contrast, these relatively small anisotropy effects may well be a result of the correlation between conduction and spin in these CMR materials, since they have a magnitude of a few percent.

There are additional terms in both Equation 5.15 and 5.17 that require some explanation.

For Equation 5.15, terms like

$$P_i(T, B) = \frac{e^{z_i(T, B)}}{Z} \quad (5.18)$$

are present. These terms represent the probability of finding an electron in one of two states, either double exchange or JT polaron. The analysis here is only sufficient to write down two relationships, representing the two limiting cases at high or low temperatures. At high temperatures, Equation 5.15, the curve is limited by the probability of finding a double exchange carrier in the lattice and the magnetization, both of which are rapidly diminishing. At low temperatures, the AMR is dominated by the probability of having magnetic polarons present, giving rise to the magnetic anisotropy, as shown in Equation 5.16.

In Equation 5.17, there are a few very important features. First of all, it is important to note that it is likely that the magnetization of the sample will dominate the normalized hyperbolic sine term. Second, if z_2 is overall a negative exponent as a function of magnetic field, there will be an exponential decay of the AMR as a function of B until the quantity disappears at high field. This has important ramifications for the CMR effect. If at high fields

the AMR disappears, it implies that at high fields all the polarons responsible for the AMR are transformed back to DE carriers.

Basically, since the total number of carriers is conserved in the system, the temperature dependence of the AMR and the saturation of the AMR can be understood as exchange of carriers between and Jahn-Teller polaron conduction mechanisms, as a function of temperature or magnetic field.

So far, the adoption of the phenomenological partition function has been somewhat arbitrary. For further motivation of this as an meaningful choice of parameter, please see Appendix C.

Curve Fitting of the AMR

Curves based on the derivations above can be used to fit the AMR both as a function of magnetic field and temperature. Equation 5.11 is used for the AMR as a function of magnetic field. The curves are described quite well by this kind of dependence. The peak is reproduced along with the exponential decay after the maximum.

The results are also shown for different AMR curves at a few representative temperatures near T_c . The fits throughout the transition are shown in Figures 5.15 and 5.16.

Fits to the AMR as a function of temperature data have been performed based on Equation 5.6. These fits appear to perform quite well in the transition. That the AMR curves as a function of temperature correspond to sigmoidal curves is not in question, but it seems that fits to the curves can be made based on numerous different choices of the z_i .

5.2.3 Discussion of the Anisotropic Magnetoresistance

Due to the arbitrary selection of the forms of the exponents in Equations 5.11 and 5.6, it is not possible to make any meaningful quantitative predictions

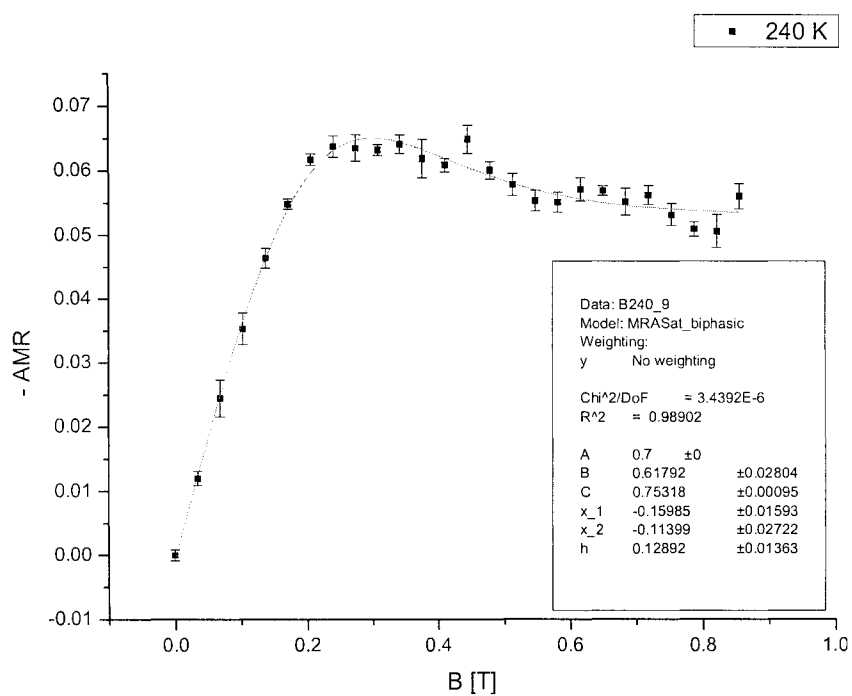


Figure 5.14: Magnetoresistive anisotropy saturation for LCMO at temperatures near T_c . The saturation occurs at about 0.17 T. Note the decay of the AMR above the saturation point. The instabilities are due mainly to temperature and magnetic field fluctuations. The data are from CO4.

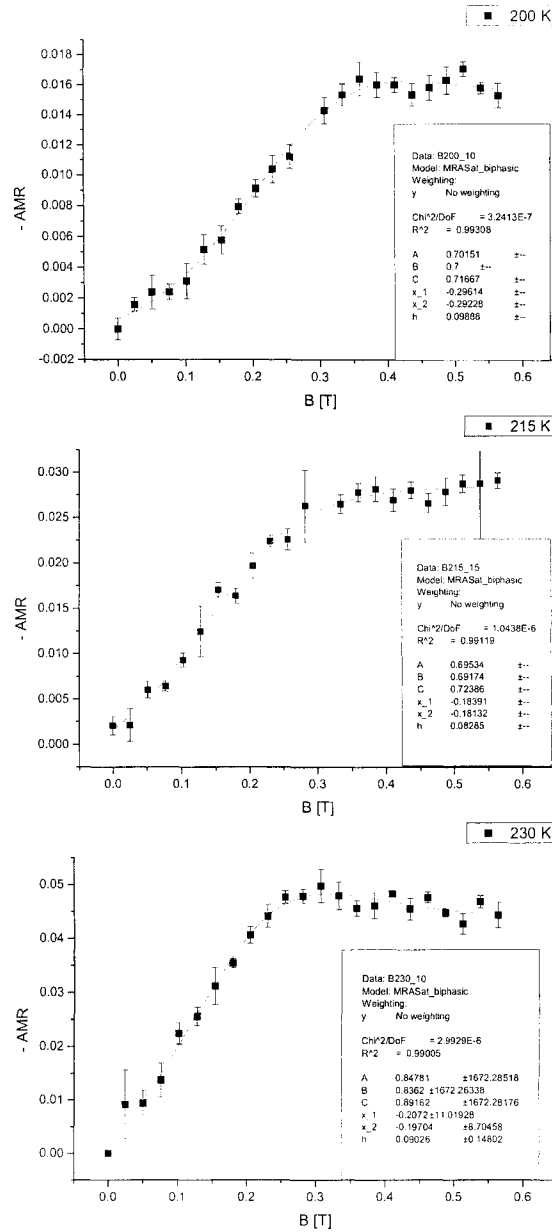


Figure 5.15: From 200 to 230 K the AMR data can be fit using the this phenomenological phase-separation model, Equation 5.11. This data is for the B||J orientation. The data are from CO4.

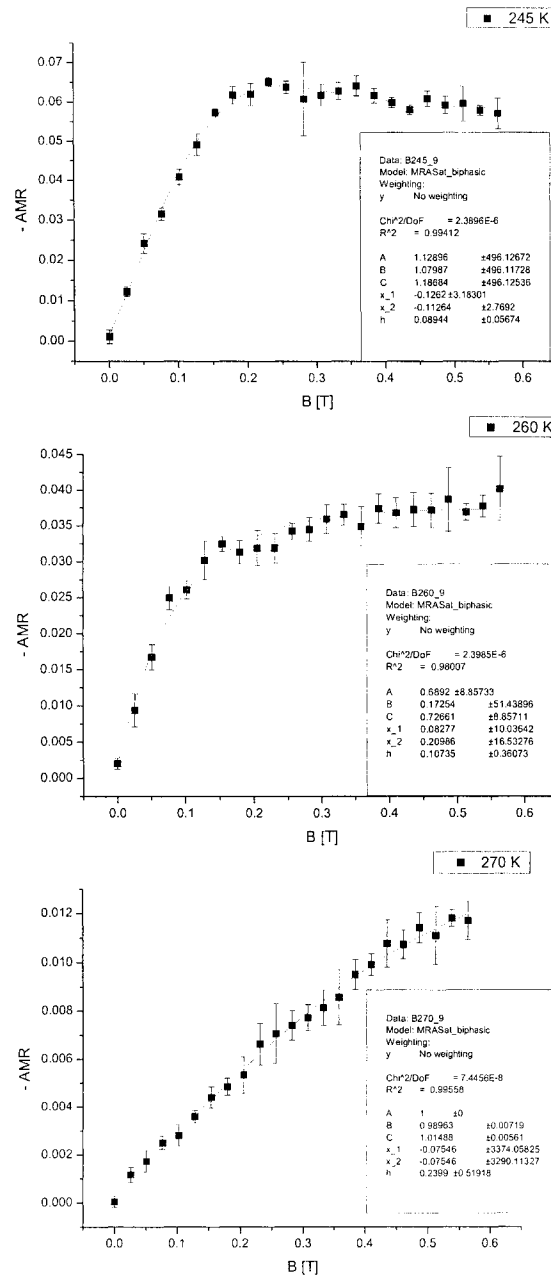


Figure 5.16: From 245 to 270 K the AMR data can be fit using the this phenomenological phase-separation model, Equation 5.11. This data is for the $B||J$ orientation. The data are from CO4.

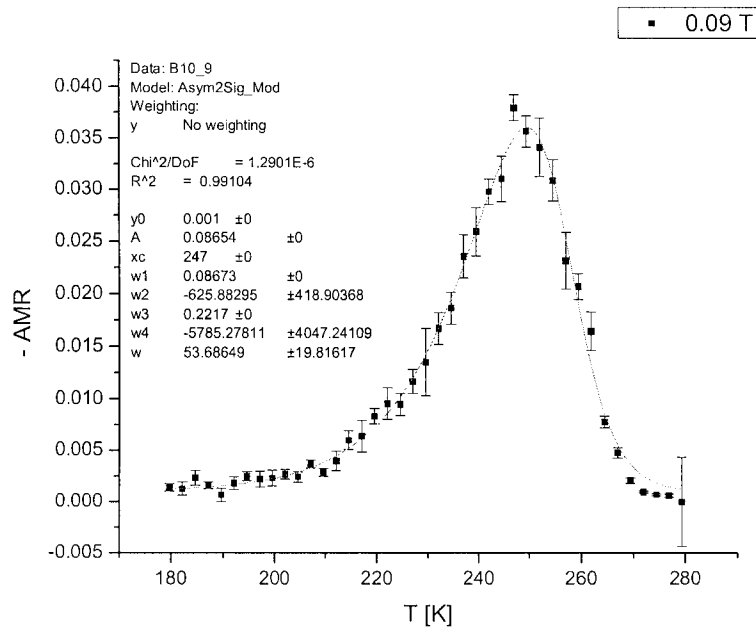


Figure 5.17: Fit to the AMR vs T data for sample CO4. The magnetic field applied is ~ 0.09 Tesla. The AMR is not saturated for this field strength. The data are from CO4.

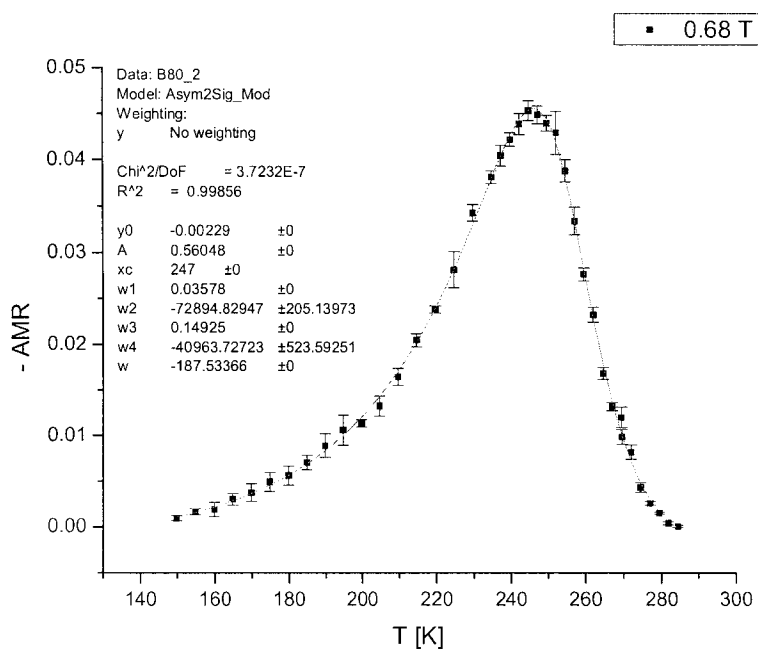


Figure 5.18: Fit to the AMR vs T data for sample CO4. The magnetic field applied is ~ 0.68 Tesla. The AMR is saturated for this field strength. The data are from CO4.

from the parameters found from fits of these equations to the data. It would have been preferable to have been able to have pulled some material parameters from a very rigorous microscopic formulation. However, that the general form of the AMR curve can be fit by this dependence, for exponents that are functions of B and T, is in itself likely very useful information. As a first attempt at an interpretation and understanding of the increased AMR at temperatures near T_c , this general dependence is perhaps satisfactory.

As a result of the inability to be quantitative on a reasonable level, a brief discussion of the AMR results is presented.

MA and AMR Peak Location Comparison

The peak of the AMR for sample CO4 and a field strength of 0.09 T, shown in Figure 5.17, is approximately 247 K. The peak in the magnetic anisotropy, shown in Figure 5.3 is at a temperature of 245 K, at a field of 25 Gauss. These two peak temperatures correspond well, which supports the idea that the magnetization and the magnetoresistance are correlated.

AMR vs. B

The saturation point of the AMR moves depending on the temperature. This may give an idea of the number of magnetic spins still available to be aligned by an external applied field. As the AMR saturation point moves to lower values, it is taking less field strength to align spins in the material. This suggests that there are less spins to be aligned. The saturation point is seen to decrease throughout the transition.

For applied B-fields larger than the saturation field and at temperatures near T_c , the AMR is observed to decay. If the phase separation interpretation is a good one, then this indicates that with a high enough field, electrons trapped by JT distortions can return to their magnetized and conductive

state.

AMR vs. T

In the case of the temperature dependent AMR, the fits given by the phase separation model are in very good agreement with the data. At the onset of the MIT, the AMR grows based on the growing number of trapped polarons in the lattice. The spin of these localized electrons couples more strongly to the other Mn-ions in the a-b plane and alignment in that plane is strongly favored. This has been attributed to an exchange effect that results in magnetic anisotropy in the lattice. The carriers that are still conducting by the double-exchange mechanism are sensitive to this magnetic anisotropy. From simulations of the Landau Lifshitz Gilbert (LLG) equation it can be seen that increased scattering could arise as a result of nanoscale magnetic domains forming in the CMR material during the transition. This is due to the local magnetization between Mn ion sites varying throughout the material on a small scale.

Additional Considerations

The interpretation given here for the AMR is that polarons contribute an additional in-plane magnetization. This has been taken to have an effect on the double exchange carriers, given that they are the most mobile carriers in the lattice. However, there are other possible mechanisms that could contribute. Consider a polaron that forms in the lattice from a double exchange electron whose spin is initially aligned in the c-axis direction by a large external field. If the polaron forms, the spin will likely align in the a-b plane. If the electron is subsequently liberated by some mechanism, the spin will still have to align with the external field before it has a significant probability of undergoing transport through the lattice. Also, the polarons themselves are

likely mobile in the lattice, though obviously not on the same scale as double exchange type carriers. If this were not the case, then the polaronic model presented in the Theory section and in Ref. [68] would be unlikely to predict the thermally activated behavior of the resistivity seen above T_c . The interaction of mobile polarons with lifetimes that are perhaps finite, particularly in the onset of the resistivity increase near T_c , and that interaction of this phase with a double-exchange phase is a complicated set of interactions to model.

Finally, it is important to note that the e_g orbital orientation and long range strain field observed in Ref. [10] and mentioned in section 5.2.2 was found in a layered LSMO material. While this material and LCMO have their differences, the observations of the AMR have been interpreted as evidence for this kind of strain field in non-layered materials.

5.3 Oxygen Depletion

In this section, results from the oxygen content experiments are presented. Again, the emphasis should be placed on the effect that oxygen content in the film has on the AMR.

5.3.1 Resistivity, MR and AMR Data after Vacuum Annealing

The effects seen in oxygen deficient thin films of LCMO are numerous. The resistivity peak increases in magnitude and the critical temperature shifts to lower temperature with decreasing oxygen content. The resistivity increases at low temperatures and in the transition. These effects are shown in Figure 5.19, along with the trend of the MR.

The MR peak decreases in magnitude and the temperature at which the

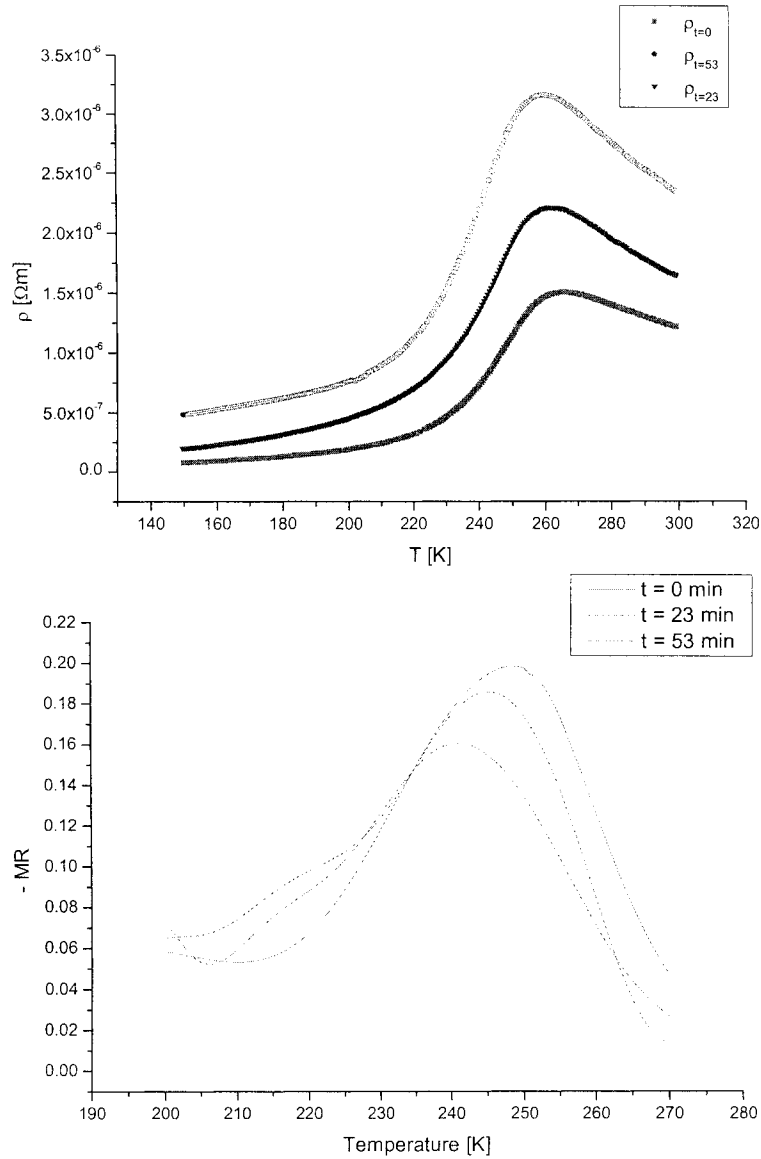


Figure 5.19: Top: The oxygen stoichiometric and non-stoichiometric resistivities for three vacuum annealing times. Bottom: The MR peaks decrease in magnitude slightly as a function of vacuum annealing. Both peaks show a shift to lower values of T_c . The data are taken from sample CO3.

MR maximizes is decreased as oxygen is removed.

The magnitude of the AMR effect increases, that is the difference between the resistivities of the $B \perp c$ and the $B \parallel c$ cases increases as oxygen is removed from the material, if all the AMR peaks are normalized to the stoichiometric ($t=0$ min) resistivity curve. If the curve is instead normalized to the non-stoichiometric resistivity, then the AMR is seen to decrease. These effects are shown in Figure 5.20.

The total shift in the MR and AMR peaks is at approximately eight Kelvin.

5.3.2 Analysis of Oxygen Content Experiments

A comparison of the peak magnitudes and positions in temperature has been performed for the vacuum annealing experiments. This is just a quantitative look at the data shown in Figure 5.20. The results of comparing peak height and location in temperature are shown in Figures 5.21 and 5.22.

5.3.3 Discussion of Film Oxygen Experiments

The results of the oxygen content experiments on LCMO thin films are most easily interpreted in terms of three effects. These effects are an increase in lattice defects, an increase in lattice strain and c-axis dimension as well as a decrease in hole doping concentration.

That the resistivity increases near T_c and at low temperatures can be understood simply from the fact that without the required amount of oxygen there are now many defects present in the lattice. Oxygen plays a crucial role in conduction by double-exchange. It is oxygen that forms the conductive bridge between Mn ions in the double exchange picture. Electrons will be forced to find a path through the material along which there are oxygen ions

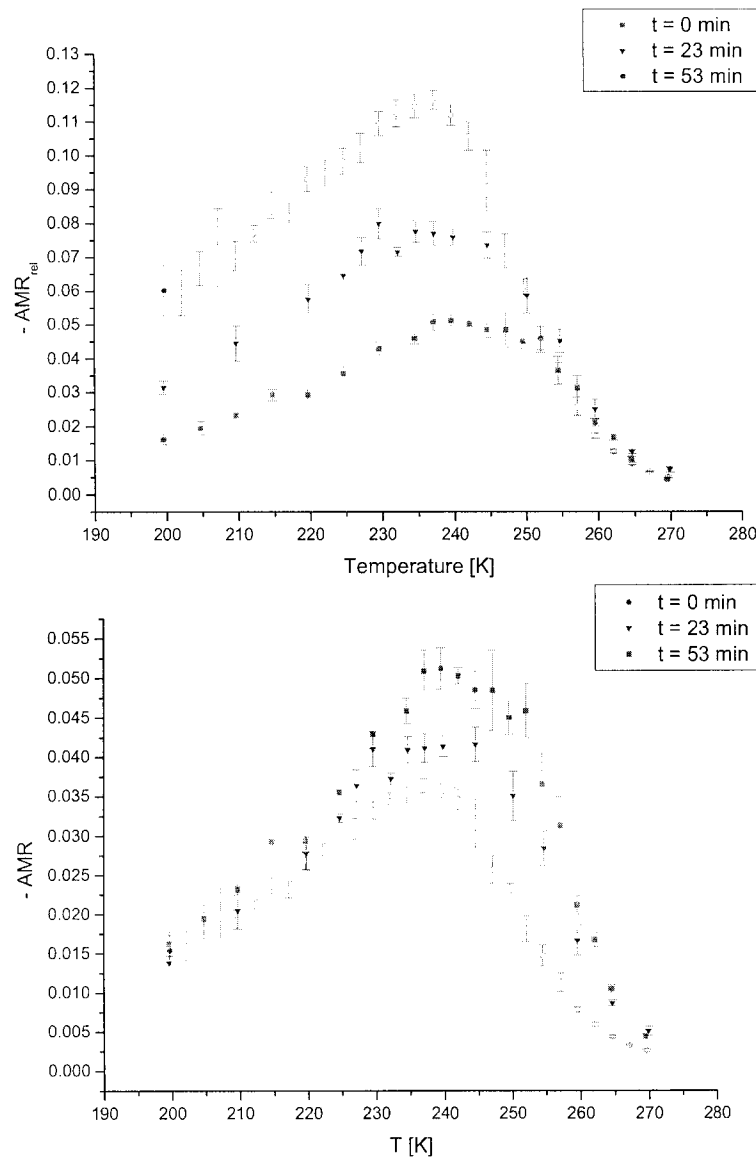


Figure 5.20: The effects of vacuum annealing on the AMR peaks. Top: The AMR_{rel} peak, normalized to the *stoichiometric* resistivity at zero field (the $t=23$ min AMR is normalized to $t=0$ min resistivity curve) grows with annealing. Bottom: The AMR peak normalized to the *non-stoichiometric* resistivity at zero field (the $t=23$ min AMR is normalized to the $t=23$ min resistivity curve) diminishes with vacuum annealing. The data are from sample CO3.

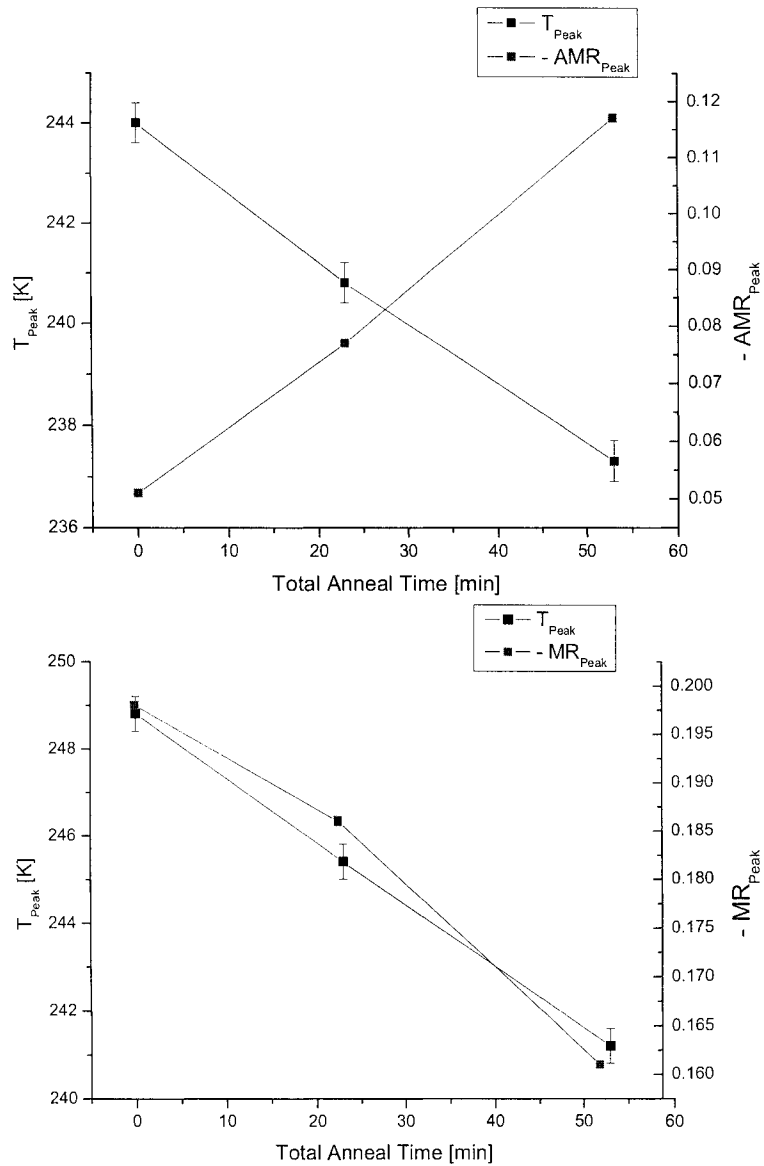


Figure 5.21: A comparison of the peak magnitude and temperature of the AMR and MR. The vacuum annealed peak magnitude and temperature for the MR and AMR peaks. The AMR is taken relative to the *stoichiometric* resistivity. The data are from CO3.

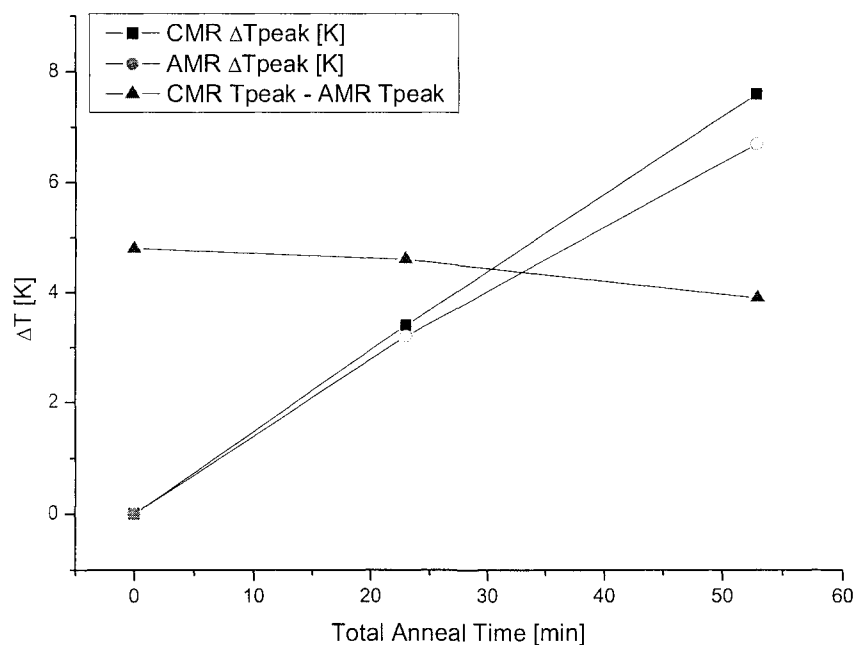


Figure 5.22: A comparison of the peak magnitude and temperature of the AMR and MR. A comparison of the temperature difference between the MR and the AMR peaks is shown. Again, the AMR is normalized to the *stoichiometric* resistivity. It can be seen that, for large annealing times, it might be possible for these peaks to overlap in temperature, as the distance between them decreases slightly by the third vacuum annealing. The data are from CO₃.

and will scatter when they encounter a lattice defect caused by a missing oxygen ion.

That the AMR increases in magnitude relative to the optimal oxygen content in the film suggests that for oxygen deficient samples there is an increase in the c -axis length. It has been shown by XRD that oxygen deficiency leads to increased stress in the crystal lattice, and that that stress generally leads to an extension in the c -axis dimension [57, 58]. This overall increase in the c -axis lattice constant again decouples the spins along the c -axis direction and increases the coupling in the a - b plane. This leads to the increased magnitude of the AMR relative to the optimal oxygen content.

That the magnitude of the AMR increases and that the AMR peak and T_c shift to lower temperatures suggests that oxygen deficiency improves the probability that self-trapped polarons will form in the material. This increase in the c -lattice parameter looks very much like a Jahn-Teller distortion. It is likely that the loss of oxygen in the film makes it easier for JT distortions to populate the lattice and trap carriers at lower temperatures. This shifts T_c to lower values.

In LCMO, it is expected that oxygen is in possession of two extra electrons, O^{-2} , due to its large electronegativity. Without the optimal level of oxygen in the lattice, the electrons that would otherwise have been bound to the oxygen sites now likely occupy Mn e_g sites, since the Fermi level lies in the Mn e_g band. This has the effect of lowering the hole doping level in the material. It is well-known that T_c depends on the hole doping level in these materials. From an optimally hole doped manganite, any change in the hole doping results in a lowering of T_c . The addition of these extra carriers would also have an effect on the AMR. The additional electrons in the lattice, if trapped by Jahn-Teller distortions, would contribute additional spin

moments that prefer to align in the a-b plane. From this as well, an increase in the AMR relative to the optimal oxygen content could be expected.

The increase in the overall resistivity is likely due solely to increased scattering by the additional defects present in the lattice due to lack of oxygen. The T_c shifts observed are likely the combined result of the increase in lattice strain and the hole doping concentration, both of which have an effect on T_c . As the oxygen content is lowered to values far away from optimal doping, the MIT becomes broader. This may be a result of competition between the two effects of lattice strain and hole doping, both of which are shifting T_c , but in opposite directions and likely not at the same rate.

Correlations between oxygen content and T_c have been shown experimentally for precise values of δ [64, 16]. These experiments were done on bulk samples but it is reasonable to expect a similar trend to be observed in thin films. This assumption is certainly borne out by this work.

The MR is reduced in magnitude for reduced oxygen content in the films. This may be due to competition between the CMR effect which appears to liberate e_g electrons and the increased lattice strain that prefers to trap them. Typically, the MR curves have to be fit in segments by high order polynomials. This adds a few fitting artefacts to the MR peak, but care has been taken so that the peak location and height remains undisturbed.

The AMR peaks shown in Figure 5.20 are normalized two ways. For the “stoichiometric” AMR peaks, the difference between the $B\parallel c$ and $B\perp c$ resistivities for different oxygen contents is normalized to the resistivity for optimal oxygen doping ($\delta = 0$). Since this quantity remains constant throughout the oxygen content investigation, this makes comparing the curves between annealing events possible. However, if the AMR is instead normalized to the zero field resistivity for the same oxygen content, the “non-stoichiometric”

case where $(\rho_{\parallel} - \rho_{\perp})_{\delta_i}$ is divided by ρ_{0,δ_i} , then the AMR decreases as a function of annealing time. This suggests that, while the strain of oxygen reduction does tend to increase the c-axis length, the increased scattering due to defects outpaces the increase in the quantity $(\rho_{\parallel} - \rho_{\perp})$.

Conclusions

An investigation into the CMR compound LCMO has been undertaken. Some qualitative insight into the central problem, that of the marked increase in the resistivity near T_c has been obtained. In the analysis presented, it has been suggested that the energies of the Jahn-Teller polaronic scattering mechanism are a direct function of temperature. At temperatures near T_c , these temperatures are of a magnitude such that they can compete for the dominant ground state energies present in the lattice. Scattering probabilities derived from Jahn-Teller considerations fit the resistivity of LCMO with reasonable accuracy over small temperature ranges.

A detailed look at the AMR as a function of temperature and magnetic field have also been presented. The explanation given for the phenomenon is that of two distinctly different charge carrier densities co-exist in the transition. This interpretation has yielded some results surrounding the dependence of the AMR as a function of temperature and magnetic field. The idea that the AMR is a double-exchange effect has been suggested. This is based on the ability to show that the AMR has a dependence on the magnetization of the material.

The effects of oxygen stoichiometry have been presented. An explanation of the resistivity, AMR and MR peaks as a function of vacuum annealing time has been presented. The effects of reduced oxygen content on these quantities has been discussed in terms of increased lattice defects, increased lattice strain and decreased hole doping level.

In parting, some observations from the data that may be of assistance in understanding the CMR effect are offered.

The CMR Effect as Charge Transport across a 90° Magnetic Domain Wall

In the fully phase separated regime, where all e_g electrons are JT distorted, as shown in Figure 5.2, in order to find an empty e_g orbital to hop to, the electron would have to traverse something like a 90° domain wall. If the double exchange mechanism still has some relevance to polaron conduction, then the probability of hopping through a domain wall that is 90° is zero, from Equation 2.3. Thermal fluctuations may increase this hopping probability simply by randomizing spins, but still a larger resistance could be expected from this arrangement. Also, the details of the actual spin dynamics across any magnetic domain wall are largely unknown, so this may also help to increase the hopping probability from zero to some large but finite amount. This mechanism may contribute to the increase in resistivity near T_c . It would also require the double-exchange mechanism, which has been left aside in many attempts to understand the resistivity of these materials in the transition, including the derivations in this report.

The Colossal Magnetoresistance Effect as a Magnetostrictive Effect

From the AMR as a function of B, it has been shown that above the saturation point, for temperatures near the peak of the AMR in temperature

6. Conclusions

and for high field strengths, the AMR begins to decrease. This data was shown in Figure ?? . By the interpretation given in the section 5.2.2 and from Equation 5.17 this would imply that as the field increases, carriers that were once JT polarons return to nearly-free double exchange type carriers by the application of a large magnetic field. Since a JTD involves a contraction in the a-b plane and an extension in the c-axis direction, the liberation of these carriers could be considered a magnetostrictive effect. Aligning the spins in the neighborhood of a JT distorted Mn^{+3} by the application of a large magnetic field might make a more cubic arrangement of the Mn ions energetically more favorable, thus destroying the JT distortion. In the presence of the high field, spins are aligned and the e_g electrons conduct easily by double-exchange.

This suggestion that the CMR phenomenon is a kind of magnetostrictive effect is also supported by the fact that the suppression of the resistivity does not seem to saturate with applied field in CMR materials [21]. If double-exchange alone were responsible, then for a reasonable field strength the effect could be expected to saturate when all the spins are aligned. In thin films, the required applied fields should be reasonably low, on the order of a few hundred oersted [7]. However, the effect fails to saturate for exceedingly large fields, and so it is likely that for large fields there is enough energy in the lattice to liberate roughly all the JT trapped electrons by magnetostriction.

Magnetostriction is a well-established effect that is discussed in at least one standard textbook [52]. Materials like pure nickel display negative magnetostriction. This means that when a magnetic field is applied to the material the lattice parameters parallel to the direction of the applied field are observed to contract. In contrast, permalloy is observed to show an extension in it's lattice parameters in the direction of an applied field.

Future Work

Though it would be prohibitive in terms of refitting the current apparatus to really deal well with AC currents, it would be quite interesting to apply an oscillating voltage to thin films of LCMO. This oscillating voltage could be applied in a MOSFET-type geometry, as shown in Figure 7.1. This might show an effect where none was seen earlier due to the time varying electric fields and possibly the induced magnetic fields. Incorporating AC fields and the piezoelectric thin films might also be interesting. A resonance in the resistivity of a CMR film that is below T_c might be expected for the correct oscillatory (phononic) frequency.

Part II

Electric Field Effect in LCMO and Preliminary Results on Depositions of PZT

Electric Field Effect

7.1 Motivation for Electric Field Effect Investigation

Solid state transistors based on CMR materials have been proposed in the race to keep up with the demand for increased microprocessor speed. It is expected that, if the resistance of a CMR material can be modulated using an external field, then the switching time of these materials from insulating to metallic-type conduction is expected to be on the order of 100's of GHz. This would represent a considerable leap ahead of conventional Si or GaAs technologies that, given theoretical and practical constraints, will find it difficult to exceed oscillation speeds of 10 GHz or more [33].

It is well established that the resistivity of these materials changes by large amounts under the influence of an applied magnetic field in the transition region. However, magnetic fields do not lend themselves readily to FET geometries. If the resistance of a CMR film was able to be modulated with an electric field, in a manner directly analogous to conventional semiconductor devices, then FETs based on these devices would become much more practical.

The relevant parameter for an electric field effect would be the density of carriers. This density may change the crystal field to such a degree that a phase change is induced in the material. Certain work has been done that might lead one to believe that a band picture not unlike the simple one applied to semiconductors has some relevance to CMR manganites [60, 71].

7.2 Experimental

7.2.1 Inorganic Gate Insulator

In order to carry out the electric field measurements in the FET structure, a gate dielectric was required. The breakdown voltages of candidate insulative materials were measured using the four-point probe instrumentation. Stacks of thin films were deposited by sputtering or evaporation. A metallic contact layer was deposited, followed by the dielectric then followed by another metallic contact layer, making a thin film parallel plate capacitor. The contact metal used was Al and the substrate material was microscope slide glass.

The first candidate material explored was AlO_3 . Bulk AlO_3 has a breakdown voltage of 13.6 V [31]. AlO_3 was deposited by electron beam (e-beam) evaporation and RF sputtering and the highest breakdown voltage achieved was 8 V, with a considerable leakage current. SiO_2 was also tried, since this was the gate dielectric material of choice in modern semiconductor applications. The breakdown voltage in bulk SiO_2 is approximately 400 to 500 V [31]. Initially, depositions done by RF sputtering yielded breakdown voltages in the range of 30 to 40 V, with leakage currents before breakdown of ~ 10 nA. Annealing the thin films of SiO_2 in air for 2 hours at 200°C improved the breakdown voltage of the films beyond 100 V, which was the maximum applied voltage available from the apparatus at that time. The films could

withstand prolonged exposure to 100 V with leakage currents from 2 to 5 nA. Annealing in air for 3 hours had detrimental effects on the dielectric strength of the material.

7.2.2 Organic Gate Insulator

The use of polymers as gate dielectrics is attractive due to their very high breakdown voltages [31]. The capacitor grade Mylar C film manufactured by Dupont quotes a breakdown voltage of 225 V across a 1.5 μm sheet of their polymer (see Appendix F), likely better than any inorganic film deposited in the lab by a factor of 2.

A thin film capacitor was constructed using silicon wafer and sputter deposited aluminum and the 1.5 μm thick film of Mylar C as a dielectric. To confirm that the capacitance was as expected, this capacitor was placed in a simple RC circuit. Small capacitances to ground or between the wires of the circuit were neglected. Circular thin films of aluminum with a diameter of 25.2 mm were deposited on two pieces of glass microscope slide and on two pieces of Si wafer. The two pieces of glass slide and Si wafer were clamped on either side of the 1.5 μm thick Mylar C film to make a cylindrical parallel-plate capacitor.

Contact was made to the Al thin films by pressing Indium. The capacitors were each placed in separate RC circuits, in series with a standard 1 k Ω resistor. Using a digital Lock-In Amplifier with a built-in AC voltage source, measurements of the phase difference between the incoming and outgoing voltages were made on both the glass slide capacitor and the Si capacitor. Using Equation A.3 and these measurements, the capacitance of these capacitors can be found. This capacitance was subsequently used to find the thickness of the dielectric spacer and was compared against 1.5 μm . A thick-

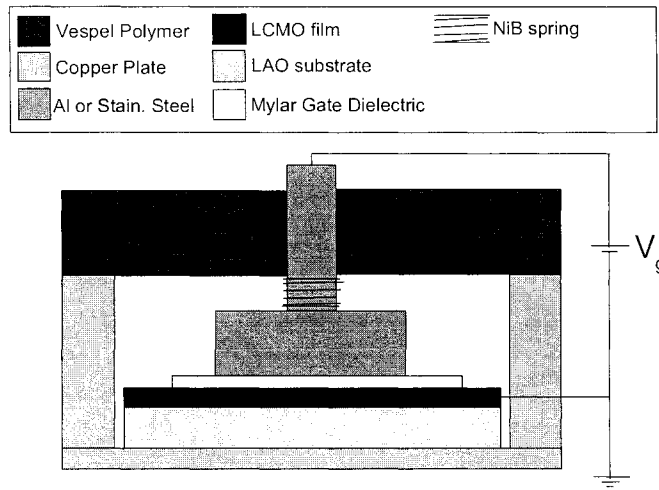


Figure 7.1: A schematic of the gate electrode used in the E-field effect measurement. The gate electrode is mechanically clamped to the sample by a NiB spring. The film and the gate voltage have a common ground.

ness of $\sim 3 \mu\text{m}$ was found and this was the distance used in all subsequent calculations.

Also, the breakdown voltage of the Mylar C film was tested using the Si wafer capacitor. It was found to correspond well to the expected value of 225 V.

A sample holder containing a macroscopic gate was machined. The geometry of this sample holder is shown schematically in Fig 7.1. The bottom portion was made from Cu to ensure good thermal conductivity, the top portion was made from a rigid insulating polymer called Vespel and the electrode was made from both Al for the rectangular geometry and stainless steel for the cylindrical geometry. The spring was made from a Nickel Boride (NiB) material. All materials used are non-magnetic.

To ensure that the gate electrode was flat, containing no protrusions that might puncture the $1.5 \mu\text{m}$ thick mylar film, the gate electrode was polished

to a near mirror finish using a fine grit polishing paper. Using a piece of Si wafer sputter coated with Al, the breakdown voltage was tested again and found to correspond well with the 225 V expected.

7.2.3 Electric Field Measurements and Results

Strong Electric Fields on the order of 1×10^7 V/m were applied to the LCMO thin films CO3 and CO4 using the gate dielectric electrode and the organic dielectric. The resistivity of the films was measured using the same cryostat used for the resistivity measurements described in Section 3.2.1. High voltage was applied to the channel of a MOSFET geometry shown in Figure 7.1 at room temperature and at 242K, a temperature where the anisotropy is a maximum.

This test was done by manually measuring the current-voltage (IV) characteristics of the LCMO thin film for a given applied gate voltage (V_g). Also, an automated routine written into the software to assess the effect. The gate voltage was stepped and the voltage required to drive a constant current through the LCMO film was measured.

No modulation of the resistivity of the LCMO thin film was observed for an applied electric field of $\sim 1 \times 10^7$ V/m or less at room temperature or at 240 K, in the middle of the transition.

7.3 Discussion of Electric Field Effect

A response to an electric field might have been expected based on carrier density. At a certain carrier density, the material might return to its Mott insulating state. That is, if enough electrons are drawn into this p-type material, with the coulomb repulsion ensuring that filling does not exceed one electron per Mn site, then the material has no vacant k vectors, its band

is full, and conduction cannot occur.

In retrospect, it seems unlikely that an electric field effect should modulate the resistivity in these materials. Phonons are likely insensitive to an applied electric field in these materials. So if an electron-phonon interaction is responsible for the large increase in the resistivity of these materials then the resistivity will probably be insensitive to an applied electric field as well. Also, the Stark effect on the e_g orbitals is zero. A lowering of the energy of the occupied e_g orbital, and the resulting increase in localization, does not seem possible by the application of an electric field.

That no effect was observed above T_c or near the transition for a large applied electric field is corroborated by other studies [48]. The only electric field effect that has been observed has been suspected to be due to the piezoelectric properties of the STO substrate at low temperatures [54].

To observe an electric field effect in these materials a p-n junction can be used. One way to create this junction is to epitaxially deposit hole doped, “p-type” LCMO onto Nb-doped STO, which is an electron-doped, “n-type” transition metal oxide.

By analogy, if an electric field is applied to a p-type semiconductor away from any depletion region there is no measurable effect on the resistivity of the material. This is what is observed for LCMO. However, an experiment on a p-n junction between LCMO and Niobium-doped SrTiO₃ (Nb:STO), which is an n-type transition metal oxide, should be attempted. Also, another type of material that could be useful in this area is La_{1-x}Sn_xMnO₃, which is an n-type material and may have a better lattice matching in the junction. Other possible technical problems, like diffusion of one atomic species into the other film or the formation of an unwanted compound at the epitaxial interface, might also be eliminated since the only difference between the two compounds

is the dopant atom. Recently there have been some successful resistivity modulations based on electric field or strain effects. In these experiments a p-n junction and PZT were used as the gate [67].

Also, recent experiments with oxygen deficient CMR materials seems to have yielded some resistance modulation [49] under an applied electric field.

7.4 Summary of Electric Field Effect

It has been shown convincingly that even the application of very high electric fields to these materials has no measurable effect. An investigation as to the effect of a p-n junction in these materials would be useful to undertake. In this vein, an array of n-type materials and different junction geometries could be investigated.

Preliminary PZT Deposition Results

8.1 Usefulness of PZT in a CMR Context

Ferroelectric materials have presented many interesting properties analogous to ferromagnetics including large remnant dipole moments and hysteresis of polarization [15]. However, perhaps one of the most useful applications of ferroelectrics to date has been in the area of acoustical transducers or Micro Electrical Mechanical Systems (MEMS) [30]. These applications are made possible by the electrostrictive or piezoelectric properties that ferroelectrics display.

Many materials display piezoelectric properties. SiO_2 is a weak piezoelectric material, having piezoelectric coefficients on the order of 1 pC/N [24]. ZnO is often used in thin film piezoelectric for miniature microphone or electrical microactuator applications [30] due to the simplicity of its chemical formula and therefore the relative ease of deposition. However, if larger piezoelectric coefficients are required then other more complicated solids are employed. In this area, the standard material has become $\text{PbZr}_{1-x}\text{Ti}_x\text{O}_3$ (PZT).

The resistivity of CMR compounds is strain dependent [72]. Previous

investigations of strain effects in thin films of CMR manganites have been limited to strain induced by substrate film lattice mismatch [72]. These investigations show clearly that there is a trend in the resistivity with strain, but are limited by the lattice parameters of the available substrates. They are not able to show detailed data probing strain effects in the film on the sub-angstrom level. Since piezoelectric materials can deform on the order of angstroms per volt, the resistivity of the LCMO thin film as a function of strain applied by a piezoelectric could be measured in a very detailed way. This could provide a more thorough insight into the dependence of the material's resistivity on strain.

In addition, an AC electric field can cause acoustical waves to propagate from the piezoelectric, in the same manner as macroscopic ultrasound devices. The frequencies accessible should be on the order of kHz to MHz, given the vibrational frequencies of a typical MEMS device [15, 53]. In this way, the frequency response of an LCMO film subject to AC strains applied by a thin film piezoelectric transducer could be investigated. This information could potentially be very interesting, as the effect of low energy lattice vibrations on the resistivity of the material could be probed in this manner. If phonons are important to charge transport in these materials then this type of experiment may provide a means to explore similar vibrational modes to those that might arise near the Curie temperature.

8.2 PZT Technical Background

PZT with a doping level of $x = 0.53$ gives a very large piezoelectric coefficient. This doping level is close to the so-called morphotropic phase boundary of the material, which is at $x = 0.54$. At low doping, PZT has a tetragonal crystal structure, with the same in-plane lattice parameter $|\bar{a}|$ and a longer

out-of-plane lattice parameter $|\bar{c}|$. At doping levels of 0.53 and above, the c- and a-axes no longer differ in length and the material takes on a rhombohedral unit cell [28]. Close to but below the boundary doping level, the piezoelectric coefficient of the material is a maximum.

The lattice parameters of PZT have been measured by XRD and by an X-ray Standing Wave (XSW) technique [38, 69]. Though the substrates for the two investigations differ, there is good agreement between the quantities. The lattice parameters for PZT are listed in Table 8.1.

It has been shown that optimally doped ($x=0.53$) single crystal, c-axis oriented films of PZT have interesting properties, such as large remnant polarizations, on the order of $50 \mu\text{C}/\text{cm}^2$, and large piezoelectric constants, on the order of $100 \text{ pC}/\text{N}$ [17], or equivalently, an in plane electrostrictive coefficient d_{33} of approximately $1 \text{ \AA}/\text{V}$ [63]. It is suspected that these effects are not as pronounced in polycrystalline specimens of PZT simply because the multitude of grains and different crystallographic orientations promote the formation of ferroelectric domains that can arrange themselves in a way so as to reduce their depolarization energy, and thus the remnant polarization of the material.

It is well documented that the resistivity of a CMR material varies as a function of lattice strain [43]. In a thin film stack consisting of alternating layers of LCMO and PZT, it should be possible to modulate the resistivity of

Table 8.1: Lattice Parameters of PZT on STO and (111) Pt-buffered Si by X-Ray Diffraction and an X-Ray Standing Wave technique for the tetragonal crystal structure compositions near the morphotropic boundary. [38, 69]

Lattice Parameter	Length [\AA]
a	4.02
c	4.13

Table 8.2: Important Off-Axis RF Sputter Deposition Parameters for PZT from Procedures at Two Different Temperatures [59, 5]. The parameter $d_{sub-targ}$ is the distance from the substrate to the target.

T_{substr}	Parameter	Value
650°C	P_{O_2}	1 [mTorr]
	P_{Ar}	9 [mTorr]
	Power	40-50 [W] (over 2" target)
	$d_{sub-targ}$	80 [mm]
	x_{target}	0.53 + 0.2 mol percent PbO
	substrate	Pt-buffered (100) MgO
	Post-Anneal	none
100°C	$P_{O_2} + P_{Ar}$	15 [mTorr]
	Power	60 [W]
	$d_{sub-targ}$	3.8 [cm]
	x_{target}	0.53
	substrate	(100) MgO
	Post-Anneal	10-20 [min], 600-650°C in air

a CMR thin film by utilizing the strain resulting from an adjacent piezoelectric thin film under an applied electric field. Lattice matching between PZT and CMR manganites has been found to be good, meaning that epitaxial growth of one substance on another is possible [73, 39].

8.3 PZT Depositions

Initial literature searches for PZT deposition parameters using RF sputtering revealed two plausible methods, one at high temperatures and one at low temperatures [59, 5]. The parameters of these procedures are listed in Table 8.2. The low temperature deposition method was attractive since a metallic mask could be used, eliminating a time consuming lithographic step. At high temperatures, the presence of a metal mask may contaminate the thin films.

PZT with a target doping level of $x = 0.53$ was deposited on numerous Si substrates at low temperature for calibration purposes. Since the low-temperature deposition procedure was not specific, the $O_2:Ar$ partial pressure ratio used was varied from sample to sample. The details of these depositions are given in Table 8.3. These test films were then patterned using conventional lithography and etched using Buffered Oxide Etch (BOE). BOE is a standard etchant that is mostly hydrofluoric acid (HF). From this, optical profilometry using the Tencor Alpha Step 200 and Zygo Interferometer was done.

From the work on PZT the two most relevant factors were film orientation and film stoichiometry. The film orientation desired was c-axis (001) orientation with the optimal doping level of $x=0.53$. X-Ray Diffractometry (XRD) was done on PZT samples deposited on [100] MgO substrates to determine the PZT film orientation. These substrates have a lattice constant of 4.04 \AA , so the lattice matching between PZT and these films is reasonably good.

X-ray Photoelectron Spectroscopy (XPS) was done on the PZT samples deposited on MgO in an attempt to measure their stoichiometry. The local environment and bonding can be probed by measuring electrons expelled from these bonds for a known incident x-ray energy. The ejected electrons are counted by an electrostatic or magnetic detector and those results are multiplied by an empirical sensitivity factor. These measurements should be accurate to within a few percent, which is a relatively high degree of accuracy. The results of these measurements is essentially an atomic percentage which can be normalized, or in whatever way manipulated, for the atomic species of interest. A chemical formula can be derived from these atomic percentages.

The effect of annealing on the PZT samples deposited on MgO was investigated as well. It was possible that annealing in air at a high enough

Table 8.3: Off-Axis RF Sputter Deposition Parameters for PZT Test Films on (100) Silicon Made to Calibrate Deposition and Etch Rates. The parameter $d_{sub-targ}$ is the distance from the substrate to the target, the power to the two inch target was 50 W, the substrate was at ambient temperature and the doping level of the target is $x=0.53$.

Sample	Parameter	Value
PZT-1	P_{O_2}	1 [mTorr]
	P_{Ar}	9 [mTorr]
	$d_{sub-targ}$	3.5 [cm]
	$t_{deposition}$	65 [min]
	t_{etch}	120 [s]
	thickness	135 [nm]
	Deposition Rate	2.07 [nm/min]
	Etch Rate	1.12 [nm/s]
PZT-3	P_{O_2}	1 [mTorr]
	P_{Ar}	9 [mTorr]
	$d_{sub-targ}$	3 [cm]
	$t_{deposition}$	85 [min]
	t_{etch}	180 [s]
	thickness	~44 [nm]
	Deposition Rate	0.52 [nm/min]
	Etch Rate	0.34 [nm/s]
PZT-5	P_{O_2}	10 [mTorr]
	P_{Ar}	10 [mTorr]
	$d_{sub-targ}$	3 [cm]
	$t_{deposition}$	85 [min]
	t_{etch}	90 [s]
	thickness	331 [nm]
	Deposition Rate	2.19 [nm/min]
	Etch Rate	3.68 [nm/s]

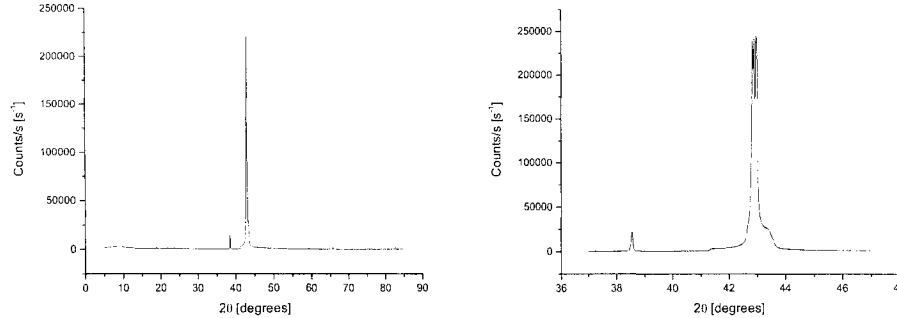


Figure 8.1: X-Ray diffraction of bare [100] MgO substrates. The substrates display a very strong singular orientation. Left: The full X-Ray spectrum. Right: A close up on the X-Ray peak.

temperature could assist in correct stoichiometry, [001] orientation and cause an increase in grain size.

8.4 Preliminary PZT Deposition Analysis and Results

An etch rate for PZT on Si was found using Buffered Oxide Etch (BOE), and the deposition rate for PZT for our sputtering geometry at low temperatures was determined. These parameters are considered to be technical, and are given in Table 8.3.

8.4.1 X-Ray Diffraction on PZT Thin Films

XRD data was taken on the PZT films on MgO for both the high and low temperature deposition methods.

The results from the high temperature deposition are shown in Figure 8.2. One can see that a distinctive peak is present, showing that the film is strongly oriented. However, this peak does not compare well with the lo-

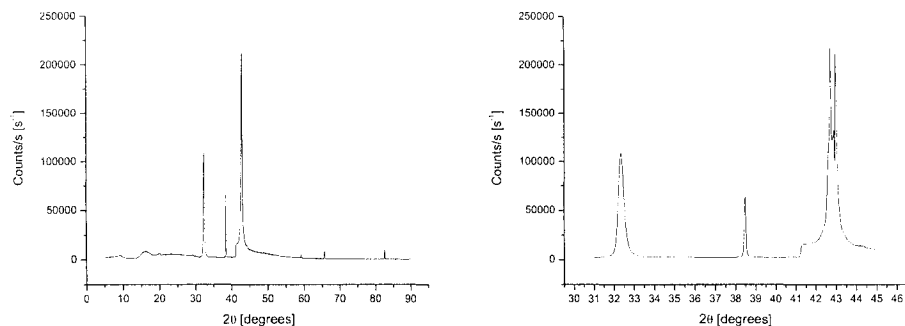


Figure 8.2: XRD of the high temperature deposition of PZT. The data shows a new peak at a lower angle than the other peaks. This peak angle corresponds well to the undesirable (110) PZT crystallographic orientation. Left: The full spectrum. Right: A close up of the area of interest.

cation of a [001] diffraction peak and in fact appears to correspond well with the [110] lattice spacing. This peak's relative height and location is insensitive to annealing, at least on the time scale of about 1 hour. It is doubtful that the film orientation will change with longer annealing times, especially given the results from the XPS investigation that will be shown in section 8.4.2.

The results from the low temperature deposition are somewhat more involved. The procedure necessitates an anneal at 650°C for approximately 20 min. After the anneal an XRD peak in the appropriate location for the [001] oriented PZT appeared in the spectrum. This shows that the film likely became strongly c-axis oriented after the anneal. The appropriate XRD spectra are shown in Figure 8.3. There is an anomalous feature that shows up at low angles in the spectra after the first anneal. This feature is addressed briefly in section 8.5.

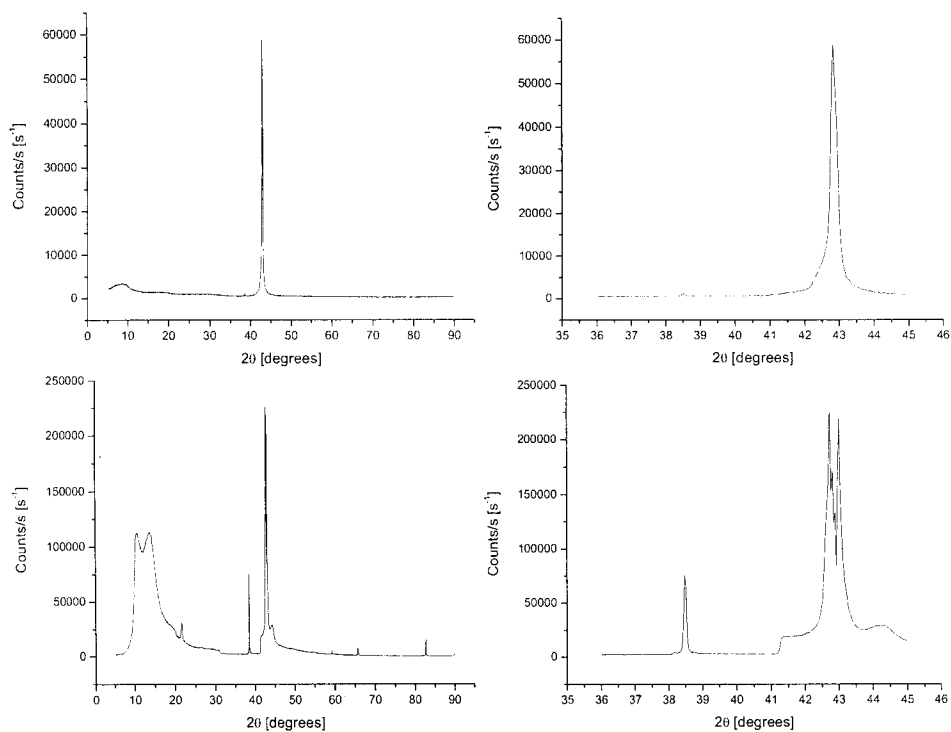


Figure 8.3: XRD spectrum of the low temperature deposition procedure for PZT. Top: The XRD spectra of the PZT thin film before annealing. Bottom: The spectra show the appearance of the desired [002] c-axis oriented peak after the 650°C anneal. There is a new peak at the required [002] location. The peak remains undisturbed after longer anneal times. An anomalous feature shows up at low angles after the first anneal.

8.4.2 X-Ray Photoelectron Spectroscopy of PZT Thin Films

The XPS measurements were done to determine the stoichiometry of the PZT films.

For the high temperature deposition, the formula arrived at was approximately $\text{PbZr}_{0.5}\text{Ti}_{0.5}\text{O}_{15}$. The ratio of Zr and Ti relative to one another is found to be roughly 1:1. This shows that the doping level was close to the optimal level of $x=0.53$, but the oxygen content is shown to greatly be in excess of what is required. Since the formula is normalized to the level of Pb, this likely indicates a loss of Pb in the film.

The low temperature deposition gave a chemical formula for the PZT of $\text{PbZr}_{0.4}\text{Ti}_{0.6}\text{O}_{2.5}$. This doping level is $x=0.6$. It is above the morphotropic boundary, where the electromechanical properties of the film are very much reduced. However, the oxygen content is similar to the expected value of three, meaning that the PbO content in the film is likely correct.

As a caveat to this work, it is important to note that the thin films were exposed to air before the XPS analysis was done. While some sputtering of the PZT surface was done to remove the layer of adsorbed oxygen atoms, these oxygen ions may have an influence on the amounts of oxygen measured in the PZT films.

8.5 Discussion of Preliminary Work on PZT

The deposited PZT has two problems, corresponding to the relative temperatures at which the materials were deposited.

High Temperature Deposition

At high temperature 650°C the Zr to Ti ratio was acceptable. The ratio fell a few percent from 53:47 to roughly 50:50, as the film lost Ti in favor of Zr. This loss could be due to resputtering of the film under bombardment with the plasma, reducing the content of the lighter Ti element, or due to a lower sputtering rate of the heavier Zr element. However, the Pb and oxygen contents of the film were well away from what is stoichiometrically correct. The Pb content dropped to nearly $\frac{1}{3}$ of what was required. This is consistent with other recipes found in the literature, who state that an excess of PbO is necessary for quality deposits of PZT. This is because PbO volatilizes at high temperatures [59]. X-ray diffraction of these films do not show a strong *c*-axis orientation of the films on MgO. The film orientation recovered from this deposition method was (110) oriented. This is likely due to the fact that the Pb level within the film is so far away from correct. It is unlikely that the material will demonstrate the strong piezoelectric properties required for further experimentation.

A possible solution for this problem might be to deposit a seed layer of Pb either onto the substrate before depositing PZT or after depositing PZT onto the thin film stack. This stack could then be annealed in oxygen at low temperature for a long time in order to allow the Pb to diffuse into the PZT film and make up for the lack of Pb seen in the XPS analysis. The oxygen environment should ensure that even with the addition of this new Pb, the film will be fully oxidized. After this procedure is complete, the film could be etched in a lead etch, and then dipped quickly (~ 5 s) in HCl in order to remove any excess Pb and PbO left on the surface. HCl is known for its ability to etch traces of metal oxides. This solution would be limited by the mobility of Pb or PbO in the PZT lattice at moderate annealing

temperatures.

Low Temperature Deposition

At low temperatures of 150°C the Pb and oxygen contents are as required. However, the Zr to Ti ratio is skewed by XPS measurements to 40:60. This composition is above the morphotropic boundary, $x=0.53$, where the maximum electromechanical response is found. As a result the electrostrictive properties of the film are greatly reduced. This discrepancy is again likely due to preferential sputtering at the target or resputtering at the film at low temperatures, where the thermal energy is not enough to either activate the sputtering of the heavier element from the target or enhance the resputtering of the heavier element from the film. X-ray diffraction analysis shows that these films are likely [001] oriented, as required. However, it is doubtful that the electromechanical response of the film would be sufficient to strain an epitaxially deposited LCMO thin film by an amount that would be measurable in the resistivity.

Again, seed layers of Ti could be deposited and annealed in oxygen, and that may help to increase the Zr to Ti ratio. However, this type of solution adds complications and lengthy steps to the deposition, which would make it highly inefficient to fabricate PZT thin films in this way.

Anomalous Feature in XRD Spectrum

During annealing of the PZT samples on MgO in air after the low temperature deposition, a large anomalous feature appears at low diffraction angles. This feature might be due to gaseous atoms diffusing into the MgO lattice at high temperatures and sitting at interstitial sites, though the intensity and order required for the interstitial atoms to show up in the XRD spectrum this way makes this explanation unlikely. Gaseous atoms of nitrogen or oxygen

may also be reacting with the MgO at high temperature to form new solid phases. This feature grows and broadens with annealing time.

A similar feature was also observed on older MgO substrates. MgO substrates are known to age and must be kept away from moisture. This feature may be a result of the thermal annealing in air prematurely aging the substrate.

8.6 PZT Summary

The result of these experiments is that neither of the two methods tried have yielded immediately useful results for depositing (001) oriented, optimally doped PZT thin films. The easiest and most costly means of rectifying the problem would simply be to purchase a new sputter target with a composition that compensates for the problems that arise during RF sputtering.

In the high temperature case, the target must contain an excess of 20% PbO by mol in order to compensate for PbO loss due to volatilization. These problems perhaps make it more obvious why PZT is often fabricated by sol-gel methods [19].

In the low temperature case, the target doping level could also be changed. At this temperature the target loses roughly 13% of its Zr relative to Ti. This can easily be compensated for by purchasing a target that is 66% Zr and 34% percent Ti. This kind of target is available commercially. The low temperature deposition is also attractive because it allows for the use of physical masks. This eliminates the need for long, complicated and potentially dangerous lithography steps using BOE (49% HF) as an etchant for PZT.

Troubleshooting a method by which to fabricate a thin film of PZT with c-axis orientation and a composition near the morphotropic phase boundary has proven to be somewhat complicated. On the next iteration, perhaps with

a new target, it will likely be solved. Once this procedure is in place, it would be interesting to do detailed measurements of the effects of strain on CMR compounds above, below and in the transition temperature region.

The electromechanical response of the PZT film against the thickness of the LCMO must be qualified. The strains attainable from the PZT will almost certainly be severely limited by contact to the substrate. If the strains prove too small, then the next recourse would be to make LCMO-PZT thin film composite bridges. These bridges would be etched free of the substrate, leaving the layers of PZT and LCMO free to bend in a manner similar to many MEMS devices. Since the substrate typically limits the strain present in the films, without direct contact to the substrate the strain in the thin films would be much greater. The oscillatory speed of such a beam might be of interest for technological applications.

BIBLIOGRAPHY

- [1] C.P. Adams, J.W. Lynn, Y.M. Mukovskii, A.A. Arsenov, and D.A. Shulyatev. Charge ordering and polaron formation in the magnetoresistive oxide $\text{La}_{0.7}\text{Ca}_{0.3}\text{MnO}_3$. *Physical Review Letters*, 85(18), 2000.
- [2] V.S. Amaral, A.A.C.S Lourenço, J.P. Arajo, A.M. Pereira, J.B.Sousa, P.B. Taveres, J.M. Vieira, E. Alves, M.F. da Silva, and J.C. Soares. Anisotropic electrical transport in epitaxial $\text{La}_{2/3}\text{Ca}_{1/3}\text{MnO}_3$ thin films. *Journal of Applied Physics*, 87(9):5570-5572, 2000.
- [3] P.W. Anderson and H. Hasegawa. Considerations on double exchange. *Physical Review*, 100(2):675-681, 1955.
- [4] A. Asamitsu, Y. Moritomo, R. Kumai, Y. Tomioka, and Y. Tokura. Magnetostructural phase transition in $\text{La}_{1-x}\text{Sr}_x\text{MnO}_3$ with controlled carrier density. *Physical Review B*, 54(3), 1996.
- [5] Nasir Abdul Basit, Hong Koo Kim, and Jean Blachere. Growth of highly oriented $\text{Pb}(\text{Zr},\text{Ti})\text{O}_3$ films on MgO-buffered oxidized Si substrates and its application to ferroelectric nonvolatile memory field-effect transistors. *Applied Physics Letters*, 73(26), 1998.
- [6] B.I. Belevtsev, V.B. Krasovitsky, D.G. Naugle, K.D.D. Rathnayaka, A. Parasiris, S.R. Surthi, R.K. Pandey, and M.A. Rom. Transport and magnetic anisotropy in CMR thin film $\text{La}_{1-x}\text{Ca}_x\text{MnO}_3$ ($x \approx 1/3$) induced by a film-substrate interaction. *physica status solidi (a)*, 188(3):1187-1207, 2001.

BIBLIOGRAPHY

- [7] L.M. Berndt, Vincent Balbarin, and Y. Suzuki. Magnetic anisotropy and strain states of (001) and (110) colossal magnetoresistance thin film. *Applied Physics Letters*, 77(18), 2000.
- [8] A.V. Boris, N.N. Kovaleva, A.V. Bazhenov, A.V. Samoilov, N.-C. Yeh, and R.P. Vasquez. Infrared optical properties of $\text{La}_{0.7}\text{Ca}_{0.3}\text{MnO}_3$ epitaxial thin films. *Journal of Applied Physics*, 81(8), 1997.
- [9] B.H. Bransden and C.J. Joachain. *Quantum Mechanics*. Prentice Hall, second edition, 2000.
- [10] B.J. Campbell, S.K. Sinha, R. Osborn, S. Rosenkranz, J.F. Mitchell, D.N. Argyriou, L. Vasiliu-Doloc, O.H. Seeck, and J.W. Lynn. Polaronic orbital polarization in a layered colossal magnetoresistive manganite. *Physical Review B*, 67(020409), 2003.
- [11] Tapan Chatterji, editor. *Colossal Magnetoresistive Manganites*. Kluwer Academic Publishers, 2004.
- [12] C. Şen, G. Alvarez, and E. Dagotto. Insulator-to-metal transition induced by disorder in a model for manganites. *Physical Review B*, 70(064428), 2004.
- [13] M. Daghofer, W. Koller, H.G. Evertz, and W. von der Linden. Polaronic aspects of the ferromagnetic two-dimensional Kondo model. *Journal of Physics: Condensed Matter*, 16:5469–5482, 2004.
- [14] S. Dai, Z.W. Li, A.H. Morrish, X.Z. Zhou, J.G. Zhao, and X.M. Xiong. Colossal magnetoresistance in $(\text{La}_{0.7}\text{Sn}_{0.3})_2\text{Mn}_2\text{O}_7$. *Physical Review B*, 55(21), 1997.
- [15] Dragan Damjanovic. Ferroelectric, dielectric and piezoelectric properties of ferroelectric thin films and ceramics. *Reports on Progress in Physics*. 61:1267–1324, 1998.
- [16] J.P. Franck, I. Issac, and D.D. Lawrie. Oxygen isotope effect in $\text{La}_{0.8}\text{Sr}_{0.2}\text{MnO}_{3+\delta}$ and its dependence on oxygen stoichiometry. *Physical Review B*, 64(214412), 2001.
- [17] Desheng Fu, Hisao Suzuki, Takesi Ogawa, and Kenji Ishikawa. High-piezoelectric behavior of c-axis-oriented lead zirconate titanate thin films with composition near the morphotropic phase boundary. *Applied Physics Letters*, 80(19), 2002.

BIBLIOGRAPHY

- [18] Nobuo Furukawa. Anomalous shift of chemical potential in the double exchange systems. *Journal of the Physical Society of Japan*, 66(8):2523–2524, 1997.
- [19] J.G.E. Gardeniers, A. Smith, and C. Cobianu. Characterization of sol-gel PZT films on Pt-coated substrates. *Journal of Micromechanics and Microengineering*, 5:153–155, 1995.
- [20] P.-G De Gennes. Effects of double exchange in magnetic crystals. *Physical Review*, 118(1):141–154, 1960.
- [21] Guo-Qiang Gong, Chadwick Canedy, and Gang Xiao. Colossal magnetoresistance of 1000000-fold magnitude achieved in the antiferromagnetic phase of $\text{La}_{1-x}\text{Ca}_x\text{MnO}_3$. *Applied Physics Letters*, 67(12), 1995.
- [22] John B. Goodenough. Spin-orbit-coupling effects in transition-metal compounds. *Physical Review*, 171(2):466–479, 1967.
- [23] David J. Griffiths. *Introduction To Quantum Mechanics*. Prentice Hall, 1995.
- [24] R. Holland and E.P. EerNisse. *Design of Resonant Piezoelectric Devices*. MIT Press, 1969.
- [25] H.A. Jahn and E. Teller. Stability of polyatomic molecules in degenerate electronic states I-Orbital degeneracy. *Proceedings of the Royal Society of London. Series A: Mathematical and Physical Sciences*, 161(905):220–235, 1931.
- [26] G. Jung, M. Indenbom, V. Markovich, C.J. Van der Beek, D. Mogilyanski, and Ya M. Mukovskii. Magneto-optics observation of spontaneous domain structure in ferromagnetic $\text{La}_{0.78}\text{Ca}_{0.22}\text{MnO}_3$ single crystal. *Journal of Physics: Condensed Matter*, 16:5461–5468, 2004.
- [27] Junjiro Kanamori. Crystal distortion in magnetic compounds. *Journal of Applied Physics*, S.31(5), 1961.
- [28] I. Kanno, S. Fuji, and R. Takayama. Piezoelectric properties of c-axis oriented $\text{Pb}(\text{Zr},\text{Ti})\text{O}_3$ thin films. *Applied Physics Letters*, 70(11), 1997.
- [29] Winfried Koller, Alexander Prüll, Hans Gerd Evertz, and Wolfgang von der Linden. Magnetic polarons in the one-dimensional ferromagnetic Kondo model. *Physical Review B*, 67(174418), 2003.

BIBLIOGRAPHY

- [30] Seung S. Lee and Richard M. White. Piezoelectric cantilever acoustical transducer. *Journal of Micromechanics and Microengineering*, 8:230–238, 1998.
- [31] David R. Lide, editor. *CRC Handbook of Physics and Chemistry*. CRC Press, 83rd edition, 2003.
- [32] Marcus Liebmann, Alexander Schwarz, Uwe Kaiser, Roland Wiesendanger, Dong-Wook Kim, and Tae-Won Noh. Magnetization reversal of a structurally disordered manganite thin film with perpendicular anisotropy. *Physical Review B*, 71(104431), 2005.
- [33] S. Luryi, J.M. Xu, and A. Zaslavsky, editors. *Future Trends in Microelectronics: The Nano Millennium*. Wiley Interscience, 2002.
- [34] Sadamichi Maekawa and Teruya Shinjo, editors. *Spin Dependent Transport in Magnetic Nanostructures*. CRC Press, 2002.
- [35] Ryo Maezono, Sumio Ishihara, and Naoto Nagosa. Phase diagram of manganese oxides. *Physical Review B*, 58(17), 1998.
- [36] A.P. Malozemoff. Anisotropic magnetoresistance with cubic anisotropy and weak ferromagnetism: A new paradigm. *Physical Review B*, 34(3), 1986.
- [37] N. Mannella, A. Rosenhahn, C.H. Booth, S. Marchesini, B.S. Mun, S.-H. Yang, K. Ibrahim, Y. Tomioka, and C.S. Fadley. Direct observation of high-temperature polaronic behavior in colossal magnetoresistive manganites. *Physical Review Letters*, 92(16), 2004.
- [38] D.L. Marasco, A. Kazimirov, M.J. Bedzyk, T.-L. Lee, S.K. Streiffer, O. Auciello, and G.-R. Bai. Atomic scale observation of polarization switching in epitaxial ferroelectric thin films. *Applied Physics Letters*, 79(4), 2001.
- [39] Frank McNally, Jin Hyeok Kim, and F.F. Lange. Fatigue properties of lanthanum strontium manganate-lead zirconate titanate epitaxial thin film heterostructures produced by a chemical solution deposition method. *Journal of Materials Research*, 15(7), 2000.
- [40] S. Mercone, C.A. Perroni, V. Cataudella, C. Adamo, M. Angeloni, C. Aruta, G. De Filippis, F. Miletto, A. Oropallo, P. Perna, A. Yu. Petrov, U. Scotti di Uccio, and L. Maritato. Transport properties in manganite thin films. *Physical Review B*, 71(064415), 2005.

BIBLIOGRAPHY

- [41] A.J. Millis. Cooperative Jahn-Teller effect and electron-phonon coupling in $\text{La}_{1-x}\text{A}_x\text{MnO}_3$. *Physical Review B*, 53(13), 1996.
- [42] A.J. Millis. Lattice effects in magnetoresistive manganese perovskites. *Nature*, 392:147–150, 1998.
- [43] A.J. Millis, T. Darling, and A. Migliori. Quantifying strain dependence in “colossal” magnetoresistive manganites. *Journal of Applied Physics*, 83(3), 1998.
- [44] A.J. Millis, P.B. Littlewood, and B.I. Shraiman. Double exchange alone does not explain the resistivity of $\text{La}_{1-x}\text{Sr}_x\text{MnO}_3$. *Physical Review Letters*, 74(25), 1995.
- [45] A.J. Millis, R. Mueller, and Boris I. Shraiman. Fermi-liquid-to-polaron crossover. I. General results. *Physical Review B*, 54(8):5839–5404, 1996.
- [46] A.J. Millis, R. Mueller, and Boris I. Shraiman. Fermi-liquid-to-polaron crossover. II. Double exchange and the physics of colossal magnetoresistance. *Physical Review B*, 54(8):5405–5417, 1996.
- [47] B.C. Nam, W.S. Kim, H.S. Choi, J.C. Kim, N.H. Hur, I.S. Kim, and Y.K. Park. Effect of oxygen annealing on the magnetoresistance in $\text{La}_{0.7}\text{Sr}_{0.3}\text{MnO}_3$ epitaxial films. *Journal of Physics D: Applied Physics*, 34:54–59, 2001.
- [48] S.B. Ogale, V. Talyansky, C.H. Chen, R. Ramesh, R.L. Greene, and T. Venkatesan. Unusual electric field effects in $\text{Nd}_{0.7}\text{Sr}_{0.3}\text{MnO}_3$. *Physical Review Letters*, 77(6), 1996.
- [49] I. Pallecchi, L. Pellegrino, E. Bellingeri, A.S. Siri, and D. Marré. Effects of electric and magnetic fields on phase-separated $\text{La}_{0.7}\text{Sr}_{0.3}\text{MnO}_{3-\delta}$. *Physical Review B*, 71(014406), 2005.
- [50] Soo Hyun Park, Yoon-Hee Jeong, and Ki-Bong Lee. Specific heat and resistivity of a double-exchange ferromagnet $\text{La}_{0.7}\text{Ca}_{0.3}\text{MnO}_3$. *Physical Review B*, 56(1), 1997.
- [51] R.K. Pathria. *Statistical Mechanics*. Pergamon Press, first edition, 1972.
- [52] Martin A. Plonus. *Applied Electromagnetics*. McGraw-Hill Inc, first edition, 1978.

BIBLIOGRAPHY

- [53] W.P. Robbins, D.L. Polla, T. Tamagawa, D.E. Glumac, and W. Tjhen. Design of linear-motion microactuators using piezoelectric thin films. *Journal of Micromechanics and Microengineering*, 1:247–252, 1991.
- [54] G. Rupprecht and W.H. Winter. Electromechanical behavior of single-crystal strontium titanate. *Physical Review*, 155(3):1019–1028, 1967.
- [55] M.B. Salamon and M. Jaime. The physics of manganites: Structure and transport. *Reviews of Modern Physics*, 73:583–628, 2001.
- [56] S. Satpathy, Zoran S. Popović, and Filip R. Vukajlović. Electronic structure of the perovskite oxides: $\text{La}_{1-x}\text{Ca}_x\text{MnO}_3$. *Physical Review Letters*, 76(6), 1996.
- [57] J.R. Sun, C.F. Yeung, K. Zhao, L.Z. Zhou, C.H. Leung, H.K. Wong, and B.G. Shen. Strain dependent vacuum annealing effects in $\text{La}_{1-x}\text{Ca}_x\text{MnO}_{3-\delta}$ films. *Applied Physics Letters*, 76(9), 2000.
- [58] J.R. Sun, H.W. Yeung, H.K. Wong, T. Zhu, and B.G. Shen. Effects of vacuum annealing on the transport property of $\text{La}_{0.67}\text{Sr}_{0.33}\text{MnO}_3$ films. *The European Physical Journal B*, 35(4):481–491, 2003.
- [59] Ryoichi Takayama and Toshihiro Tomita. Preparations of epitaxial $\text{Pb}(\text{Zr}_{1-x}\text{Ti}_x)\text{O}_3$ thin films and their crystallographic, pyroelectric and ferroelectric properties. *Journal of Applied Physics*, 60(4), 1989.
- [60] Hidekazu Tanaka, Jun Zhang, and Tomji Kawai. Giant electric field modulation of double exchange ferromagnetism at room temperature in the perovskite manganite-titanate p-n junction. *Physical Review Letters*, 88(2), 2002.
- [61] Yoshinori Tokura. Correlated electrons: Science to technology. *JSAP International*, (2):12–21, 2000.
- [62] Y. Tomioka, A. Asamitsu, Y. Moritomo, H. Kuwahara, and Y. Tokura. Collapse of a charge-ordered state under a magnetic field in $\text{Pr}_{1/2}\text{Sr}_{1/2}\text{MnO}_3$. *Physical Review Letters*, 74(25), 1995.
- [63] R.N. Torah, S.P. Beeby, and N.M. White. Experimental investigation into the effects of substrate clamping on the piezoelectric behavior of thick-film PZT elements. *Journal of Physics D: Applied Physics*, 37:1074–1078, 2004.

BIBLIOGRAPHY

- [64] S.V. Trukhanov, N.V. Kasper, I.O. Troyanchuk, M. Tovar, H. Szymchak, and K. Bärner. Evolution of magnetic state in the $\text{La}_{1-x}\text{Sr}_x\text{MnO}_{3-\gamma}$ ($x=0.3, 0.5$) manganites depending on the oxygen content. *Journal of Solid State Chemistry*, 169:85–95, 2002.
- [65] J.H. Van Vleck. The Jahn-Teller effect and crystalline stark splittings for clusters of the form XY_6 . *Journal of Chemical Physics*, 7:72–84, 1939.
- [66] Zhi-Hong Wang, G. Christiani, H.-U. Habermeier, Zhen-Rong Zhang, and Bao-Shan Han. Perpendicular magnetic anisotropy of $\text{La}_{0.77}\text{Sr}_{0.33}\text{MnO}_3$ thin films grown on CaMnO_3 buffered SrTiO_3 . *Journal of Applied Physics*, 94(8), 2003.
- [67] T. Wu, S.B. Ogale, J.E. Garrison, B. Nagaraj, Amlan Biswas, Z. Chen, R.L. Greene, R. Ramesh, and T. Venkatesan. Electroresistance and electronic phase separation in mixed-valent manganites. *Physical Review Letters*, 86(26), 2001.
- [68] N-C Yeh, R.P. Vasquez, D.A. Beam, C-C Fu, J. Huynh, and G. Beach. Effects of lattice distortion and Jahn-Teller coupling on the magnetoresistance of $\text{La}_{0.7}\text{Ca}_{0.3}\text{MnO}_3$ and $\text{La}_{0.5}\text{Ca}_{0.5}\text{CoO}_3$ epitaxial films. *Journal of Physics: Condensed Matter*, 9:3713–3721, 1997.
- [69] Shintaro Yokoyama, Yoshihisa Honda, Hitoshi Morioka, Shoji Okamoto, Takashi Iijima, Hirofumi Matsuda, Keisuki Saito, and Hiroshi Funakubo. Comparison study of (001)-/(100)-oriented epitaxial and fibre-textured $\text{Pb}(\text{Zr},\text{Ti})\text{O}_3$ thick films prepared by MOCVD. *Integrated Ferroelectrics*, 64:217–225, 2004.
- [70] Clarence Zener. Interaction between the d-shells in the transition metals. II. Ferromagnetic compounds of manganese with perovskite structure. *Physical Review*, 82(3):403–405, 1951.
- [71] Jun Zhang, Hidekazu Tanaka, and Tomji Kawai. Rectifying characteristic in all-perovskite oxide film p-n junction with room temperature ferromagnetism. *Physical Review Letters*, 80(23), 2002.
- [72] Jun Zhang, Hidekazu Tanaka, and Tomoji Kawai. Strain-induced insulator-metal transition and room-temperature colossal magnetoresistance in low-doped $\text{La}_{1-x}\text{Ba}_x\text{MnO}_3$ thin films. *Journal of Applied Physics*, 90(12), 2001.

BIBLIOGRAPHY

- [73] T. Zhao, S.B. Ogale, S.R. Shinde, R. Ramesh, R. Droopad, J. Yu, K. Eisenbeiser, and J. Misewich. Colossal magnetoresistive manganite-based ferroelectric field-effect transistor on Si. *Applied Physics Letters*, 84(5), 2004.
- [74] G. Zheng and C.H. Patterson. Ferromagnetic polarons in $\text{La}_{0.5}\text{Ca}_{0.5}\text{MnO}_3$ and $\text{La}_{0.33}\text{Ca}_{0.67}\text{MnO}_3$. *Physical Review B*, 67(220404), 2003.
- [75] M. Ziese. Spontaneous resistivity anisotropy and band structure of $\text{La}_{0.7}\text{Ca}_{0.3}\text{MnO}_3$ and Fe_3O_4 films. *Physical Review B*, 62(2), 2000.
- [76] M. Ziese and S.P. Sena. Anisotropic magnetoresistance of thin $\text{La}_{0.7}\text{Ca}_{0.3}\text{MnO}_3$ films. *Journal of Physics: Condensed Matter*, 10:2727–2737, 1998.

RC Circuit Analysis and Mylar Thickness Evaluation

A simple RC circuit has a transfer function of the form.

$$V_{out} = V_{in} \frac{1}{1 + j\omega RC} \quad (\text{A.1})$$

where V_{in} is the sinusoidal applied voltage, V_{out} is the sinusoidal voltage transferred, j is the $\sqrt{-1}$, ω is the angular frequency $2\pi f$, R is the circuit resistance and C is the circuit capacitance.

The magnitude and phase of the transfer function also have simple forms.

$$\frac{V_{out}}{V_{in}} = \frac{e^{-j\theta}}{1 + (\omega RC)^2} \quad (\text{A.2})$$

where θ is the complex phase of the transfer function, which in the complex plane follows the relation.

$$\tan \theta = C R \omega \quad (\text{A.3})$$

Using equally standard equations for the capacitance of a cylindrical parallel-plate capacitor, the spacing between the plates can be obtained.

This information was used to confirm that for flat, dust free mechanical electrodes clamped across the thin Mylar dielectric, the distance between the electrodes could be similar to $1.5 \mu\text{m}$. This is the thickness of the Mylar. If this distance is much larger than that, then it will severely hinder the magnitude of the electric field that was applied to the LCMO film, or the PZT/LCMO stack.

The value predicted from this experiment was approximately $3\mu\text{m}$. This is within error of the correct value and will not severely reduce the magnitude

APPENDIX A. RC Circuit Analysis and Mylar Thickness Evaluation

of an applied voltage. In all subsequent calculations of the magnitude of the electric field applied to the film, this value was used.

Spin-Orbit Coupling and Anisotropic Magnetoresistance

Original MRA Derivation

The total Hamiltonian includes the exchange splitting energy from the applied magnetic field.

$$H_{AMR} = -\mu_B \gamma H \cdot S + H_{SO} \quad (\text{B.1})$$

where H is just the applied magnetic field strength, μ_B is the Bohr magneton, γ is the gyromagnetic ratio and H_{SO} has been given in Equation 2.10.

The diagonal terms arising from the z direction can only contribute to the anisotropy if the orbital participating in the conduction itself has a spacial anisotropy. These terms will be addressed later.

When the second half of Equation 2.10, involving the raising and lowering operators, is treated in a perturbative approach, off-diagonal elements are produced between the spin up and spin down states. These off-diagonal terms mix the spin manifolds and the perturbed wavefunctions are a superposition of the original d-orbital states. With the Fermi Energy in the spin down band, the scattering of spin up or spin down electrons off of the perturbed states can be calculated and the resistivity estimated by computing the square of the relevant scattering matrix element.

$$\rho_{\uparrow,\downarrow} \approx |\langle i_{\uparrow,\downarrow} | \frac{1}{2} A (L_+ S_- + L_- S_+) | \psi_{orbital} \rangle|^2 \quad (\text{B.2})$$

where the $\langle i_{\uparrow,\downarrow} |$ corresponds to the state of an up or down spin conduction electron and $|\psi_{orbital}\rangle$ is the relevant superposition of wavefunctions.

The perturbative calculation can be carried out to second order. The second order approximation is justified by the fact that a first order approximation to the energy provides modifications that are to second order in the resistivity. Therefore, since the energy modification is a second order effect, it is important to treat the wavefunctions to second order as well. Different scattering amplitudes and thus different resistivities are found for different combinations of matrix elements. These resistivities are specific to spin orientation, but by taking appropriate averages one can work back to a comparison with experiment.

In terms of the diagonal $L_z S_z$ scattering mechanism, to first order this effect is often negligible. However, if these splittings are not ignored, or if the spin-orbit coupling is particularly large then to second order in a perturbed wavefunction calculated from the additional zeroth-order contributions to the energy, $L_z S_z$ terms can lead to increased scattering. Within one spin band, if one computes “diagonal” matrix elements with the second order perturbed wavefunctions one can see that the probability that an electron has of scattering off a particular orbital is increased. This effect is unique to this spin-mixing scattering mechanism in that it does not rely on any mixing between spin up and spin down states in order to change the scattering probability. It is a source of anisotropy that affects both the spin up and spin down channels equally.

This formulation has some obvious flaws. This picture completely neglects the band structure of the material in question. Also, in the Smit mixing scheme one would expect that the MRA of impurities in metals should go to zero as the applied magnetic field strength goes to zero. This is not what falls out [36]

$$\frac{\Delta\rho}{\rho} = \frac{3A^2}{4H^2} \left(\frac{\rho_{\downarrow}}{\rho_{\uparrow}} - 1 \right) \quad (\text{B.3})$$

where $\frac{\Delta\rho}{\rho}$ is the resistivity with the field parallel to the current minus the field perpendicular to the current, normalized to essentially the resistivity at zero applied field. It is a measurable quantity. $\frac{\rho_{\downarrow}}{\rho_{\uparrow}}$ is the ratio of the appropriate matrix elements summed to give the total contribution from the spin down and spin up bands to the resistivity.

It can be seen immediately that as H approaches zero, the anisotropy becomes infinite! The $L_z S_z$ result yields similar problems in that it stays constant as $H \rightarrow 0$ or gives qualitatively incorrect results for real systems.

Application to Manganites

Malozemoff proposes a cubic anisotropy to solve the “zero field catastrophe” that occurs in the above derivations. This cubic anisotropy amounts to increasing the diagonal energy of the e_g orbitals by some fixed amount in the previous formulation and then rediagonalizing the matrix before computing any scattering matrix elements. It is shown that this eliminates the zero field problem and brings the theory into good qualitative agreement with experiment.

This cubic anisotropy energy might seem somewhat arbitrary in metallic systems with magnetic impurities. However, this increase in the e_g orbital energies is similar to what happens in manganites due to the crystal field splitting. As a result, this formulation from Malozemoff is applicable to the CMR materials. This would also lead one to expect that, since there is always some splitting in the manganite energy levels due to the crystal field, there should always be some non-zero MRA value if the material is in a ferromagnetic state.

Further Motivation of the Empirical Partition Function

It is important to address interpreting the expression given in Equation 5.14 as a partition function. With respect to the conduction mechanism, the form of Equation 2.1 deserves some scrutiny. That an electron from the d-orbital moves simultaneously with an electron from a p orbital implies that as far as conduction is concerned there may be some merit to considering a two electron system. This system has a total spin of one. A partition function (Z) based on spin projections of this system would have the following form [51].

$$Z_N = (e^0 + e^{z_1} + e^{z_{-1}})^N \quad (\text{C.1})$$

where the individual Boltzmann factors corresponding to different spin projections and N being the number of particles in the system.

To this a term should be added to account for the fact that these two electrons are in a product state of different orbitals on different ions, but that there is some energy associated with their correlation.

$$Z_N = (e^0 + e^{z_1} + e^{z_{-1}} + e^0 e^{z_1} e^{z_{-1}})^N \quad (\text{C.2})$$

giving

$$Z_N = (1 + e^{z_1} + e^{z_{-1}} + e^{z_1+z_{-1}})^N \quad (\text{C.3})$$

where the e^0 term has been set simply to one. In the double exchange mechanism the electron transfer occurs without a spin flip. In the $J_H \rightarrow$

∞ limit that would mean that the spin 0, the anti-ferromagnetic exchange contribution to the energy of the system is negligible.

This form implies that the final term in Equation C.3 might follow the relation

$$z_1 + z_{-1} = f(T) \propto \int \phi_d H \phi_p d^3r \quad (\text{C.4})$$

This statement implies that the energy difference between the spin up and spin down projection is proportional to an overlap integral between the d and p orbitals participating in the double exchange interaction ϕ_d, ϕ_p and may be a function of temperature.

Equation C.4 is meant to show that the overlap between the two orbitals may necessarily be a function of temperature (and possibly of time) if the phononic contribution to the particle energies cannot be ignored. The motivation for considering the spin projection energies to be functions of temperature will be given below.

It is important to determine how far one can push this partition function when it comes to making predictions. Using the standard fundamental thermodynamic relations and the values of the coefficients obtained empirically, the magnetization and the entropy can be easily calculated.

$$S = - \left(\frac{\partial A}{\partial T} \right)_H \quad (\text{C.5})$$

The thermodynamic relation for the magnetization has been given in Equation 5.12. The exponents used in this development are given in Equation 5.8.

If one naively took this reduced magnetization to be an order parameter and added it to the reduced entropy, which is negative, then as a function of temperature a peak that looks similar to the phenomenon of CMR is formed. This peak is shown in Figure C.2. The CMR effect, the reduction of the resistivity under an applied magnetic field, can be achieved if the polaronic coefficient, the parameter with the explicit temperature dependence, is assumed to be a function of the magnetic field. If this parameter is changed, peak suppression is achieved. For peak shift, the non-temperature dependent parameters, such as the energy associated with the applied field, must be increased or decreased. Some sample curves are shown in Figure C.3.

One can see from the plots that the magnetization does not approach T_c with the appropriate dependence and that the CMR-like peak rises too slowly and the transition is too broad in temperature. However, all the qualitative pieces are present to describe the CMR phenomena. The quantity is small at low temperatures, turns sharply upwards at some finite temperature

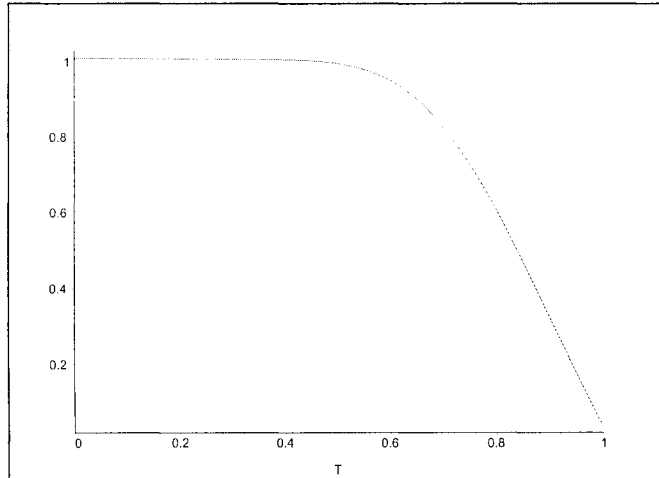


Figure C.1: The normalized magnetization computed from the partition function using empirically determined coefficients.

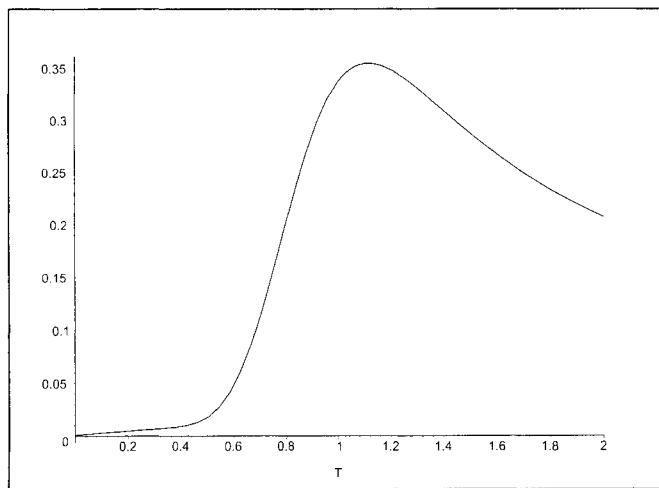


Figure C.2: This peak is found by simply adding the normalized entropy of the system (which is negative at low temperatures) to the magnetization. The reduced temperature ($= \frac{T}{T_c}$) has been used.

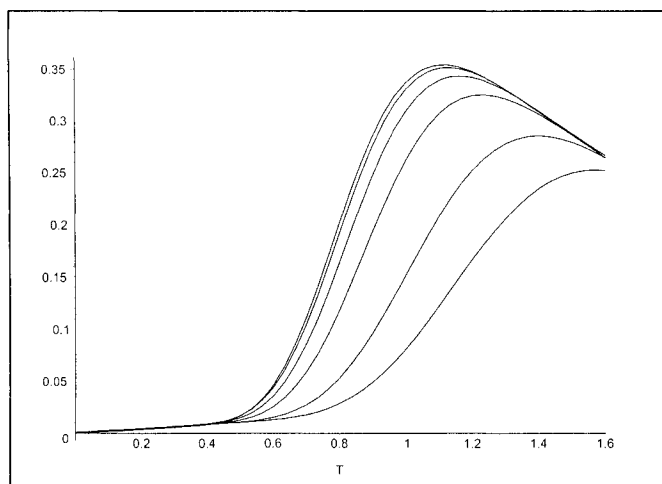


Figure C.3: Peak suppression as a CMR-like effect based on a systematic change in the empirical parameters. The peak suppression arises as a result of a change in the coefficients on the temperature dependence while peak shift is a result of a change in the non-temperature dependent parameters. The reduced temperature ($= \frac{T}{T_c}$) has been used.

near $T/T_c=1$ and has a “thermally activated” exponential decay type of dependence above T_c . If a rigorous definition for the exponents in this simple partition function was available, it would likely improve this as a description of the CMR phenomenon.

AMR and LLG Simulations

The Landau Lifshitz Gilbert (LLG) equation in spherical coordinates is

$$-\frac{\partial\theta(t)}{\partial t} \sin(\theta(t)) = \frac{\gamma}{M_s} \frac{\partial W}{\partial\phi(t)} + \alpha \frac{\partial\phi(t)}{\partial t} \sin^2(\theta(t)) \quad (\text{D.1})$$

$$\frac{\partial\phi(t)}{\partial t} \sin(\theta) = \frac{\gamma}{M_s} \frac{\partial W}{\partial\theta(t)} + \alpha \frac{\partial\theta(t)}{\partial t} \quad (\text{D.2})$$

where θ is the azimuthal angle relative to the z-axis, ϕ is the angle in the x-y plane, γ is the gyromagnetic ratio, M_s is the saturation magnetization, α is the damping coefficient and t is time. W in Equation D.1 is the relevant energies. Here they are given by

$$W = W_A + W_D + W_Z + W_{Ex} \quad (\text{D.3})$$

$$\text{where} \quad W_A = K_1 \sin^2(\theta(t))$$

$$W_D = \frac{\mu_0 M_s^2}{2} \cos^2(\theta(t)) \quad (\text{D.4})$$

$$W_Z = -\mu_0 \vec{H}_{\text{applied}} \cdot \vec{M} \quad (\text{D.5})$$

$$W_{Ex} \propto \vec{S}_i \cdot \vec{S}_j \approx 0 \quad (\text{D.6})$$

where W_A is the anisotropy energy, W_D is the demagnetization energy, W_Z is the Zeeman Energy and W_{Ex} is the exchange energy that has been set equal to zero because in this simple comparison it is assumed that the spin of the conduction electron, S_i and the spin of the polaronic domain, S_j are perpendicular to each other ($\cos(\theta) \approx 0$). In any case, the exchange energy

Table D.1: The Constants Used in the LLG Simulations

Parameter	Value
α_{LLG}	0.1
γ	0.176 [ps ⁻¹ T ⁻¹]
M_s	25000 [A/m]
K_1	0 [J/m ³]

is always the difficult one to manage in a many body problem and here will be neglected.

The LLG equation was simulated for two situations. The first situation is one in which a static in plane magnetic anisotropy has been considered. The second situation is one in which an oscillating magnetic anisotropy term inserted manually as a small portion of the magnetic field perpendicular to the applied field. The frequency of oscillation was found by computing the time it takes to cross a unit cell at roughly the Fermi velocity. The second situation is meant to simulate the effect of the nanoscale magnetic domains of the ferromagnetic polarons, which are essentially randomly aligned in the a-b plane during the transition, on a moving conduction electron.

The results for the direction cosines vary strongly for the two different situations. The parameters used for the calculations are given in Table D.1.

For a strong field applied in the c-axis direction and no field applied in the a-b plane, the direction cosine m_z stays aligned in the z direction ($m_z=1$) and the other two direction cosines in x and y do not have any appreciable component of the magnetic moment ($m_x = m_y = 0$).

Static In-Plane Component

The case of a small static field in one direction, either x or y, that is about one percent of the applied field is also analyzed. In this case, the total magnetic vector precesses from alignment in the z direction, to some small deviation from total alignment in the z direction. This would not necessarily cause extra spin-spin scattering by double-exchange, since all electron spins on all sites would precess to the same angle and remain there for all future times.

Of course, if these two magnetic fields, one arising from a preferred magnetization in the plane and the external applied field, are aligned, then no deviation should be seen from spin alignment with the applied field.

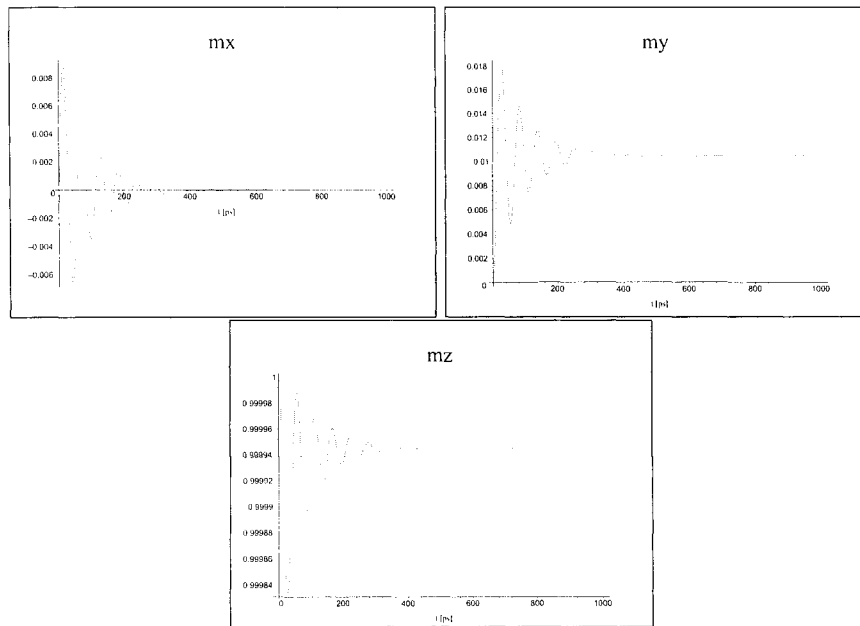


Figure D.1: The direction cosines for a small static magnetic field in the y direction and a large static magnetic field applied in the z-direction. The lattice stiffness was $\alpha_{LLG}=0.1$. The direction of magnetization is no longer entirely in the z-direction ($m_x=m_y=0$, $m_z=1$) but has some component in the y-direction.

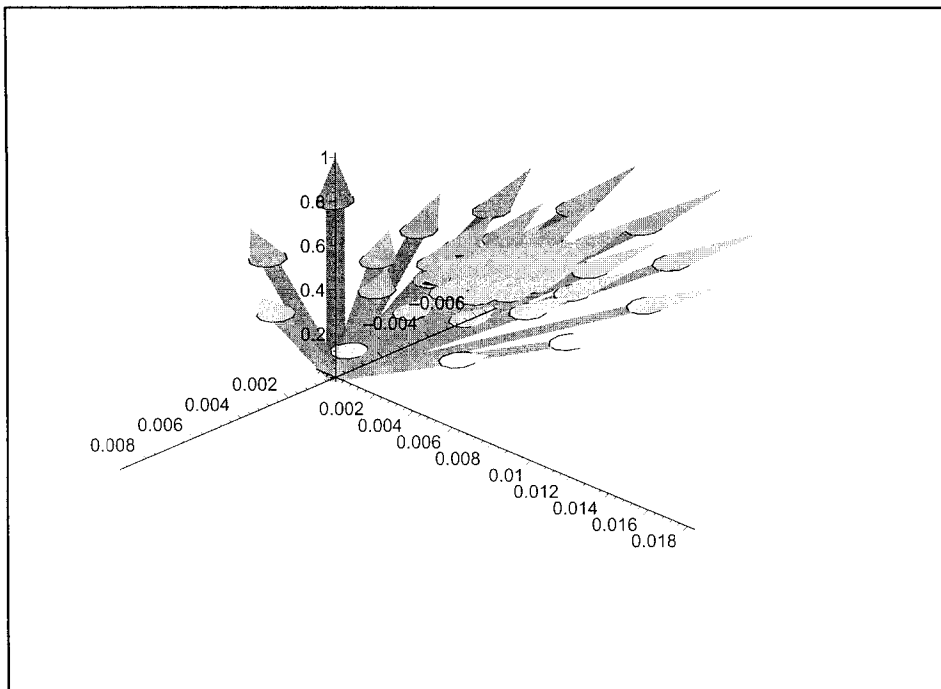


Figure D.2: The vector defined by the direction cosines of a classical spin in a large H_z and small static H_y are shown for $\omega = 0.1, \alpha = 0.1$. The spin precession is visible, until the precession comes to rest at a certain offset from the z -axis.

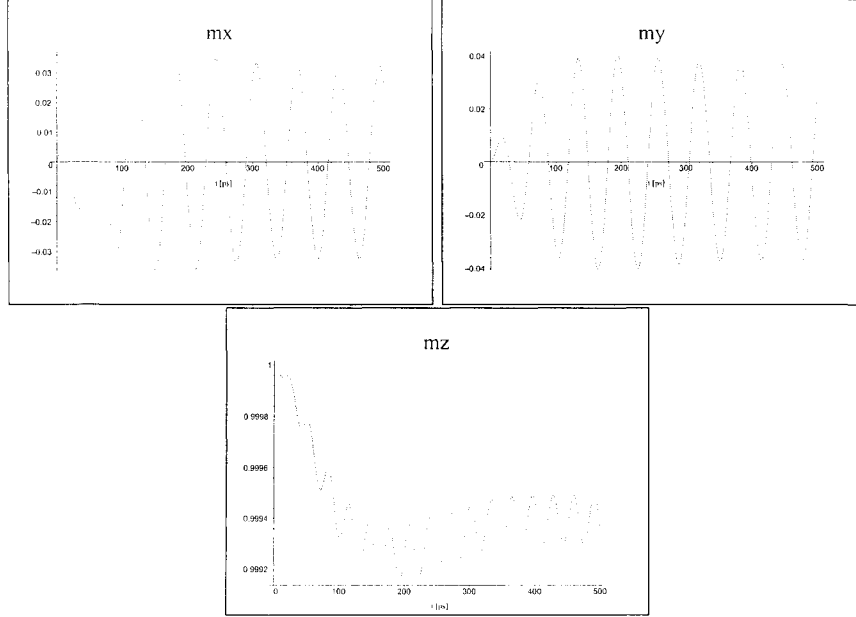


Figure D.3: The direction cosines for a low frequency, $\omega=0.1$, oscillating magnetic field in the y direction and a large static magnetic field applied in the z-direction. The lattice stiffness was $\alpha_{LLG}=0.1$. The direction of magnetization is no longer entirely in the z-direction ($m_x=m_y=0$, $m_z=1$) but has some oscillatory components as the spin precesses about the z-axis.

Oscillating In-Plane Component

The case of a small oscillating magnetic field, with components only in y, can also be investigated. The reason for having components just in one dimension is to simulate antiferromagnetic alignment of the ferromagnetic domains. To a traveling electron, these static magnetic domains might look something like a spin wave. Essentially the simulation being attempted here is that of a free electron traveling down a corridor between antiferromagnetically aligned spins.

In this case, it is seen that the single electron spin never reaches an equilibrium position, but precesses continuously in time. Unless all the sites in the lattice have phases that differ only by integers of 2π , there will be increased spin-spin scattering for this situation.

Even in the case of magnetic domains that do not affect the conduction electron, the local magnetic field could cause misalignment of the t_{2g} spins from site to site, causing extra scattering by double exchange.

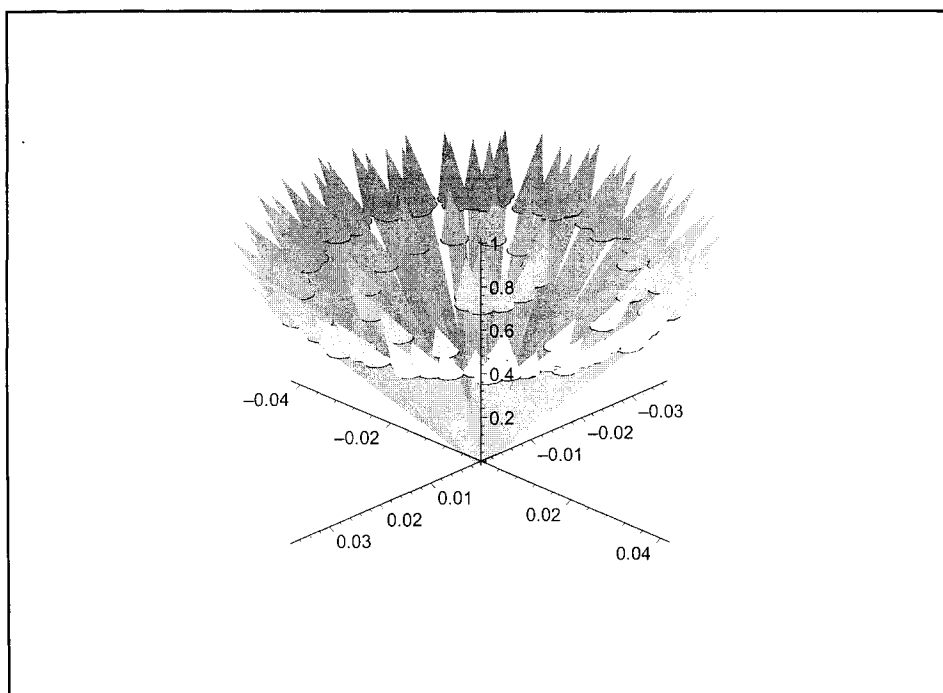


Figure D.4: The vector defined by the direction cosines of a classical spin in a large H_z and small oscillating H_y are shown for $\omega = 0.1, \alpha = 0.1$. The spin precession is visible. The spin precesses out of alignment with the z-axis and shows oscillatory behavior in all three direction cosines for all subsequent times.

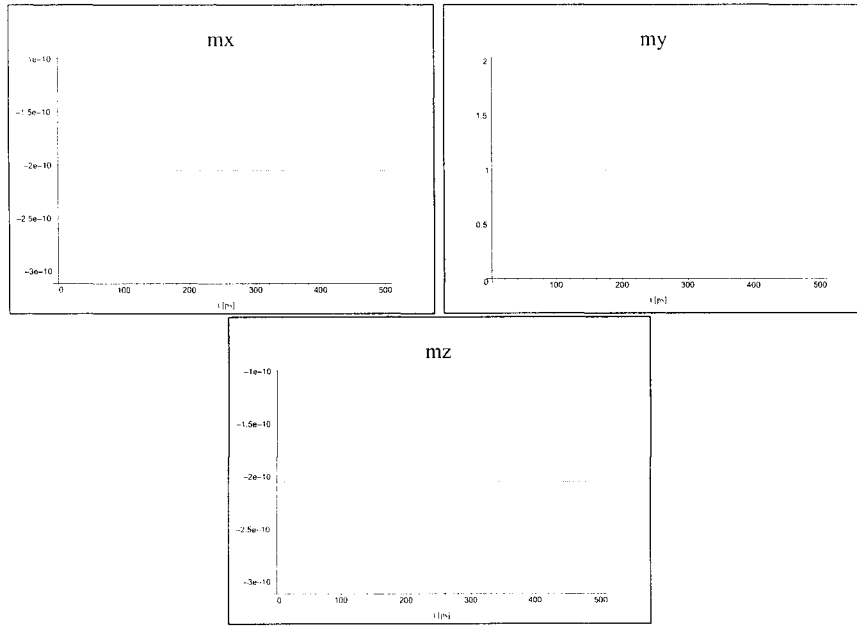


Figure D.5: The direction cosines for a low frequency, $\omega=0.1$, oscillating magnetic field in the y direction and a large static magnetic field applied in the *same* direction. The lattice stiffness was $\alpha_{LLG}=0.1$. The large field in the y-direction swamps the small oscillation and the spin stays aligned in the y direction ($m_x=m_z \sim 0$, $m_y=1$).

This additional spin precession for an oscillating component in the y direction is not seen when the magnetic field is applied in the y direction. This is shown in Figure D.5. In this case, there would be no additional scattering by double exchange. This might qualitatively account for the lower resistivity in LCMO near T_c for an applied magnetic field in the a - b plane relative to applying the magnetic field in the c -axis direction.

Summary

Essentially, an attempt was made to obtain some grasp of what effect the local magnetization, on the scale of the unit cell, might have on conduction by double exchange. Given that nanoscale magnetic domains are present in the lattice below T_c , perhaps as a result of the formation of ferromagnetic polarons, the local magnetization that a double-exchange electron sees may have components that differ slightly from the applied field. If the damping coefficient is sufficiently small so that the electron spin is sensitive to these local changes, these crystal magnetic field components due to spin-spin correlations from magnetic domain formation can cause the spin of an electron on a given site to be perturbed out of alignment with an applied magnetic field. This can lead to an increase in scattering for a magnetic field applied in different directions relative to the crystallographic orientation.

The Loss of the Magnetization at the MIT in LCMO

The difference in ω_0 across the transition is unfortunately rather poorly qualified by the theory developed in section 4.2.1. That ω_0 should decrease and perhaps become negative might seem intuitive, though Figure 4.7 implies a divergence of ω_0 as $T \rightarrow T_c$. Whether this is physical or not, it might be an attractive idea given that if the energy decrease from JT trapping was sufficient to overcome the coulomb repulsion between the electrons a situation like Figure E.1 might be possible. In one stroke this would explain the change in resistivity and the onset of paramagnetism. This would require a large change in the band structure and a *colossal* change in the energies of the e_g orbitals. Energy reductions greater than about 10 eV would be required to overcome the coulomb repulsion in the valence band of these materials [56].

From the resistivity analysis, it is suspected that the Jahn-Teller localized state is going to be lower in energy than the conduction state. If this Jahn-Teller energy is sufficiently large and negative, then perhaps the lowering is sufficient to bring the e_g orbitals energy lower than that of the t_{2g} orbitals. If the opportunity to reduce the energy is great enough, it may be enough to overcome the coulomb repulsion between the electrons. This would make double occupancy of the e_g orbitals favorable over single occupancy of the t_{2g} orbitals. Therefore, through the course of the transition, the e_g orbitals become fully occupied in the case of an Mn^{+3} orbital and partially occupied in the case of the Mn^{+4} . Before the transition, there were either three or four ferromagnetically aligned electrons per Mn-ion. After the transition, there are at most one ferromagnetically aligned electron on, in the case of a doping level of $x = 0.35$, thirty five percent of of the Mn-ion sites. The number of sites with an unpaired electron will depend on the doping level. This effect

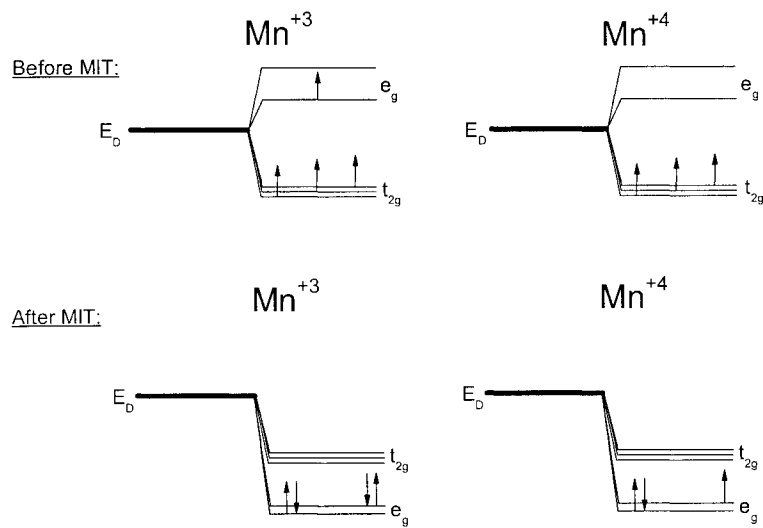


Figure E.1: Possible energy level diagram and electron configuration if the e_g orbitals become low enough in energy to become favorable over the gain in coulomb energy and the antiparallel alignment of spins. E_D stands for the degeneracy energy before any splittings are applied.

is shown schematically in Figure E.1. This estimate is without considering the new most favorable arrangement of these spins based on exchange, any kind of domain structure that may form, or another means of suppressing the macroscopic expression of ferromagnetism. This may help to explain the transition from ferromagnetism at low temperatures to paramagnetism at high temperatures, there will still be some ferromagnetic electrons in the lattice, but they will be greatly in the minority.

That this might be a reasonable picture, that with growing temperature the e_g orbitals, or some set of orbitals, sink to very low energy due to phononic trapping, is supported by the fact that above the transition temperatures the material no longer exhibits the CMR effect. If the JT distortions only lowered the energy of the trapped state a small amount even at high temperatures, then the liberation of the carriers, like that observed during the transition, should be possible at any temperature above T_c as well. Somehow these carriers are put entirely out of reach of any kind of perturbation, large or small. This supports the idea that they move to very low energy, so that they are very strongly bound on an Mn-ion site.

This change might also be accompanied by a change in the bonding of the materials. LSMO does show a structural transition well near T_c for low doping levels [4]. This may be evidence of bond rearrangement due to the energy level changes described here. The same effect may be present in LCMO.

Some Properties of Mylar C - Dupont Datasheet

Some important properties of the Mylar C thin film are given in Table F.1.

Table F.1: Select properties of Mylar C capacitor grade polymer at a thickness of $1.5\mu\text{m}$.

Parameter	Value
$V_{Breakdown}$	225 [V]
V_{rise}	100 [V/s]
ϵ_r	3.3 (at 60 Hz)
ρ_V	10^{18} [Ωcm] (at 25°C)
V_{rise}	100 [V/s]
V_{rise}	100 [V/s]